Relativistic Quasiparticle Random Phase Approximation in Deformed Nuclei

Dissertation
von
Daniel Peña Arteaga

Institut für Theoretische Physik T30
Physik Department
Technische Universität München

Mai 2007

Physik–Department der Technischen Universität München
Theoretische Physik T30

Relativistic Quasiparticle Random Phase Approximation in Deformed Nuclei

Daniel Peña Arteaga

Vollständiger Abdruck der von der Fakultät für Physik der Technischen Universität München zur Erlangung des akademischen Grades eines

Doktors der Naturwissenschaften (Dr. rer. nat.)

genehmigten Dissertation.

Vorsitzender:		Univ.-Prof. Dr. R. Krücken
Prüfer der Dissertation:	1.	Univ.-Prof. Dr. P. Ring
	2.	Univ.-Prof. Dr. W. Weisse

Die Dissertation wurde am 16.05.2007 bei der Technischen Universität München eingereicht und durch die Fakultät für Physik am 25.06.2007 angenommen.

Abstract

Covariant density functional theory is used to analyse the response to the E1 and M1 electromagnetic transition operators in superfluid deformed nuclei in the framework of self-consistent Hartree-Bogoliubov theory and relativistic quasiparticle random phase (RQRPA) approximation. The fully self-consistent RHB+RQRPA equations are posed for the case of axial symmetry and for three different kinds of energy functionals, and solved with the help of a new parallel code. Special care is taken in order to validate the proper decoupling of spurious modes. Results of the first multipole magnetic operator (M1) response in light and heavy deformed nuclei are presented and analysed; in particular, the scissors mode and spin excitations. Qualitative agreement with experiment is obtained for the position of the scissors mode, and its structure as a rotation of the deformed neutron density against the deformed proton density reproduced. In addition to the scissors mode, a soft M1 mode with strong orbital character is found in heavy nuclei at relatively low energies. From the analysis of the proton and neutron transition densities in the intrinsic frame, and from the structure of the RQRPA amplitudes, it is concluded that this mode corresponds to a collective rotation of the deformed neutron skin against the deformed proton-neutron core. The response in light and heavy nuclei to the electric dipole operator (E1) is also given consideration. The position of the Giant Dipole Resonance is well reproduced within the RHB+RQRPA framework in axial symmetry. The effects of superfluidity and deformation on the Pygmy Dipole Resonance are closely examined. Excellent agreement with recent experimental results is found.

Acknowledgements

First and foremost I would like to thank my supervisor, Prof. Dr. Peter Ring, not only for stimulating discussions and timely advice, but also for his support throughout the various phases of the work presented in this document. His understanding and experience in many areas has made a pleasure working with him. I am particularly grateful for his optimism and overall confidence in the project, always trying to point me on the right direction but giving me enough leeway to learn from my own mistakes.

Many thanks go to Roger Hilton, who was always a source of good humour and interesting conversations while at the TUM. He patiently read the first drafts and helped me polish all the rough edges, both in the contents and in the use of the English language.

It is a pleasure for me to thank all my colleagues at the TUM Theory Department and at the TUM campus in Garching, who have provided support and company during my time in Munich, with a special mention to Nils Paar, Christian Rummel, Ioannis Daoutidis, Andreas Serr, Marco Ajello, Rasmus Voss, Alfredo Alexander-Katz, Elena Litvinova, Marta Balbás, Javier Madroñero, and all the guests that contributed to make me feel at home at the University.

Many friends have helped me to persevere in my efforts, sharing with me their free time, good will and beer from all around the world. Even though they are too many to mention all, they know who they are. Thanks to all!

And finally, my family deserves a very special thanks, the best I can give. Mamá, Papá, Tío, Lola, Gabi, Carmelita, Lolo, …, esta tésis está dedicada, con mucho cariño, a todos vosotros.

"Writing in English is the most ingenious torture ever devised for sins committed in previous lives."
— Jame Joyce, 1882-1941

Contents

List of used Acronyms

MF	Mean Field
HF	Hartree Fock
HK	Hohenberg-Kohn
KS	Kohn-Sham
RPA	Random Phase Approximation
DFT	Density Functional Theory
TDDFT	Time Dependent Density Functional Theory
GEA	Gradient Expansion Approximation
GGA	Generalized Gradient Approximation
RMF	Relativistic Mean Field
RDFT	Relativistic Density Functional Theory
RHB	Relativistic Hartree Bogoliubov
HFB	Hartree Fock Bogoliubov
TRK	Thomas-Reiche-Kuhn
GMR	Giant Monopole Resonance
GDR	Giant Dipole Resonance
IVGDR	Isovector Giant Dipole Resonance
IV	Isovector
IS	Isoscalar
PDR	Pygmy Dipole Resonance
RPA	Random Phase Approximation

RRPA	Relativistic Random Phase Approximation
QRPA	Quasiparticle Random Phase Approximation
RQRPA	Relativistic Quasiparticle Random Phase Approximation
pn-RQRPA	proton-neutron Relativistic Quasiparticle Random Phase Approximation
TDRMF	Time Dependent Relativistic Mean Field
LDA	Local Density Approximation
NLME	Non Linear Meson Exchange
DDME	Density Dependent Meson Exchange
DDPC	Density Dependent Point Coupling
NL3	Parametrization of Relativistic Mean Field non linear model
DD-ME1	Parametrization of the relativistic density dependent meson exchange functional
DD-ME2	Parametrization of the relativistic density dependent meson exchange functional
PC-F1	Parametrization of relativistic density dependent point coupling functional
DB	Dirac Brueckner
BCS	Bardeen-Cooper-Schrieffer
TRM	Two Rotor Model
TDA	Tamm-Dancoff Approximation
M1	Magnetic $J^\pi = 1^+$ transitions
E1	Electric $J^\pi = 1^+$ transitions
QCD	Quantum Chromodynamics
EFT	Effective Field Theory
EWSR	Energy Weighted Sum Rule
LAPACK	Linear algebra package

Chapter 1

Introduction

"I am frequently astonished that it so often results in correct predictions of experimental results."
— Murray Gell-Mann, 1929 -

Ever since Ernest Rutherford first proposed the existence of the atomic nucleus in 1911, considerable theoretical and experimental effort has been put into the understanding of its basic structure and properties. Early models, like the liquid drop model which was historically the first to be proposed, treated the nucleus as a matter continuum. It was not until the discovery of the proton in 1918, and then later of the neutron, 1932, that nuclear physics took its current shape as a fully fledged many-body quantum system of strongly correlated particles. Since then it has always played an outstanding role in the development of many-body theories and has been at the forefront of new experimental techniques.

As one of the most active research areas from the beginning of the twentieth century, Nuclear Physics has always required a strong link between experiments and theory. Early experimental techniques allowed only the study of nuclei on or close to the β-stability line and where limited to energy scales considerably smaller than the nucleon mass. Thus, the nucleus has traditionally and successfully been described as a collection of non-relativistic nucleons interacting through an instantaneous two-body potential, with the dynamics given by the Schrödinger equation. However, recent advances in experimental techniques allow for the production and study of exotic nuclei close to the drip lines. Major experimental facilities e.g. NCSL, ORNL and ANL (USA), GSI (Germany), GANIL (France), RIKEN(Japan), CERN (Europe), Dubna (Russia), TRIUMF (Canada) have continually pushed the limits of our comprehension of the nuclear system.

Although intimately related, three main areas of investigation of the strong interaction may be distinguished: heavy ion collisions at relativistic energies that probe the nature of quark-gluon confinement and the assumptions of the underlying QCD. Electron and Muon scattering experiments probe the quark-gluon structure of hadrons and of nuclei. And, finally, experiments at lower energies with beams of stable and unstable nuclei, using Radioactive Nuclear Beams (RNB) facilities probe the structure and the dynamics of nuclei on and far the stability line. In particular, the study of exotic nuclei with RNB techniques encompasses new aspects of nucleonic matter: limits of nuclear existence, halo phenomena, nuclei with extreme isospin, the nature of pairing correlations, shell structure and magic numbers.

On the theoretical front, it is well established nowadays that QCD is the underlying fundamental theory of strong interactions. However, the link between QCD and a bare nucleon-nucleon force remains one of the long-term goals of nuclear theory. The difficulty of describing quantitatively the structure and interaction of nucleons in terms of QCD is due to its non-perturbative character at low energies. Even though, to date, only a qualitative understanding has been possible, efforts that take the underlying symmetries of QCD as a basis and exploit separation of scales using EFT look very promising [53], and are already bearing fruit. Other new approaches take advantage of the relatively low energy dynamics of the nucleus to extract a universal potential that cuts out the high momentum part of the interaction [19].

Understanding the underlying mechanisms for effects such as neutron skins, halos, shell closures far from the stability valley and exotic collective excitation phenomena is a fundamental step in the theoretical efforts to achieve a consistent and unified model of the atomic nucleus. For very light nuclei, a bare interaction complemented with a phenomenological three body force solved in the framework of Quantum Monte Carlo Methods provides an exact solution for the few-body problem. However, the complexity of these no-core shell model calculations renders the method unfeasible for nuclei with masses greater than $A = 16$.

Another approach, using a shell model calculation based on configuration mixing, already has been very successful in describing microscopically the nucleus for many years. Including explicit correlations between nucleons, usually only in a restricted space of valence nucleons, realistic modern shell model potentials are able to predict many nuclear properties, from bulk quantities to excited states. However, since the model space expands quickly with the number of particles, its application is restricted to light and to medium mass nuclei.

For the study of heavier nuclei alternative methods have been developed, usually in the form of self-consistent mean field theories. Their starting point is the supposition that, in first order, the nucleons can be considered as independent particles moving in an average field generated by the other nucleons. Phenomenological in nature, their success in describing bulk nuclear properties all across the nuclear chart make them a very good tool for the study of nuclear phenomena. Their roots lie in Density Functional Theory: formulated as effective energy density functionals whose parameters are adjusted to well known properties of a few selected nuclei, they can be applied universally to calculate properties of all nuclei. The best known of such functionals are the Skyrme [158] and Gogny [58] functionals, developed over the last decades to achieve a high level of precision in the description and prediction of experimental data.

On the same level, models based on Relativistic Density Functional Theory also offer a very interesting tool for the study of nuclear structure phenomena. Later we shall show, models based on Relativistic Density Functional Theory are at least as successful as their non-relativistic counterparts, and provide several advantages compared to a non-relativistic theory. They are, however, not devoid of problems; usually the actual implementation is more troublesome. It starts at a more fundamental level, including spin properties in a very natural way, and classifying different physical quantities by their behaviour under Lorentz transformations. The appearance of a scalar S and vector V fields is a direct consequence of relativity, that leads, for example, to a new mechanism for saturation via the difference between the scalar and vector densities. The absolute size of the scalar field and the time-like component of the vector field characterise the essential features of nuclear systems, i.e. the shell structure: their difference determines the weak nuclear mean field in which nucleons move and their sum the strong spin-orbit term. Another effect that can only be explained with a relativistic description is the pseudospin symmetry in nuclear spectra, known for nearly forty years, which comes about from the fact that both fields, S and V, are almost equal in absolute value.

Relativistic Density Functional Theory, as applied in Nuclear Physics, originates from the basic concepts of the Walecka model [140, 121], first proposed by Teller [73, 74, 46]. The theory is based on the following assumptions: i) nucleons are treated as point particles, ii) relativity is fully taken into account and iii) nucleons move as independent particles in the corresponding mean fields. The nucleon dynamics are described by Dirac equations containing a mass operator including meson fields with different spin, parity and isospin properties. In almost all implementations for nuclear matter and finite nuclei, RDFT is used in the *no-sea* approximation: the contribution from the Dirac sea of states with negative energies is neglected when calculating densities and currents. In practical applications, a very simple combination of fields appeared to be sufficient: isoscalar scalar field describing the long range attraction, a isoscalar vector field that simulates the short range repulsion, a isovector vector field that takes into account the nuclear interaction isospin dependence, plus the photon fields carrying the electromagnetic interaction. In lowest order, the fluctuations for these effective meson fields are not taken into account (i.e. the fields are not quantized), leading to a semi classical theory, and are minimally coupled with the nucleons by local vertices. However, it was soon realized that a density dependence (i.e. in-medium aware interaction) was crucial if quantitative agreement with experimental data was to be achieved. Several different models have been proposed to include an effective density dependence. Historically the first was the non-linear model, proposed by Boguta and Bodmer [22], in which the density dependence is included via non-linear self-interactions between the scalar mesons. Another model was introduced by Brookmann and Toki [146], that includes the density dependence explicitly in the coupling constants. Point coupling functionals, the last to come, were first introduced by Büervenich and Madland [33]. They combine two- three- and four-body contact interactions together with derivative terms and can be considered an expansion of the finite range propagators of the original RMF model.

In non-closed shell nuclei, pairing correlations play a very important role. The BCS approximation has always been a very popular scheme to treat correlations due to its simplicity. However, it breaks down in nuclei close to the drip lines, where levels in the continuum may be occupied. This problem can be avoided using the RHB model [20, 21], which includes an explicit pairing channel. The most successful of RMF models use the non-relativistic Gogny interaction in the pairing channel, as has been shown that there is practically no mixing between small and large components of the Dirac spinors [141, 142, 104]. Since this force has a finite range, it provides a natural cutoff, avoiding one of the most important problems that plague BCS and other schemes involving artificial pairing windows.

In particular, RHB theory has been successfully applied to the study of many ground state properties in nuclei, and shows a high degree of accuracy in the reproduction of experimental data: masses and radii, shape coexistence [91, 90, 167], halos [82, 117], Λ-hypernuclei [84, 164], neutron and proton rich nuclei [162, 10, 86, 85, 88, 87, 156, 89, 80, 15, 104, 168, 111, 122, 149, 143], rotational bands and nuclear magnetism [8, 44, 136, 135, 2, 3, 5, 6], superdeformations [4, 131, 7, 148, 100], etc.

The excitation phenomena in nuclei, in particular giant resonances and low-lying excitations, have raised significant interest in recent years. New experimental techniques allow the study of exotic nuclei that lie very far away from the valley of stability. Collective modes of excitation, such as giant resonances, have been one of the most active topics in nuclear physics. Their properties, in particular their width and position, reflect the underlying collective dynamics of protons and neutrons and provide a very valuable insight into the nuclear interaction. Two basic categories of giant resonances are distinguished: electric and magnetic, corresponding respectively to excitations that involve and do not involve the spin degrees of freedom. The magnetic multipole resonances are excited by relatively small set of scattering processes, while electric resonances can be excited by a variety of different techniques, especially by inelastic scattering of α particles, protons, photons, etc.

The low amplitude limit of the Time Dependent Relativistic Mean Field (TDRMF), the Relativistic Random Phase Approximation (RRPA), is the natural extension of the self-consistent relativistic approach to describe collective states [132]. Even though the majority of nuclei are deformed, most self-consistent studies of the excitation response of nuclei have been performed within spherical constraints, even when applied to axial or triaxially deformed systems. There are many non self-consistent studies which take deformation explicitly into account. The complexity involved and the computational costs of solving the microscopic equations for collective excited states, however, have delayed the appearance of fully self-consistent deformed calculations. Nevertheless, very important and still open questions grant the quest for better and more accurate models a relevance that is not possible to ignore. Spherical beyond-RPA studies, like the phonon coupling and angular momentum projection models, relativistic [96] and non-relativistic [153], try to understand and reproduce the width of the giant resonances, as well as to establish the origin and properties of collective nuclear motion.

In the same spirit, deformed self consistent models are a logical extension to the plethora of tools available in the field of nuclear structure. Questions like the isospin dependence of the nuclear interaction lead unfailingly to focus on the realm of deformed nuclei, where it is undeniably necessary the proper treatment of the underlying intrinsic symmetry. Concrete examples would be e.g. the existence and evolution of low lying soft collective modes, the dynamics of giant resonance splitting or the nature of magnetic spin excitations.

Deeply linked with nuclear structure, the origin of the element abundances, and the processes leading to the formation of matter in the universe, would benefit greatly from more accurate predictions for the reactions involved. The most prospective paths for the formation of heavy nuclei are the s-process (slow neutron capture), r-process (rapid neutron capture), and rp-process (rapid proton capture). It is presumed that these rapid processes run in environments with high isospin asymmetry, and that the subsequent β-decays are slower than the captures, resulting in the production of elements heavier than iron. Complex nuclear reaction networks used in the study of these phenomena need the input from nuclear structure theory calculations. Therefore, it is very desirable to be able to calculate more accurate decay rates that would help to elucidate the origin and observed abundances of chemical elements. Deformed mean field calculations of nuclear excitations, if shown up to the task, can provide a very valuable input that could be the missing quantitative leap forward.

In this work we present the development and first results of the application of the Relativistic Quasiparticle Random Phase Approximation to axially deformed nuclei. The RQRPA equations are formulated in the canonical basis of the RHB model for the ground state, and solved in its matrix representation. As a first approximation, pairing correlations are included using a monopole pairing force whose strength is adjusted to gaps calculated from experimental even-odd mass differences. The framework is fully self-consistent, the same interaction is used for the ground state and excited states calculations; i.e., no new parameters are introduced at the RPA level to adjust the interaction.

As a first application of the developed RHB+RQRPA in axial symmetry framework, we analyze the results of sample calculations of multipole electromagnetic transitions in light and heavy nuclei. In particular, the scissors mode, excited by the first multipole magnetic transition operator, is studied in two representative deformed nuclei, ^{20}Ne and ^{156}Gd. As examples of E1 excitations, the Giant Dipole Resonance and Pygmy Dipole Resonance have also been studied, first in the isotope chain from ^{20}Ne to ^{26}Ne, and in a representative deformed heavy nucleus, ^{100}Mo.

This work is organized as follows. The second chapter introduces briefly the formalism behind Density Functional Theory, and discusses the extensions required for the proper description of the wide range of phenomena found in nuclei. The next chapter will introduce the relativistic extension of Density Functional Theory as it is applied in nuclear physics, with BCS as a first approximation to pairing. Chapter 4 introduces the general Relativistic Quasiparticle Random Phase Approximation formalism as the small amplitude limit of the Time Dependent Density Functional Theory. The next chapter particularises for the case of axial symmetry and discusses the implications of the reduced symmetry compared to that of the spherical case. Test cases and a brief discussion about the numerical implementation can also be found in this chapter. Some illustrative calculations in light, medium and heavy nuclei for the M1 and E1 transition modes are presented in the next two chapters, 6 and 7. Finally, the last chapter is dedicated to the conclusions and a brief outlook of future applications and improvements.

Chapter 2

Density Functional Theory. A brief introduction.

"Prediction is very difficult, especially if it's about the future."
— Niels Bohr, 1885-1962

Density Functional Theory (DFT) is a quantum mechanical method used in many areas of physics to investigate many-body systems. DFT is among the most popular and versatile methods available in condensed matter physics, computational chemistry, and, of course, nuclear physics. Novel applications relevant to fields traditionally considered more distant from quantum mechanics like biology and mineralogy are beginning to appear.

DFT owes this versatility to the generality of its fundamental concepts and the flexibility with which it can be implemented, despite being based on quite a rigid conceptual framework. Traditional methods in many body quantum theory, in particular Hartree Fock (HF) theory and its descendants, are based on complicated many-particle wave functions. DFT promotes the local particle density $\rho(\mathbf{r})$ from just one among many observables to the status of a key variable, on which the calculation of all other observable can be based. In principle, it is a simpler quantity to deal with both conceptually and practically.

Although Density Functional Theory has its conceptual roots in the Thomas-Fermi model, it was not put on a firm theoretical footing until the Hohenberg-Kohn (HK) theorems [67]. In the original article it was shown that knowledge of the local ground state density $\rho(\mathbf{r})$ implies knowledge of the ground state wave function and hence of all other ground state observables. Even though DFT was originally a ground state theory, it has also been successfully extended to the time-dependent domain, and used to determine excited states [32]. Although the sequence $\rho(\mathbf{r}) \rightarrow \Psi(\mathbf{r}_1, \cdots, \mathbf{r}_N) \rightarrow \hat{\mathcal{O}}$ describes the conceptual structure of DFT, it does not represent what is done in actual applications, which typically proceeded along rather different lines and does not make explicit use of many-body wave functions.

2.1 Density Functional Theory (DFT) formalism

For a many-body system the ground state expectation value for the Hamiltonian is the ground state energy

$$E = \langle \Psi_0 | \hat{H} | \Psi_0 \rangle = \langle \Psi_0 | \hat{T} + \hat{U} + \hat{V} | \Psi_0 \rangle \tag{2.1}$$

where, in the customary decomposition of $\hat{H}$, $\hat{T}$ is the kinetic energy term, $\hat{U}$ is the term corresponding to the interaction between particles and $\hat{V}$ is an external potential. For a given wave function Ψ one can calculate the local single particle density as

$$\rho(\mathbf{r}) = \int d^3r_2 \cdots \int d^3r_N \Psi^\star(\mathbf{r}, \mathbf{r}_2, \cdots, \mathbf{r}_N) \Psi(\mathbf{r}, \mathbf{r}_2, \cdots, \mathbf{r}_N) \tag{2.2}$$

At the heart of DFT is the HK theorem, that states *for ground states* the previous relation can be inverted: given a ground state density $\rho(\mathbf{r})$, it is possible, in principle, to calculate the corresponding ground state wave function Ψ_0. This means that Ψ_0 is a functional of $\rho(\mathbf{r})$, and consequently, all ground state observables are functional of $\rho(\mathbf{r})$ too. The crucial fact which makes this possible is that the ground state wavefunction Ψ_0 must not only reproduce the correct ground state density, but also minimizes the energy. For a given ground state density this can be written as

$$E_{u,0} = \min_{\Psi \rightarrow \rho_0} \langle \Psi | \hat{T} + \hat{V} + \hat{U} | \Psi \rangle \tag{2.3}$$

where $E_{u,0}$ denotes the ground state energy in the external potential $U(\mathbf{r})$. For an arbitrary density, a general functional can be defined

$$E_u[\rho] = \min_{\Psi \rightarrow \rho} \langle \Psi | \hat{T} + \hat{V} + \hat{U} | \Psi \rangle \tag{2.4}$$

It is conceptually useful to write the total energy functional in the following form

$$E_u[\rho] = \min_{\Psi\to\rho} \langle\Psi|\hat{T}+\hat{V}|\Psi\rangle + \int d^3r\rho(\mathbf{r})u(\mathbf{r}) := F[\rho] + U[\rho] \tag{2.5}$$

where the internal energy functional $F[\rho] = \min_{\Psi\to\rho}\langle\Psi|\hat{T}+\hat{V}|\Psi\rangle$ is independent of the external potential $v(\mathbf{r})$, and thus only determined by the structure of the operators $\hat{T}$ and $\hat{V}$. This universality of the internal energy functional allows one to define the ground state wave function Ψ_0 as that antisymmetric N-particle function such that it delivers the minimum of $F[\rho]$ and reproduces ρ_0. If the ground state is non degenerate, this double requirement uniquely determines Ψ_0 in terms of ρ_0 without having to specify $u(\mathbf{r})$ explicitly. The last three equations constitute the constrained-search proof of the HK theorem [95, 93]. The original proof by Hohenberg and Kohn proceeded by assuming that Ψ_0 was not uniquely determined by ρ_0 and showed that this produced a contradiction to the variational principle. Since 1964, the HK theorem has been throughly scrutinized, and several alternative proofs have been found. Thus, assuming knowledge of the energy density functional $E[\rho]$ for a given system, its minimization yields the ground state density, and thus all other possible ground state observables.

However, if the ground state is degenerate a unique functional $\Psi[\rho]$ does not exist, but by definition these wave functions all yield the same energy so the functional $E_u[\rho]$ still exists, and a universal functional $F[\rho]$ can still be defined [45]. This, however, is not a major difficulty since the explicit wave function is not needed in actual applications of DFT. Another conceptual problem with HK theorem is representability, that has two sides. The first is the so called N-representability, i.e., given an arbitrary function $\rho(\mathbf{r})$, whether it is a density arising from an antisymmetric N-body wave function $\Psi(\mathbf{r}_1,\cdots,\mathbf{r}_N)$. The second is the u-representability, i.e., given a function that can be written as (2.2), whether does it correspond to the ground state density for a given potential $u(\mathbf{r})$. The problem of N-representability has been solved, and it can be shown that any non-negative function can be written in terms of some antisymmetric $\Psi(\mathbf{r}_1,\cdots,\mathbf{r}_N)$ in the form (2.2) [56, 60]. The v-representability problem is still an ongoing investigation, although some results regarding it can be found in [37, 155, 92].

Using this very briefly outlined formalism, in theory it should be possible to calculate all observables, since the HK theorem guarantees that they are all functionals of the local density. In practice, however, one does not know how to do this explicitly. Moreover, explicit expressions for $T[\rho]$ and $V[\rho]$ are generally not known, and one has to rely on different approximations. The simplest of such approximations would be the local density approximation LDA, that restricts the form of the density functionals to

$$F[\rho(\mathbf{r})] := \int d^3r\rho(\mathbf{r})f(\rho(\mathbf{r})) \tag{2.6}$$

The LDA approximation exploits the knowledge of the density at point $\mathbf{r}$, but any real system is spatially inhomogeneous, i.e., it has a spatially varying density $\rho(\mathbf{r})$. A first attempt to include information on the rate of change of the density were the so-called Gradient Expansion Approximations (GEA). In this class of approximation one tries to systematically calculate gradient corrections of the form $|\nabla\rho(\mathbf{r})|$, $\nabla^2\rho(\mathbf{r})$, etc., to the LDA. In practice, the inclusion of low-order gradient corrections almost never improves the LDA and often worsens it. A more general form of approximation is the Generalized Gradient Approximation (GGA) [115], that replaces the expansion with more general functions of $\rho(\mathbf{r})$ and $\nabla\rho(\mathbf{r})$

$$F^{GGA}[\rho] = \int d^3r f(\rho(\mathbf{r}), \nabla\rho(\mathbf{r})) \tag{2.7}$$

Although the use of the Generalized Gradient Approximation has lead to major improvements as compared to the Local Density Approximation, it is often not good enough for accurate calculations. In the quest for more accurate functionals, many beyond-GGA schemes have been developed. In chemistry and atomic physics, were the interaction is known, functionals with phenomenological parameters and even admixtures with HF exchange terms have been very successfully applied. Another beyond-GGA development is the emergence of the so called meta-GGAs, which, in addition to the density and its derivatives, depend also on more general forms of densities, like the kinetic energy density [113, 13, 150].

DFT, implemented within the scope of these approximations, has been very popular for calculations in solid state physics since the 1970's. In many cases the DFT gives quite satisfactory results, in comparison to experimental data at relatively low computational costs when compared to other ways of solving the quantum mechanical many-body problem. It can be shown that the density dependent Hartree and Hartree Fock [158] methods traditionally used in nuclear physics calculations can be linked to DFT in a very natural way, leading to a unified description of the different models under a common theory.

2.1.1 The Kohn-Sham approach

Density functional theory can be implemented in many ways. The direct minimization of the energy functional is not normally the most efficient way amongst them; for example, to date, no functional has been able to reproduce shell effects, a phenomenon with a single-particle origin. A far more widely used is the Kohn-Sham approach, that does not exclusively work in terms of the particle density, but brings a special kind of wave-function, single-particle orbitals, back into the game. As a consequence the

DFT then looks formally like a single-particle theory, although many-body effects are still included via the so-called exchange-correlation functional. However, the Thomas-Fermi approximation for $T[\rho]$ is not very good. A more accurate scheme for treating the kinetic energy functional of interacting particles is based on decomposing it into one part that represents the kinetic energy of non-interacting particles of density ρ, $T_s[\rho]$, and another one that represents the remainder, $T_c[\rho]$

$$T[\rho] = T_s[\rho] + T_c[\rho] \tag{2.8}$$

T_s is not known exactly as a functional of ρ, and using the LDA leads one back to the Thomas-Fermi approximation [34], but it is easily expressed in terms of the single-particle orbitals $\phi_i(\mathbf{r})$ of a fictitious non-interacting system with density ρ as

$$T_s[\rho] = -\frac{\hbar^2}{2m} \sum \int d^3 r \phi_i^\star(\mathbf{r}) \nabla^2 \phi_i(\mathbf{r}) \tag{2.9}$$

because, for non-interacting particles, the total kinetic energy is just the sum of the individual kinetic energies. Since the $\phi_i(\mathbf{r})$ are all functionals of ρ, this expression for T_s is an explicit orbital functional but an implicit density functional, i.e., $T_s[\rho] = T_s[\{\phi_i[\rho]\}]$, where the notation indicates that T_s depends on the full set of occupied orbitals ϕ_i, each of which is a functional of ρ. The exact functional can be written now

$$E[\rho] = T[\rho] + V[\rho] + U[\rho] = T_s[\{\phi_i[\rho]\}] + V_H[\rho] + E_{xc}[\rho] + U[\rho] \tag{2.10}$$

where by definition E_{xc} contains the differences $T - T_s$ and $V - V_H$, where V_H is the Hartree energy or classical part of the interaction. E_{xc} is the so called exchange-correlation functional. It is the sum of the energy due to the Pauli principle (exchange) and the energy due to correlations. This equation is formally exact, but of course E_{xc} is unknown — although the HK theorem guarantees that it is a density functional. Since T_s is written now as an orbital functional it cannot be directly minimized with respect to ρ. The scheme suggested by Kohn and Sham [77] for performing the minimization starts by writing the functional derivative in the form

$$\frac{\delta E[\rho]}{\delta \rho(\mathbf{r})} = 0 = \frac{\delta T_s[\rho]}{\delta \rho(\mathbf{r})} + \frac{\delta V_H[\rho]}{\delta \rho(\mathbf{r})} + \frac{\delta U[\rho]}{\delta \rho(\mathbf{r})} + \frac{\delta E_{xc}[\rho]}{\delta \rho(\mathbf{r})} \tag{2.11}$$

and realizing that for a system of non interacting particles moving in an external potential $u_s(\mathbf{r})$ the minimization would look like

$$\frac{\delta E_s[\rho]}{\delta \rho(\mathbf{r})} = 0 = \frac{\delta T_s[\rho]}{\delta \rho(\mathbf{r})} + u_s(\mathbf{r}) \tag{2.12}$$

Comparing the last two equations, both minimizations have the same solution $\rho_s(\mathbf{r}) \equiv$

$\rho(\mathbf{r})$ if $u_s(\mathbf{r})$ is chosen to be

$$u_s(\mathbf{r}) = \frac{\delta V_H[\rho]}{\delta\rho(\mathbf{r})} + \frac{\delta U[\rho]}{\delta\rho(\mathbf{r})} + \frac{\delta E_{xc}[\rho]}{\delta\rho(\mathbf{r})} \tag{2.13}$$

In particular, the equations of motion for this auxiliary system yield orbitals that reproduce the density $\rho(\mathbf{r})$ of the original system

$$\rho(\mathbf{r}) \equiv \rho_s(\mathbf{r}) = \sum_{i=1}^{A} \phi_i(\mathbf{r})\phi_i^\dagger(\mathbf{r}) \tag{2.14}$$

Consequently, one can calculate the density of the interacting (many-body) system by solving the equations of a non-interacting (single-body) system in the potential $u_s(\mathbf{r})$. The question of whether such a potential always exists in the mathematical sense is called the non-interacting u-representability problem. As yet it is not known if interacting ensemble-representable densities may be noninteracting pure-state representable (i.e. represented by a single determinant), which would be convenient, but is not necessary, for KS calculations. Usually the KS equations are solved by a self-consistency cycle, i.e., given an appropriate initial density guess the potentials are calculated and used to find a new density, and the process repeated until convergence has been achieved. It should be clear that the energy eigenvalues for the orbitals are a completely artificial objects. It is only the density that has a strict physical meaning in the KS equations. The KS eigenvalues, on the other hand, in general bear only a semiquantitative resemblance to the true energy spectrum, but in no account should they be trusted. An exception is the highest occupied KS eigenvalue, that can be rigorously related to the first ionization energy [114, 9, 94], although this is only strictly true for the exact functional and holds only approximately in all other cases.

2.2 Nuclear physics and Density Functional Theory extensions

Even though since its inception DFT has been very successfully applied to many-body problems in solid state physics and chemistry, two major handicaps somewhat delayed its adoption into mainstream nuclear physics to the beginning of the 70's. To date, no functional in the Local Density Approximation or Generalized Gradient Approximation has been found which is able to reproduce shell effects, which appears as a major glitch since the correct prediction of the magic numbers is an essential part of any microscopic nuclear theory. It was soon realized, however, that the KS approach to the minimization of the energy functional gives qualitatively the desired shell effects, since it basically leads to a HF-like Schrödinger equation. Many years earlier, with the introduction of a very strong spin-orbit force, DFT was extended to explicitly include the spin degrees of freedom, giving birth to the spin-DFT. However, some of the strongest DFT theorems have not been proved rigorously for spin-DFT and are only known to hold qualitatively. In the non-relativistic approach, to introduce the spin degree of freedom, the density is replaced by a density matrix $\rho_{ss'}$ with $s = 1, 2$, and in the relativistic approach by a spinor density matrix $\rho_{ss'}$, $s = 1, \cdots, 4$. The advantage of using a relativistic theory is the natural appearance of the spin-orbit force term without any additional parameter or assumptions.

In addition to the spin, isospin plays a very important role in nuclear physics; the natural extension to the energy functional is to let it depend on the neutron and proton densities separately. This introduces a major complication over the case of condensed matter physics, where the electromagnetic interaction depends only on the charge density. In fact, in the search for an energy density functional able to quantitatively describe ground-state nuclear properties, many of such additional explicit density dependences have been identified. For example, the standard Skyrme [158] density functional depends on the neutron proton density, and in addition on the kinetic energy density τ and the spin density and currents J, and their derivatives. Because it is not possible to know *a priori* whether this extensions play an important role, and although there is a sound physical justification behind all these additions, the procedure is a trial and error quest to find better functionals.

On the relativistic side the standard procedure is to write an interaction Lagrangian with the desired degrees of freedom, and from there to derive an energy density functional as the basis for the minimization. For finite nuclei, this minimization procedure is always based on the KS approach, as will be briefly outlined in the next chapter. However, such a density functional is not enough to quantitatively describe nuclei. For example, nuclear superfluidity cannot be explained without particle-particle correlations. Thus, the inclusion of an abnormal density, which takes into account the effects of open-shells, is of the utmost importance; without it, the description of nuclei would be only of a very qualitative nature.

In the next chapter we will follow this path, first obtaining a density functional based on a relativistic Lagrangian which includes the minimum set of interactions able to reproduce basic nuclear features. To obtain quantitative agreement with experimental data, however, one needs to introduce an explicit density dependence in the interaction. This can be achieved using two different approaches: with the explicit inclusion of field non-linearities, or, alternatively, with density dependent field-nucleon couplings. We will present both methods, and then extend the density functional to include particle-particle correlations.

Chapter 3

Relativistic Density Functional Theory and the nuclear many-body problem.

"Before I came here I was confused about this subject. Having listened to your lecture I am still confused. But on a higher level."
— Enrico Fermi, 1901-1954

DFT was first applied to atomic systems, were in principle the interaction is known (the electromagnetic interaction). The picture in nuclear physics is not so encouraging because one major obstacle plagues a straightforward application of DFT, namely that the exact nuclear force has still, and despite almost half a century of study, not been completely determined.

The current trend in nuclear physics DFT is to use a purely phenomenological force, analogous to the approach used in the atomic physics case so successfully. As many symmetries as possible are included in a model functional that depends on as few parameters as possible. One then adjusts these parameters to bulk properties of nuclear matter and a few selected finite nuclei. The parameters set thus obtained can then be used over the whole nuclear chart, and the quantitative agreement with available experimental data is quite remarkable [158, 165, 58].

Historically known as Relativistic Mean Field (RMF) theory, Lorentz-invariant density functionals have been used to successfully describe many properties of nuclei.

Starting with a fully covariant effective Lagrangian, an energy density functional is constructed, and the Kohn-Sham theory applied to derive Hartree-like single-particle equations whose self-consistent solution give the ground-state density. The actual construction of the energy density functional is based on the Walecka model, which includes the minimal set of degrees of freedom to qualitatively reproduce basic nuclear properties such as saturation. Quantitative agreement with experiment is then achieved by extending the basic functional with explicit density dependences and pairing correlations.

3.1 Relativistic Mean Field (RMF) theory

In the Walecka model [165] and its extensions, nucleons are described as Dirac point particles that interact by the exchange of virtual mesons (or, in the case of point coupling models, contact terms). The energy functional that describes the dynamics of the nuclear system is derived from a fully covariant effective Lagrangian. The meson degrees of freedom are chosen as the minimum set of interactions required to properly describe the nuclear system properties, and are characterized by their characteristic quantum attributes: parity, spin and isospin. The meson masses and their coupling constants to the nucleons thus parametrize the actual interaction. The model used throughout this work is the simple (σ,ω,ρ,γ) model [121, 139]. An scalar-isoscalar field σ mediates the medium-range attraction between nucleons. It is an effective field whose origin lies in many complex effects, for example two-pion resonances and QCD combinations of quark-antiquark pairs and gluons. A vector-isoscalar field ω is introduced to model the short range repulsion. And finally the isospin dependence of the nuclear force is taken into account by a vector-isovector field ρ. In principle one should also include one-pion exchange in the formulation of the Lagrangian, as it is the basic ingredient of the nuclear force. However it does not enter at the classical Hartree-level because it leads to a parity-breaking field, which has not been observed in nuclei. However, as already stated, two-pion exchange is included in a phenomenological way within the σ field. The electromagnetic interaction is also taken into account by including the photon field γ, generated by the vector potential A_μ. The effective Lagrangian density can thus be written

$$\mathcal{L} = \mathcal{L}_N + \mathcal{L}_m + \mathcal{L}_{int} \tag{3.1}$$

where $\mathcal{L}_N$ refers to the free nucleon propagation

$$\mathcal{L}_N = \overline{\psi}(i\gamma^\mu \partial_\mu - m)\psi \tag{3.2}$$

$\mathcal{L}_m$ is the Lagrangian for the free meson and electromagnetic fields,

$$\begin{aligned}\mathcal{L}_m &= \frac{1}{2}\partial_\mu\sigma\partial^\mu\sigma - \frac{1}{2}m_\sigma^2\sigma^2 - \frac{1}{4}\Omega_{\mu\nu}\Omega^{\mu\nu} \\ &+\frac{1}{2}m_\omega^2\omega_\mu\omega^\mu - \frac{1}{4}\vec{R}_{\mu\nu}\vec{R}^{\mu\nu} + \frac{1}{2}m_\rho^2\rho_\mu\rho^\mu - \frac{1}{4}F_{\mu\nu}F^{\mu\nu}\end{aligned} \tag{3.3}$$

where the field tensors are defined as

$$\Omega_{\mu\nu} = \partial_\mu\omega_\nu - \partial_\nu\omega_\mu \tag{3.4}$$

$$\vec{R}_{\mu\nu} = \partial_\mu\vec{\rho}_\nu - \partial_\nu\vec{\rho}_\mu \tag{3.5}$$

$$F_{\mu\nu} = \partial_\mu A_\nu - \partial_\nu A_\mu \tag{3.6}$$

where the arrows indicate isovectors. And finally $\mathcal{L}_{int}$ is the nucleon-meson coupling interaction, which is restricted in this simple model to minimal linear coupling.

$$\mathcal{L}_{int} = -\bar{\psi}\Gamma_\sigma\sigma\psi - \bar{\psi}\Gamma_\omega^\mu\omega_\mu\psi - \bar{\psi}\Gamma_\rho^\mu\vec{\rho}_\mu\psi - \bar{\psi}\Gamma_e^\mu A_\mu\psi \tag{3.7}$$

where the vertexes Γ read

$$\Gamma_\sigma = g_\sigma, \qquad \Gamma_\omega^\mu = g_\omega\gamma^\mu, \qquad \Gamma_\rho^\mu = g_\rho\vec{\tau}\gamma^\mu, \qquad \Gamma_e^\mu = e\frac{1-\tau_3}{2}\gamma^\mu \tag{3.8}$$

with the nucleon-meson couplings g_σ, g_ω, g_ρ and e. The Hamiltonian density can be derived from the Lagrangian density as the (0,0) component of the energy-momentum tensor

$$\mathcal{H} = T^{00} = \frac{\partial\mathcal{L}}{\partial\dot{q}_j}\dot{q}_j - \mathcal{L} \tag{3.9}$$

leading the to the energy functional

$$E = \int \mathcal{H} d^3r \tag{3.10}$$

Following the Kohn-Sham approach of section (2.1.1), one can express the relativistic energy density E as a functional of the single particle density

$$\hat{\rho}(\mathbf{r},\mathbf{r}',t) = \sum_{i=1}^{A} |\psi_i(\mathbf{r},t)\rangle\langle\psi_i(\mathbf{r}',t)| \tag{3.11}$$

and the meson fields $\phi = (\sigma,\omega,\rho,\gamma)$, leading to the standard relativistic energy density functional E_{RMF}

$$E_{RMF}[\hat{\rho},\phi] = \mathrm{Tr}[(-i\boldsymbol{\alpha}\boldsymbol{\nabla} + \beta m)\rho] \pm \frac{1}{2}\int d^3r\,\left[(\partial_\mu\phi_m)^2 + m_m^2\right] + \mathrm{Tr}[(\Gamma_m\phi_m)\rho] \tag{3.12}$$

where summation over the mesons is implied, the trace operation involves summation over Dirac indices and an integral over the whole space and Γ_m describes the meson-nucleon interaction. At the mean field level the meson are treated as classical fields. The nucleons, described by a Slater determinant $|\Phi\rangle$ of single-particle wave functions, move independently in these classical meson fields. One can thus apply the classical time-dependent variational principle

$$\delta \int_{t_1}^{t_2} dt \{\langle \Phi | i\partial_t | \Phi \rangle - E[\rho, \phi_m]\} = 0 \tag{3.13}$$

that leads to the equations of motion

$$\begin{aligned} i\partial_t \rho &= [h[\rho, \phi], \rho] && (3.14)\\ \left[\partial^\mu \partial_\mu + m_m^2\right] \phi_m &= \pm \mathrm{Tr}\left[\Gamma_m \rho\right] && (3.15) \end{aligned}$$

where the single particle effective Dirac Hamiltonian h is the functional derivative of the energy with respect to the single particle density

$$h[\rho, \phi_m] = \frac{\delta E[\rho, \phi_m]}{\delta \rho} \tag{3.16}$$

Using the explicit expansion for the density (3.11) in terms of single particle wave functions the equations of motion (3.14) and (3.15) can be cast into the standard form

$$\begin{aligned} \left[\gamma^\mu (i\partial_\mu + V_\mu) + m + S\right] \psi &= 0 && (3.17)\\ \left[\Box + m_m^2\right] \phi_m &= \pm \sum_i \bar{\psi}_i \Gamma_m \psi_i && (3.18) \end{aligned}$$

where the scalar S and vector V_μ potentials are defined by

$$\begin{aligned} S &= \Sigma^s \\ V &= \Sigma_0^v + \Sigma_0^{tv} + eA^0 && (3.19) \end{aligned}$$

with the self-energies for the meson fields given by

$$\begin{aligned} \Sigma^s &= -g_\sigma \sigma && (3.20)\\ \Sigma_0^v &= g_\omega \omega^0 && (3.21)\\ \Sigma_0^{tv} &= g_\rho \tau_3 \rho_3^0 && (3.22) \end{aligned}$$

It is customary to define a set of densities and currents that act as the sources for the different meson fields in their respective equations (3.18), and label them accordingly. Thus, the source for the σ meson would be the *scalar* density, for the ω meson the *vector* current, and so on:

$$\begin{aligned}
&\text{scalar}-\text{isoscalar} && \rho_s=\sum_i^A\bar{\psi}\psi \\
&\text{vector}-\text{isoscalar} && j^\mu=\sum_i^A\bar{\psi}\gamma_\mu\psi \\
&\text{vector}-\text{isovector} && \vec{j}^\mu=\sum_i^A\bar{\psi}\gamma^\mu\vec{\tau}\psi \\
&\text{electromagnetic} && j_c^\mu=\sum_i^A\bar{\psi}\frac{1}{2}(1+\tau_3)\gamma^\mu\psi
\end{aligned} \tag{3.23}$$

In order to describe the ground state properties of nuclei, one has to look for stationary solutions of the equations of motion (3.14) and (3.15).

$$[h[\rho,\phi_m],\rho]=0 \tag{3.24}$$

$$\left[-\Delta+m_m^2\right]\phi_m=\pm\sum_i\bar{\psi}_i\Gamma_m\psi_i \tag{3.25}$$

The source densities and currents then retain only the time-like components

$$\begin{aligned}
&\text{scalar}-\text{isoscalar} && \rho_s=\sum_i^A\bar{\psi}\psi \\
&\text{vector}-\text{isoscalar} && \rho_v=\sum_i^A\bar{\psi}\gamma^0\psi \\
&\text{vector}-\text{isovector} && \rho_{tv}=\sum_i^A\bar{\psi}\gamma^0\tau_3\psi \\
&\text{electromagnetic} && \rho_c=\sum_i^A\bar{\psi}\frac{1}{2}(1+\tau_3)\psi
\end{aligned} \tag{3.26}$$

and the nucleon wave functions are then the eigenvectors of the stationary Dirac equation,

$$\left[-i\boldsymbol{\alpha}\boldsymbol{\nabla}+V_0+\beta(m+S)\right]\psi_k=\varepsilon_k\psi_k \tag{3.27}$$

which yields the single particle energies ε_k as eigenvalues. Because we are restricting ourselves to the study of even-even nuclei, we have taken advantage of the fact that in that case there are no net currents, and the corresponding spatial components of the vector potential V vanish. Equation (3.27) together with equations (3.25) pose a self-consistent problem. Starting with an initial guess for the potentials S and V, one solves the Dirac equation (3.27) for ψ_k, which in turn are used to calculate the source terms in the meson equations (3.25). Solving for the fields, new scalar S and vector V are obtained, and the cycle repeated until convergence has been achieved. With the resulting density ρ and fields ϕ, the total energy of the system can be calculated using (3.12), as well as other bulk properties of the nucleus, like radii. The total binding energy thus obtained has to be corrected by the microscopic estimate for the energy of the center-of-mass motion

$$E_{cm} = -\frac{\langle P_{cm}^2 \rangle}{2Am} \tag{3.28}$$

where P_{cm} is the total momentum of a nucleus with A nucleons [16]. It should also be noted that in the calculation of the sources for the meson equations (3.25) only positive energy spinors are included in the summation. This is the so-called *no-sea approximation*. In a fully relativistic description also the negative energy states from the Dirac sea would have to be included. However, this would lead to divergent terms which can only be removed by a proper renormalization procedure. However, then one obtains a set of equations that can only be solved numerically [61] for finite nuclei, although an analytical solution for infinite nuclear matter can be found [38]. Numerical studies have shown that effects due to vacuum polarization can be as large as 20%-30%. Their inclusion requires a readjustment of the parameter set for the effective Lagrangian that leads to approximately the same results as if they were neglected [68, 166, 172], i.e. they are taken into account in the parameters in a global fashion. Therefore the *no-sea approximation* is used in almost all practical applications of relativistic Density Functional Theory. It will have, however, serious consequences in the application of the Random Phase Approximation for the calculation of excited states.

3.2 Density dependence

Even in the earliest applications of the simple Walecka model, it was realized, that this simple linear interaction density functional did not provide a quantitative description of complex nuclear systems. An effective density dependence must be introduced, which gave birth to the different density-dependent relativistic energy density functionals. Two basic procedures have been used to that purpose. Historically the first was the introduction of non-linear self-interaction terms in the meson part of the Lagrangian. These functionals will be labeled from now on as Non Linear Meson Exchange functionals, or NLME for short. The other approach is to include the density dependence in the meson-nucleon couplings, retaining linearity in the Lagrangian. These will be referred to as Density Dependent Meson Exchange (DDME) functionals. In addition, and latest to be developed, expansion of the meson propagator into zero-range couplings and gradient correction terms results in point coupling functionals. These will be referred as Density Dependent Point Coupling (DDPC) functionals.

3.2.1 Meson exchange with non-linear σ-meson self-interaction (NLME functionals)

First introduced by Boguta and Bodmer [22], the quadratic σ-potential $\frac{1}{2}m_\sigma^2\sigma^2$ in (3.3) is replaced with a quartic potential

$$\frac{1}{2}m_\sigma^2\sigma^2 \rightarrow U_\sigma(\sigma) = \frac{1}{2}m_\sigma^2\sigma^2 + \frac{g_2}{3}\sigma^3 + \frac{g_3}{4}\sigma^4 \tag{3.29}$$

that includes the non-linear σ self-interactions in a phenomenological fashion with two additional parameters g_2 and g_3. The only practical difference with the linear relativistic density functional is that an additional term appears in the σ field equation, and becomes, in the time independent case,

$$\left[-\Delta + U'_\sigma(\sigma)\right]\phi = \rho_s \tag{3.30}$$

with

$$U'_\sigma(\sigma) = m_\sigma^2 + g_2\sigma^2 + g_3\sigma^3 \tag{3.31}$$

which renders it unsolvable analytically and one has to resort to numerical techniques [130]. The adjustment of the non-linear parameters g_2 and g_3 to surface properties of finite nuclei gives, in many practical cases, a negative value for the parameter g_3, leading to an unstable theory. However, in the limit of moderate densities, as found in normal nuclei, the σ field is small, and the potential $U(\sigma)$ attractive, which results in a reasonable solution [22, 130].

This particular form of the non-linear potential has become standard in realistic applications of relativistic Density Functional Theory to nuclei, although additional non-linear interaction terms, both in the isoscalar and isovector channels, have been considered [161]. The problem with the inclusion of additional interaction terms is, however, that the empirical data set of bulk and single-particle properties of finite nuclei can only determine six or seven parameters in the general expansion of the effective Lagrangian in powers of the fields and their derivatives [161].

There are eight free parameters in the non-linear σ-meson density functional: the meson masses m_σ, m_ω, m_ρ, and their coupling constants.g_σ, g_2, g_3, g_ω, and g_ρ. The mass of the ρ meson is fixed to the experimental value, i.e.

$$m_\rho = 763.0\,\mathrm{MeV} \tag{3.32}$$

while for the proton and neutron nuclear masses the average value of empirical masses is taken to be

$$m = 939.0\,\mathrm{MeV} \tag{3.33}$$

NL3		
m	939.0	MeV
m_σ	508.194	MeV
m_ω	782.501	MeV
g_σ	10.217	
g_ω	12.868	
g_ρ	4.474	
g_2	-10.431	fm^{-1}
g_3	-28.885	

Table 3.1: NL3 parameter set for the non-linear σ-meson energy density functional [83].

This reduces the number of free parameters of the model to seven, which are fitted to experimental ground state properties. In the present investigation the NL3 parameter set (see Table 3.1) will be used as representative of the non-linear σ-meson relativistic energy density functionals. It has been used extensively to study the nuclear structure phenomena from light to super-heavy elements, both in stable and exotic nuclei. Special care was taken to fit the parameters not only to ground state properties of stable nuclei, but also of ^{132}Sn and ^{214}Pb to obtain an improved isospin dependence of the interaction for unstable nuclei [83].

3.2.2 Meson exchange with density dependant couplings constants (DDME functionals)

The limitations of the standard non-linear σ-meson effective interactions presented in the previous section are well known, even for nuclei close to the stability line. They are more pronounced in the isovector channel, which is poorly constrained by the available experimental data. It is also well known that they predict an equation of state of neutron matter that is very different from the standard microscopic many-body neutron matter equation of state of Friedman and Pandharipande [52].

In order to overcome the limitations of the standard non-linear functionals, several solutions have been proposed. One, already commented in the previous section, is to include additional self-interaction terms in the isovector and isoscalar channels. Another possibility is to formulate an effective theory with medium dependent meson-nucleon couplings. In such a theory the couplings g_σ, g_ω and g_ρ are assumed to be vertex functions of Lorentz scalar bilinear forms of the nucleon operators. In most applications they depend on the vector density

$$\rho_v = \sqrt{j_\mu j^\mu}, \qquad \text{with} \quad j_\mu = \bar{\psi}\gamma_\mu\psi \tag{3.34}$$

The other obvious choice would be the scalar density, but it has been shown, however, that the vector density dependence gives better results for finite nuclei [54], and provides a more natural relation to the microscopic self-energies of Dirac-Brueckner theory [66]. The basic interaction Lagrangian is thus (3.7) where now the nucleon-meson couplings exhibit a dependence on the vector density (3.34). This dependence produces a vector rearrangement self-energy $\Sigma_\mu^{v,R}$ that has to be added to the vector potential V

$$\Sigma_\mu^{v,R} = \frac{j_\mu}{\rho_v}\left(\frac{\partial g_\sigma}{\partial \rho_v}\bar{\psi}\psi\sigma + \frac{\partial g_\omega}{\partial \rho_v}\bar{\psi}\gamma^\nu\psi\omega_\nu + \frac{\partial g_\rho}{\partial \rho_v}\bar{\psi}\gamma^\nu\vec{\tau}\psi\vec{\rho}_\nu\right) \tag{3.35}$$

which reduces in the stationary case to

$$\Sigma_0^{v,R} = \frac{\partial g_\sigma}{\partial \rho_v}\rho_s\sigma + \frac{\partial g_\omega}{\partial \rho_v}\rho_v\omega^0 + \frac{\partial g_\rho}{\partial \rho_v}\rho_{tv}\rho_3^0 \tag{3.36}$$

with the densities defined in (3.26). Thus the scalar S and vector V potentials in the Dirac equation read

$$\begin{aligned} S &= \Sigma^s \\ V &= \Sigma_0^v + \Sigma_0^{tv} + eA^0 + \Sigma_0^{v,R} \end{aligned} \tag{3.37}$$

Even though the density dependence of the nucleon-meson couplings can, in principle, be obtained from microscopic Dirac Brueckner (DB) calculations [66, 43], only qualitative agreement is found when calculating ground-state properties of finite nuclei. A better approach [154] is to choose an ansatz that encloses the different DB results but leaves the parameters of the density dependence free to be fitted to properties of nuclear matter and finite nuclei. The most often used functional form for the σ and ω mesons is

$$g_i(\rho_v) = g_i(\rho_{sat})f(x_i) \qquad \text{for} \quad i = \sigma, \omega \tag{3.38}$$

where

$$f(x_i) = a_i\frac{1 + b_i(x + d_i)^2}{1 + c_i(x + d_i)^2} \tag{3.39}$$

is a function of $x_i = \rho_i/\rho_{sat}$, and ρ_{sat} denotes the saturation density of symmetric nuclear matter. Not all parameters in (3.39) are independent. From (3.38) it is fairly obvious that

$$f_i(1) = 1 \tag{3.40}$$

	DD-ME2	
m_σ	555.1238	MeV
m_ω	783.0000	MeV
m_ρ	763.0000	MeV
$g_\sigma(\rho_{sat})$	10.5396	
$g_\omega(\rho_{sat})$	13.0189	
$g_\rho(\rho_{sat})$	3.6836	
a_σ	1.3881	
b_σ	1.0943	
c_σ	1.7057	
d_σ	0.4421	
a_ω	1.3892	
b_ω	0.9240	
c_ω	1.4620	
d_ω	0.4775	
a_ρ	0.5647	

Table 3.2: DD-ME2 parameter set for the density dependent meson exchange relativistic energy functional [81, 103].

Also, in reference [54] the following restrictions are imposed

$$f''_\sigma(1) = f''_\omega(1) \tag{3.41}$$

$$f''_i(0) = 0 \tag{3.42}$$

in order to keep the number of parameters of the density dependence down to three. The last condition also guarantees that the rearrangement contribution becomes finite at zero density. In the parametrizations used in the present investigation (Table 3.2), b_σ, d_σ and b_ω were chosen as the independent parameters of (3.39), plus the two values for the couplings at saturation density, $g_\sigma(\rho_{sat})$ and $g_\omega(\rho_{sat})$, making a total of five parameters for the isoscalar channel. The functional form for the ρ-meson coupling is taken from DB calculations of asymmetric nuclear matter [43].

$$g_\rho(\rho) = g_\rho(\rho_{sat})e^{-a_\rho(x-1)} \tag{3.43}$$

That adds two more parameters, $g_\rho(\rho_{sat})$ and a_ρ, in the isovector channel. The ω and ρ meson masses are the standard bare masses $m_\omega = 783\,\text{MeV}$ and $m_\rho = 763\,\text{MeV}$, while the σ meson mass is a free parameter. It adds up to eight parameters in total. Compared to the standard non-linear σ model, one more parameter is included in the isovector channel, and a better description of isovector properties of nuclear matter and finite nuclei is obtained [103].

3.2.3 Point coupling with density dependant couplings constants (DDPC functionals)

Similar to the finite range relativistic density functional approach, the DDPC functionals consider an effective Lagrangian for nuclear mean-field calculations at the Hartree level with the *no-sea* approximation. Instead of modeling the interaction by the exchange of mesons, in DDPC the model consists in four-, six- and eight-fermion point couplings (contact interactions) together with derivative terms representing, respectively, two-, three- and four-body forces and the finite ranges of the corresponding mesonic interactions. In many applications, however, the three- and four-body forces can be modeled by density dependent two-body coupling constants whose dependence is polynomial. In fact, DDPC functionals are closely related to finite range relativistic functionals. Expanding the finite range meson propagators into a zero-range coupling plus gradient corrections we can link both. For example, for the σ-meson

$$\frac{-g_\sigma^2}{-\Delta + m_\sigma^2}\rho_s \approx \frac{-g_\sigma^2}{m_\sigma^2}\rho_s + \frac{-g_\sigma^4}{m_\sigma^4}\Delta\rho_s \tag{3.44}$$

It is usual practice to define a new set of coupling constants $\mathcal{G}$ and δ such that

$$\begin{aligned} \mathcal{G}_m &= \frac{g_m^2}{m_m^2} \\ \delta_m &= \frac{g_m^4}{m_m^4} \end{aligned} \tag{3.45}$$

In general the Lagrangian for these point coupling models can be written as

$$\mathcal{L} = \mathcal{L}_N + \mathcal{L}_{int} + \mathcal{L}_{em} \tag{3.46}$$

where, naturally, the mesons are missing. The Lagrangian for the free nucleons $\mathcal{L}_N$ remains the same as (3.2), and the interaction Lagrangian $\mathcal{L}_{int}$ has the form

$$\begin{aligned} \mathcal{L}_{int} = & -\frac{1}{2}\mathcal{G}_s\left(\bar{\psi}\psi\right)\left(\bar{\psi}\psi\right) - \frac{1}{2}\mathcal{G}_v\left(\bar{\psi}\gamma_\mu\psi\right)\left(\bar{\psi}\gamma^\mu\psi\right) \\ & -\frac{1}{2}\mathcal{G}_{ts}\left(\bar{\psi}\vec{\tau}\psi\right)\cdot\left(\bar{\psi}\vec{\tau}\psi\right) - \frac{1}{2}\mathcal{G}_{tv}\left(\bar{\psi}\gamma_\mu\vec{\tau}\psi\right)\cdot\left(\bar{\psi}\gamma^\mu\vec{\tau}\psi\right) \\ & -\frac{1}{2}\delta_s\left(\partial_\nu\bar{\psi}\psi\right)\left(\partial^\nu\bar{\psi}\psi\right) - \frac{1}{2}\delta_v\left(\partial_\nu\bar{\psi}\gamma_\mu\psi\right)\left(\partial^\nu\bar{\psi}\gamma^\mu\psi\right) \\ & -\frac{1}{2}\delta_{ts}\left(\partial_\nu\bar{\psi}\vec{\tau}\psi\right)\cdot\left(\partial^\nu\bar{\psi}\vec{\tau}\psi\right) - \frac{1}{2}\delta_{tv}\left(\partial_\nu\bar{\psi}\gamma_\mu\vec{\tau}\psi\right)\cdot\left(\partial^\nu\bar{\psi}\gamma^\mu\vec{\tau}\psi\right) \end{aligned} \tag{3.47}$$

Finally, the electromagnetic interaction

$$\mathcal{L}_{em} = -\bar{\psi}\Gamma_e^\mu A_\mu\psi - \frac{1}{4}F_{\mu\nu}F^{\mu\nu} \tag{3.48}$$

with Γ_e^μ defined in (3.8). In most applications [12, 71], the coupling constants $\mathcal{G}$ exhibit a polynomial density dependence, but unlike in the DDME functionals, each one depends on its density (3.26)

$$\mathcal{G}_i(\rho_i) = \alpha_i + \beta_i \rho_i + \gamma_i \rho_i^2, \qquad i = s, v, ts, tv \tag{3.49}$$

The scalar S and vector V potentials for the Dirac equation are

$$\begin{aligned} S &= \Sigma^s + \Sigma^{ts} \\ V &= \Sigma_0^v + \Sigma_0^{tv} + eA^0 \end{aligned} \tag{3.50}$$

with the self energies

$$\begin{aligned} \Sigma^s &= \alpha_s \rho_s + \beta_s \rho_s^2 + \gamma_s \rho_s^3 + \delta_s \Delta \rho_s && (3.51) \\ \Sigma^v &= \alpha_v \rho_v + \beta_v \rho_v^2 + \gamma_v \rho_v^3 + \delta_v \Delta \rho_v && (3.52) \\ \Sigma^{ts} &= \alpha_{ts} \rho_{ts} + \beta_{ts} \rho_{ts}^2 + \gamma_{ts} \rho_{ts}^3 + \delta_{ts} \Delta \rho_{ts} && (3.53) \\ \Sigma^{tv} &= \alpha_{tv} \rho_{tv} + \beta_{tv} \rho_{tv}^2 + \gamma_{tv} \rho_{tv}^3 + \delta_{tv} \Delta \rho_{tv} && (3.54) \\ & && (3.55) \end{aligned}$$

The total number of possible parameters is thus sixteen, but the most common parametrizations (see Table 3.3) use a number comparable to the DDME models, ranging from nine to eleven. However, the real world performance of this type of functionals is inferior when compared to the excellent predictive power of the NLME and DDME functionals. This is partly due to their recent development and the lack of good parametrizations. However, the simplicity of the DDPC functionals, and the reduced numerical complexity required in the actual implementation, mark them as very good candidates for future development.

3.3 Relativistic Hartree Bogoliubov (RHB) theory

In nuclei with open shells the Relativistic Mean Field picture of independent nucleons moving in an average potential is no longer a sufficient picture. In many cases, the gap in the single-particle energy spectrum prevents the independent particle picture from breaking down. In particular, doubly closed shell nuclei have a large energy gap and for them the Mean Field solution is especially good, since it takes a lot of energy to scatter particles out of their orbitals. However, for the rest of nuclei, the MF solution may have a small energy gap and completely lack such stability. In many of those cases, allowing the Mean Field solution to deform restores the energy gap. Even then that is generally not enough to sustain the independent particle picture. The static field used in the MF description corresponds to the low multipoles of an expansion of the

	PC-F1	
α_s	-3.83577 $\cdot 10^{-4}$	MeV^{-2}
β_s	7.68567 $\cdot 10^{-11}$	MeV^{-5}
γ_s	-2.90443 $\cdot 10^{-17}$	MeV^{-8}
δ_s	-4.1853 $\cdot 10^{-10}$	MeV^{-4}
α_v	2.59333 $\cdot 10^{-4}$	MeV^{-2}
γ_v	-3.879 $\cdot 10^{-18}$	MeV^{-8}
δ_v	-1.1921 $\cdot 10^{-10}$	MeV^{-4}
α_{ts}	-.-	
δ_{ts}	-.-	
α_{tv}	3.4677 $\cdot 10^{-5}$	MeV^{-2}
α_{tv}	-4.2 $\cdot 10^{-11}$	MeV^{-4}

Table 3.3: PC-F1 parameter sets for the density dependent point coupling functional [33].

two-body force, and so the inclusion of deformations is an attempt to take into account as much as possible from the two-body interaction. In competition with the effect of the long range field forces, the short range forces try to scatter particles out of their independent-particle orbitals. These short range correlations are totally neglected in the pure Mean Field approach. In general, the pairing correlations are accounted for in the quasi particle picture by the introduction of an additional field, i.e. the pairing potential. They cannot be included in the classical Lagrangian because at that level it does not contain terms of the form $\psi^\dagger\psi^\dagger$. In order to include pairing correlations in a microscopic way, the meson fields need to be quantized, so as to gain one meson exchange two-body forces [79]. One can, however, follow a phenomenological approach and introduce a generalized density $\mathcal{R}$ [157]

$$\mathcal{R} = \begin{pmatrix} \rho & \kappa \\ -\kappa^\star & 1-\rho^\star \end{pmatrix} \tag{3.56}$$

where ρ is the single-particle density and κ is the pair density, defined as

$$\begin{aligned} \rho_{ij} &= \langle\Phi|c_j^\dagger c_i|\Phi\rangle \\ \kappa_{ij} &= \langle\Phi|c_j c_i|\Phi\rangle \end{aligned} \tag{3.57}$$

such that the ground state of a nucleus $|\Phi\rangle$ can be represented as a vacuum with respect to the operators

$$\alpha_k\,|\Phi\rangle = 0 \tag{3.58}$$

The most general form for α such that its associated single particle density is non-zero is

$$\alpha_k^\dagger = \sum_k U_{mk}c_m^\dagger + V_{mk}c_m \tag{3.59}$$

where U_{mk} and V_{mk} are the so called Hartree-Bogoliubov coefficients, and determine the single particle density matrix

$$\rho_{ij} = \sum_k V^*_{ik} V_{jk} \tag{3.60}$$

and the pairing density

$$\kappa_{ij} = \sum_k U^*_{ik} V_{jk} \tag{3.61}$$

In a DFT approach, one can extend the energy functional and make it depend also on the pairing density

$$E[\rho, \kappa, \phi] = E_{RMF}[\rho, \phi] + E_{pair}[\kappa] \tag{3.62}$$

where E_{RMF} is one of the functionals introduced in the preceding sections. In addition, the pairing energy density E_{pair} is also included. It can be written in a general form as

$$E_{pair}[\kappa] = \frac{1}{4}\mathrm{Tr}[\kappa V^{pp} \kappa] \tag{3.63}$$

The equations of motion (3.14) and (3.15) now depend on the generalized density $\mathcal{R}$

$$i\partial_t \mathcal{R} = [\mathcal{H}(\mathcal{R}, \phi), \mathcal{R}] \tag{3.64}$$

where $\mathcal{H}$ is the generalized single-particle field, i.e. the Hartree-Bogoliubov effective Hamiltonian

$$\mathcal{H} = \frac{\delta E}{\delta \mathcal{R}} = \begin{pmatrix} h_D - m - \lambda & \Delta \\ -\Delta^* & -h_D + m - \lambda \end{pmatrix} \tag{3.65}$$

The Relativistic Hartree Bogoliubov effective Hamiltonian contains now two average potentials: the self-consistent mean field h_D, which encloses all the long range particle-hole correlations, and the pairing field Δ, which includes the short range particle-particle correlations. The former results from the variation of the energy functional with respect to the normal density ρ, and the later from the variation with respect to the abnormal density κ

$$h_D = \frac{\delta E}{\delta \rho} \qquad \Delta = \frac{\delta E}{\delta \kappa} \tag{3.66}$$

The ground state is obtained from the static limit of (3.64), i.e. the Hartree-Bogoliubov equations

$$\begin{pmatrix} h_D - m - \lambda & \Delta \\ -\Delta^* & -h_D + m - \lambda \end{pmatrix} \begin{pmatrix} U_k \\ V_k \end{pmatrix} = E_k \begin{pmatrix} U_k \\ V_k \end{pmatrix} \tag{3.67}$$

When the pairing force is diagonal in the Hartree basis defined by h_D, the general Bogoliubov-Valatin transformation (3.59) simplifies to

$$\alpha^\dagger_k = u_k a^\dagger_k - v_k a^\dagger_{\bar{k}} \tag{3.68}$$

with the usual normalization condition

$$u_k^2 + v_k^2 = 1 \tag{3.69}$$

In general, when the off-diagonal elements of the pairing interaction, in the Hartree basis, are small when compared to the diagonal ones, they can be neglected at each iteration step in the self-consistent process, leading to the BCS approximation and the simplification of the Bogoliubov-Valatin transformation. In that case, the HFB equation decouples into a set of two independent equations, one for the self-consistent mean field h_D which is identical to the usual RMF one but with an additional Lagrange parameter λ to preserve the number of particles, and the so called gap equation

$$\Delta_{k\bar{k}} = -\frac{1}{2}\sum_{k>0} V^{ph}_{k\bar{k}k'\bar{k}'} \frac{\Delta_{k'\bar{k}'}}{\sqrt{(\epsilon_k - \lambda)^2 + \Delta^2_{k\bar{k}}}} \tag{3.70}$$

that together with the particle number constraint,

$$2\sum_{k>0} v_k^2 = N \tag{3.71}$$

the Dirac equation (3.27) and the meson equations (3.25) define the self-consistent stationary problem. The coefficients for the Bogoliubov-Valatin transformation u and v can be readily calculated from the last two equations and read

$$\begin{aligned} u_k^2 &= \frac{1}{2}\left\{1 + \frac{\epsilon_k - \lambda}{\sqrt{(\epsilon_k - \lambda)^2 + \Delta^2_{k\bar{k}}}}\right\} \\ v_k^2 &= \frac{1}{2}\left\{1 - \frac{\epsilon_k - \lambda}{\sqrt{(\epsilon_k - \lambda)^2 + \Delta^2_{k\bar{k}}}}\right\} \end{aligned} \tag{3.72}$$

with the quasi-particle energies E_k defined by

$$E_k = \sqrt{(\epsilon_k - \lambda)^2 + \Delta^2_{k\bar{k}}} \tag{3.73}$$

The source densities for the meson equations have to be modified accordingly to take into account each single-particle occupation factor v_i in the following way

$$\begin{aligned}
\rho_s &= \sum_i v_i^2 \bar{\psi}\psi \\
j^\mu &= \sum_i v_i^2 \bar{\psi}\gamma_\mu\psi \\
\vec{j}^\mu &= \sum_i v_i^2 \bar{\psi}\gamma^\mu\vec{\tau}\psi \\
j_c^\mu &= \sum_i v_i^2 \bar{\psi}\frac{1}{2}(1+\tau_3)\gamma^\mu\psi
\end{aligned} \tag{3.74}$$

The effective pairing force V^{pp} in its simplest form, and the approach taken in this investigation, is to use a monopole pairing force. This corresponds to a truncation to first order in the multipole expansion of the short range correlations, keeping only the $J = 0$ term. While this is often a good approximation for the description of nuclei close to the valley of β-stability, it does not provide a correct description for the scattering of nucleon pairs from bound states to the energy continuum [70]. This effect becomes more important as the Fermi level comes closer to the particle continuum in nuclei close to the drip lines. Nevertheless, as a first approximation to the problem it suffices as it lays the ground work for a more complete description that can be implemented later on. Thus, restricting to a monopole pairing force, the interaction V^{pp} can be written as

$$V^{pp} = -G\ \delta_{i\bar{i}}\delta_{j\bar{j}} \tag{3.75}$$

where the bar refers to time reversed states and G is the pairing constant, which is different for neutrons and protons. Because the monopole V^{pp} is diagonal in the Hartree basis defined by h_D, this leads to a BCS-like pairing theory. This special ansatz for V^{pp} modifies the gap equation to

$$\frac{G}{2}\sum_{k>0}\frac{1}{\sqrt{(\epsilon_k-\lambda)^2+\Delta^2}} = 1 \tag{3.76}$$

where the gap parameter Δ is the same for all the levels in the basis space and the pairing constants G specify the strength of the pairing interaction. This pairing scheme has the advantage of being extremely simple. However, it has the undesired property of depending on the configuration basis chosen to solve the static equations. In particular, equation (3.76) is unbound in the sense that all the levels in the basis contribute to the pairing energy, not only those close to the Fermi energy. Thus, in order to make the pairing energy non-divergent, it is important to introduce a cutoff factor that restricts the sum in (3.76) to the vicinity of the Fermi surface. The approach taken in the present investigation includes a smooth cutoff having a Fermi shape [78]

$$f_i^2 = \frac{1}{1 + e^{(\epsilon_i - \lambda - \Delta\epsilon)/\mu}} \tag{3.77}$$

The values for the parameters are fixed throughout this investigation to $\mu = 0.5\,\text{MeV}$ and $\Delta\epsilon = 10\,\text{MeV}$. In reference [78] it was shown that the final results do not depend crucially on the actual values chosen for these parameters as long as they were reasonable. The gap equation and the occupation probabilities have to be modified accordingly

$$1 = \frac{G}{2} \sum_{k>0} \frac{f_k}{\sqrt{(\epsilon_k - \lambda)^2 + f_k \Delta^2}} \tag{3.78}$$

$$v_k^2 = \frac{1}{2} \left\{ 1 - \frac{\epsilon_k - \lambda}{\sqrt{(\epsilon_k - \lambda)^2 + f_k \Delta_{k\bar{k}}^2}} \right\} \tag{3.79}$$

Throughout this investigation the strength constants G of the pairing monopole interaction have been adjusted in all cases using a simple three point formula to the experimental pairing gaps [133].

As a final remark, it is worth remembering that, according to the theorem of Bloch and Messiah [18], any RHB wave function can be written either in the quasiparticle basis as a product of independent quasiparticle states, or in the canonical basis as a highly correlated BCS-state. The canonical basis can be uniquely determined imposing that it diagonalizes simultaneously the density *and* the single-particle Hamiltonian h_D. Thus, even if the RHB equation formally reduces to a BCS-like relativistic mean-field theory in the canonical basis, it is *not* an approximation. It is important to stress this fact, as in the next chapter we will develop the Quasiparticle Random Phase Approximation on top of the canonical basis, which is formally identical to a BCS-like theory. However, the Relativistic Quasiparticle Random Phase Approximation presented in this document is a full Hartree-Bogoliubov theory as long as one works in the canonical basis.

Chapter 4

Relativistic Quasiparticle Random Phase Approximation (RQRPA)

"The optimist thinks this is the best of all possible worlds. The pessimist fears it is true."
— J. Robert Oppenheimer, 1904-1967

The nuclear excitation spectra have played a crucial role in our understanding of the structure of nuclei. Unlike the situation in atomic physics, it was soon realised that the response of the nuclear system to external stimuli could not be fully explained in the simple framework of shell model single particle excitations. It was argued that many of the missing features observed in experimental nuclear spectra could only be explained by assuming a "coherent" participation by many nucleons, in a similar fashion to the shape vibrations in the nuclear liquid-drop model. Amongst nuclear excitations, those which represent the collective motion of many nucleons have given us the most valuable insight into general gross properties of the nuclear system.

The best known example is the Giant Dipole Resonance, which has been observed throughout the whole periodic table and represents the vibration of neutrons against protons. Over the years many more of such collective excitations have been proposed, identified and analysed, ranging from vibrations of the local density like the *breathing modes* (which involves variations of the density over the whole nuclear volume) or surface quadrupole modes, to spin excitations (spin waves), changes in the nuclear charge (e.g. analog resonances) that correspond to polarization waves in the nucleus, or isospin flip processes (e.g. Gamov-Teller resonances).

On the theoretical front, many theories have been proposed for the study of nuclear excitations. In the context of mean field theories, the obvious path to follow is to extend the formalism to the time-dependent domain. In modern terms, this implies the formulation of the Time Dependent Density Functional Theory. In particular, the small amplitude limit of the TDDFT, the Random Phase Approximation, is the simplest theory of excited states of the nucleus which takes into account the highly correlated nature of nucleons in the many-body system which represents the nucleus.

Conceptually, the Random Phase Approximation in the context of the nuclear many-body system is the application of the harmonic approximation to the time-dependent many-body problem. Technically it involves the expansion, to linear order, of the time-dependent density that describes the evolution of the nucleus around the ground state density, and the subsequent decomposition of the approximate system in its normal modes. Amongst the many nice formal properties, one of the biggest advantages of the RPA is that it guarantees current conservation. In particular, it automatically restores the symmetries that were spontaneously broken in the mean field approximation, separating the Goldstone modes out at the correct zero energy.

In addition, the RPA is the simplest theory of excited states of the nucleus which admits the possibility that the ground state is not of purely independent particle character but may contain correlations, associated with vibrational zero-point motions. In the time-dependent picture, the wave-function of the system $\Phi(t)$ stays always a product state, a quasiparticle vacuum. However, the quasiparticle operators $\alpha^\dagger(t)$ now depend on time. Expanding the time-dependent quasiparticles in terms of the static ground-state quasiparticle operators $\alpha^\dagger$, for completeness one has to admit $\alpha^\dagger\alpha^\dagger$ terms as well as $\alpha\alpha$ terms. Thus, it is obvious the implicit assumption that the *true* ground state is *not* simply a quasiparticle vacuum, and therefore the resulting bosons are of the form

$$B^\dagger = \sum_{kk'} \mathcal{X}_{kk'}\alpha^\dagger_k\alpha^\dagger_{k'} + \mathcal{Y}_{kk'}\alpha_k\alpha_{k'} \tag{4.1}$$

and the correlated RPA ground state is defined as the vacuum with respect to these bosons

$$|\mathrm{RPA}\rangle = e^{\sum_{kk'} \mathcal{Z}_{kk'}B^\dagger_k B^\dagger_{k'}}\,|\mathrm{HB}\rangle \tag{4.2}$$

Therefore, it cannot be a simple product state of quasiparticle operators, but it must contain complicated linear combinations of quasiparticle pairs. When the RPA ground state is calculated in the mean-field or HB approximations, this results in the usually known as "*quasi-boson approximation*" [31, 30]. The name comes from the fact that it is equivalent to neglecting the Pauli principle [133].

In particular, in this chapter the relativistic extension of the QRPA, the Relativistic Quasiparticle Random Phase Approximation (RQRPA) will be derived. It can be shown [132] that it corresponds to the small amplitude limit of the Time Dependent Relativistic Mean Field (TDRMF). From the point of view of the argument presented in last paragraph, it is clear that, for mathematical consistency and completeness in the expansion of the time-dependent quasiparticle operators, if the *no-sea* approximation is used in the ground-state calculation, it has to be considered as well at the RPA level. This means that the Dirac sea of negative energy states is also taken into account when constructing the configuration space, i.e. in addition to the configurations built from two quasiparticle states of positive energy, one has to consider also pairs formed from the fully or partially occupied states of positive energy and the empty negative energy states from the Dirac sea.

4.1 Matrix equation of the RQRPA

In the previous chapter, the ground state of a nucleus was characterized by the solution of the static RHB equations. For the study of excitation phenomena, knowledge of the time-dependent density $\rho(t)$ is necessary. It will be assumed that the generalized density at any time corresponds to a Slater determinant (i.e., $\mathcal{R}^2 = \mathcal{R}$). It can be shown then that it obeys the following equation of motion

$$i\partial_t \mathcal{R} = [\mathcal{H}[\mathcal{R}], \mathcal{R}] \tag{4.3}$$

Considering only small oscillations around the ground state density $\mathcal{R}_0$, the generalized time-dependant density, up to linear order, can be written as

$$\mathcal{R}(t) = \mathcal{R}_0 + \delta\mathcal{R}(t) \tag{4.4}$$

where $\mathcal{R}_0$ is the ground state generalized density. Substituting the expansion in the equation of motion (4.3) and retaining terms to linear order we obtain

$$i\partial_t \mathcal{R} = [\mathcal{H}_0, \delta\mathcal{R}] + \left[\frac{\delta\mathcal{H}}{\delta\mathcal{R}}\delta\mathcal{R}, \mathcal{R}_0\right] \tag{4.5}$$

Considering only small harmonic oscillations around the ground state with eigenfrequencies Ω_ν and admixtures $\delta\mathcal{R}$, the time dependent transition density $\mathcal{R}(t)$ reads

$$\delta\mathcal{R}(t) = \sum_\nu \delta\mathcal{R}^{(\nu)} e^{-i\Omega_\nu t} + \delta\mathcal{R}^{(\nu)\dagger} e^{i\Omega_\nu t} \tag{4.6}$$

Since $\mathcal{R}(t)$ is a projector at all times, $\mathcal{R}^2 = \mathcal{R}$ must hold, which to linear order implies

$$\mathcal{R}_0 \delta\mathcal{R} + \delta\mathcal{R}\mathcal{R}_0 = \delta\mathcal{R} \tag{4.7}$$

In the quasiparticle basis $\mathcal{R}_0$ is diagonal having the following form

$$\mathcal{R} = \begin{pmatrix} 0 & 0 \\ 0 & 1 \end{pmatrix} \tag{4.8}$$

so it follows that $\delta\mathcal{R}$ takes the form

$$\delta\mathcal{R} = \begin{pmatrix} 0 & \mathcal{X} \\ \mathcal{Y} & 0 \end{pmatrix} \tag{4.9}$$

Taking advantage of

$$\mathcal{H}(\mathcal{R}_0) = \begin{pmatrix} E_k & 0 \\ 0 & -E_k \end{pmatrix} \tag{4.10}$$

and substituting the expression for the transition density (4.6), and considering (4.8) and (4.9), we may write the QRPA equation in its matrix form

$$\begin{pmatrix} A & B \\ -B^* & -A^* \end{pmatrix} \begin{pmatrix} \mathcal{X}^{(\nu)} \\ \mathcal{Y}^{(\nu)} \end{pmatrix} = \Omega^{(\nu)} \begin{pmatrix} \mathcal{X}^{(\nu)} \\ \mathcal{Y}^{(\nu)} \end{pmatrix} \tag{4.11}$$

where the $\mathcal{X}^{(\nu)}$ refers to the forward amplitude transition density corresponding to $-i\Omega_\nu t$, and $\mathcal{Y}^{(\nu)}$ to the backward amplitude $i\Omega_\nu t$, and are defined as

$$\begin{aligned} \mathcal{X}_{kk'}^{(\nu)} &= \langle 0|\alpha_k \alpha_{k'}|\nu\rangle \\ \mathcal{Y}_{kk'}^{(\nu)} &= \langle 0|\alpha_{k'}^\dagger \alpha_k^\dagger|\nu\rangle \end{aligned} \tag{4.12}$$

The forward amplitude is thus associated with the creation of two quasiparticles, and the backwards amplitude is then associated with the destruction of a pair of quasiparticles. For two different RPA excited states ν and ν', the following orthogonality relation holds

$$\sum_{kk'} \mathcal{X}_{kk'}^{(\nu)*} \mathcal{X}_{kk'}^{(\nu')} - \mathcal{Y}_{kk'}^{(\nu)*} \mathcal{Y}_{kk'}^{(\nu')} = \delta_{\nu\nu'} \tag{4.13}$$

and that can be used to normalize the vector $(\mathcal{X}^{(\nu)}, \mathcal{Y}^{(\nu)})$. The transition probabilities between the excited state $|\nu\rangle$ and the ground state $|0\rangle$, for a one body operator $\hat{\mathcal{O}}$ within the RPA approximation, are thus given by

$$\langle 0|\hat{\mathcal{O}}|\nu\rangle = \mathrm{Tr}\left(\mathcal{O}\mathcal{X}^{(\nu)} + \mathcal{O}^* \mathcal{Y}^{(\nu)}\right) \tag{4.14}$$

In a finite quasiparticle configuration space, and for $k < k'$ and $l < l'$, the QRPA matrices A and B read

$$\begin{aligned} A_{kk',ll'} &= (E_k + E_{k'})\delta_{kk}\delta_{k'l'} + \hat{v}_{kk'll'} \\ B_{kk',ll'} &= \hat{v}_{kk'l'l} \end{aligned} \tag{4.15}$$

where

$$\hat{v}_{kl'k'l} = \frac{\delta^2 E}{\delta\mathcal{R}^{\star}_{kk'}\delta\mathcal{R}_{ll'}} \tag{4.16}$$

is the so-called *residual interaction.* The evaluation of these matrices is greatly simplified in the canonical basis, where the quasiparticle transformation reduces to the BCS case. When time-reversal invariance holds,each single particle state has a corresponding conjugate (denoted by the bar), and the matrix elements may be written as

$$\begin{aligned} A_{kk',ll'} = (E_k + E_{k'})\delta_{kl}\delta_{k'l'} &+ \frac{1}{2}V^{pp}_{kl'k'l}(\xi^{+}_{kk'}\xi^{+}_{ll'} + \xi^{-}_{kk'}\xi^{-}_{ll'}) \\ &+ \frac{1}{2}V^{ph}_{k\bar{l}'\bar{k}'l}(\eta^{+}_{kk'}\eta^{+}_{ll'} + \eta^{-}_{kk'}\eta^{-}_{ll'}) \\ &- \frac{1}{2}V^{ph}_{k\bar{l}\bar{k}'l'}(\eta^{+}_{kk'}\eta^{+}_{ll'} - \eta^{-}_{kk'}\eta^{-}_{ll'}) \end{aligned} \tag{4.17}$$

and

$$\begin{aligned} B_{kk',ll'} &= \frac{1}{2}V^{pp}_{kinj}(\xi^{+}_{kk'}\xi^{+}_{ll'} + \xi^{-}_{kk'}\xi^{-}_{ll'}) \\ &+ \frac{1}{2}V^{ph}_{kl\bar{k}'\bar{l}'}(\eta^{+}_{kk'}\eta^{+}_{ll'} + \eta^{-}_{kk'}\eta^{-}_{ll'}) \\ &- \frac{1}{2}V^{ph}_{kl'\bar{k}'\bar{l}}(\eta^{+}_{kk'}\eta^{+}_{ll'} - \eta^{-}_{kk'}\eta^{-}_{ll'}) \end{aligned} \tag{4.18}$$

where

$$\begin{aligned} \xi^{\pm}_{kk'} &= u_k v_{k'} \pm v_k u_{k'} \\ \eta^{\pm}_{kk'} &= u_k u_{k'} \mp v_k v_{k'} \end{aligned} \tag{4.19}$$

are the single particle occupation factors. The ph matrix elements $V^{ph}_{kl'k'l}$ are the second derivatives of the energy functional with respect the single particle density

$$V^{ph}_{kl'k'l} = \langle kk'|\frac{\delta^2 E}{\delta\hat{\rho}_{kk'}\delta\hat{\rho}_{l'l}}|ll'\rangle \tag{4.20}$$

and similarly, the pp matrix elements $\bar{V}^{pp}_{minj}$ are given by the second derivative of the energy functional, but this time with respect to the abnormal density $\hat{\kappa}$

$$V^{pp}_{kl'k'l} = \langle kk'|\frac{\delta^2 E}{\delta\hat{\kappa}_{kl}\delta\hat{\kappa}_{k'l'}}|ll'\rangle \tag{4.21}$$

Finally, the transition matrix elements for a one-body external operator $\hat{\mathcal{O}}$ in the canonical basis reads

$$\langle 0|\hat{\mathcal{O}}|\nu\rangle = \sum_{kk'} \left(\mathcal{O}_{k'k} \mathcal{X}^{(\nu)}_{kk'} + \mathcal{O}^{*}_{kk'} \mathcal{Y}^{(\nu)}_{kk'} \right) (u_k v_{k'} + \tau v_k u_{k'}) \tag{4.22}$$

where $\tau = \pm 1$ depending on the time reversal properties of the operator $\hat{\mathcal{O}}$: $\tau = 1$ if it is positive under time reversal, and $\tau = -1$ otherwise. In the case of vanishing pairing correlations, one recovers the RPA theory where

$$A_{kk',ll'} = (\varepsilon_k - \varepsilon_{k'})\delta_{kl}\delta_{k'l'} + V^{ph}_{kl'k'l} \tag{4.23}$$

and

$$B_{kk',ll'} = V^{ph}_{klk'l'} \tag{4.24}$$

and with the transition matrix elements

$$\langle 0|\hat{\mathcal{O}}|\nu\rangle = \sum_{mi} \left(\mathcal{O}_{im} \mathcal{X}^{(\nu)}_{mi} + \mathcal{O}^{*}_{mi} \mathcal{Y}^{(\nu)}_{mi} \right) \tag{4.25}$$

4.2 The residual interaction

As seen in the previous chapter, the RHB ground state solutions are characterized by the generalized density $\mathcal{R}$, and in the case of meson exchange functionals also by the meson fields ϕ, which are treated as independent variables connected by the equations of motion. In order to describe small oscillations self-consistently the meson degrees of freedom have to be eliminated from the energy functional so the set of equations (4.20) and (4.21) are closed, i.e., the residual interaction has to be expressed as a functional of the generalized density $\mathcal{R}$ only. In the case of point coupling functionals this step is, evidently, non-existent as there are no explicit mesons, and the residual interaction can be immediately derived using (4.20). On the other hand, the elimination of the meson fields is possible only in the limit of small amplitudes. In this case, and restricting the discussion for now to the Walecka model, we can expand the density and fields around their stationary values

$$\begin{aligned} \phi &= \phi^{(0)} + \delta\phi \\ \mathcal{R} &= \mathcal{R}^{(0)} + \delta\mathcal{R} \end{aligned} \tag{4.26}$$

where $\delta\mathcal{R}$ and $\delta\phi$ are small deviations from the ground state values $\mathcal{R}^{(0)}$ and $\phi^{(0)}$. Substituting this expansion in the Klein-Gordon equations (3.15) and retaining only first order in $\delta\rho$

$$\left[\partial_\mu \partial^\mu + m_m^2)\right] \delta\phi_m = \pm g_m \delta\rho_m \tag{4.27}$$

Neglecting retardations effects (i.e. neglecting ∂_t^2) we find for the linearized equations of motion for the mesons

$$\left[-\nabla + m_m^2)\right] \delta\phi_m = \pm g_m \delta\rho_m \tag{4.28}$$

This approximation is meaningful at low energies, where the large meson masses assure us that the corresponding meson exchange forces are of short range and therefore retardation effects can be neglected. A formal solution for (4.28) can be written as

$$\delta\phi_m = \pm \int d^3r' g_m G_m(\boldsymbol{r}, \boldsymbol{r}')\delta\rho_m \tag{4.29}$$

which allows us to express the residual interaction $\hat{v}^{ph}$ in the general form

$$\hat{v}^{ph}_{mnij} = \frac{\delta^2 E}{\delta\hat{\rho}_{mi}\delta\hat{\rho}_{jn}} = \sum_{m=\sigma,\omega,\rho,\gamma} \Gamma'_m G_m(\boldsymbol{r}, \boldsymbol{r}')\Gamma_m \tag{4.30}$$

where the m refers to a specific meson field (summation implied), the propagator $G(\mathbf{r}, \mathbf{r}')$ is in principle the same for each type of meson field except for the mass, and the Γ_m reflect the different covariant structures of the fields as defined in (3.8). For example, for the Walecka model we can write the residual interaction as a sum over the contributions coming from the different meson fields and the electromagnetic interaction

$$\hat{v}^{ph} = \hat{v}_\sigma + \hat{v}_\omega + \hat{v}_\rho + \hat{v}_\gamma \tag{4.31}$$

where each one of the terms may be written as

$$\hat{v}^{ph}(1,2) = -g\gamma^{(1)} G(\mathbf{r}_1, \mathbf{r}_2)\gamma^{(2)} \tag{4.32}$$

In particular, they read

- σ meson field
$$\hat{v}^{ph}_\sigma(\mathbf{r}, \mathbf{r}') = -g_\sigma^2 G_\sigma(\mathbf{r}, \mathbf{r}') \tag{4.33}$$

- ω meson field
$$\hat{v}^{ph}_\omega(\mathbf{r}, \mathbf{r}') = g_\omega^2 \gamma^\mu G_\omega(\mathbf{r}, \mathbf{r}')\gamma'_\mu \tag{4.34}$$

- ρ meson field
$$\hat{v}^{ph}_\rho(\mathbf{r}, \mathbf{r}') = g_\rho^2 \gamma^\mu \vec{\tau} G_\rho(\mathbf{r}, \mathbf{r}')\gamma'_\mu \vec{\tau}' \tag{4.35}$$

- photon field
$$\hat{v}^{ph}_\gamma(\mathbf{r}, \mathbf{r}') = \frac{e^2}{4}\gamma^\mu(1-\tau_3) G_\gamma(\mathbf{r}, \mathbf{r}')\gamma'_\mu(1-\tau'_3) \tag{4.36}$$

where G_m are the meson propagators, solution of

$$(-\Delta + m_m^2)G_m = \delta(\mathbf{r} - \mathbf{r}') \tag{4.37}$$

which in this simple model adopt a Yukawa form

$$G_m(\mathbf{r}, \mathbf{r}') = \frac{e^{-m_m|\mathbf{r}-\mathbf{r}'|}}{4\pi|\mathbf{r} - \mathbf{r}'|} \tag{4.38}$$

where, in the case of the photon, clearly, the mass is zero.

For the non-linear σ density functional, the Klein-Gordon equation for the σ field cannot be solved analytically, and one has to resort to numerical techniques. A general overview of the procedure involved, and the particularization to axial symmetry, can be found in Appendix A.

In the case of meson exchange energy functionals with density dependent couplings, the residual two-body interaction carries a number of rearrangement terms, due precisely to the meson-nucleon coupling density dependence. These rearrangement terms are essential for a fully self consistent RQRPA implementation. Only when their contributions are included in the matrix elements of the residual interaction it is possible to reproduce reasonably well the excitation energy of giant multipole resonances. Without rearrangement terms one finds discrepancies of several MeV between the experimental excitation energies and the RQRPA peak energies, when calculated with relativistic effective interactions adjusted to ground state properties of spherical nuclei. A very similar effect is observed in RQRPA calculations based on effective interactions with non linear meson interactions when the contribution of the non linear terms is not included in the matrix elements of the residual interaction [99]. All the corresponding formulas for the residual two-body interaction for these energy functionals can be found in the Appendix A.

Finally, the procedure for the derivation of the residual interaction in the case of point coupling models follows closely that of the Walecka model. Expanding the densities around their ground state value, and keeping only the first order, the residual interaction matrix elements can be easily derived. For the details and formulas please refer to the Appendix A.

Chapter 5

RMF+RPA in Axial symmetry

“The idea is to try to give all the information to help others to judge the value of your contribution; not just the information that leads to judgment in one particular direction or another.”
— Richard P. Feynman, 1918-1988

The phenomenon of nuclear deformation has a long and interesting history. As early as 1924 it was suggested by Pauli [112] that the hyperfine structure of atomic and molecular energy levels resulted from the electromagnetic interaction with non-spherical atomic nuclei. The experimental evidence was given ten years later by Schüler and Schmidt [138]. The fact that nuclei need not be spherical was then emphasized by Niels Bohr in his classic paper on the nuclear liquid-drop model [28] in which he introduced the concept of nuclear shape vibrations. If a quantum-mechanical system is deformed, its spatial density is anisotropic, so it is possible to define its orientation as a whole, and this naturally leads to the presence of collective rotational modes.

In 1950, Rainwater [119] observed that the experimentally measured large quadrupole moments of nuclei could be explained in terms of the deformed shell model i.e., the extension of the spherical shell model to the case of the deformed average potential. In this picture, the deformed field was a direct consequence of single-particle motion in anisotropic orbits. In a following paper [26], Age Bohr formulated the basis of the particle-rotor model, and introduced the concept of the intrinsic (body-fixed) nuclear system defined by means of shape deformations, and regarded nuclear shape and orientation as dynamical variables. The basic microscopic mechanism leading to the existence of nuclear deformations was proposed by A. Bohr [27], stating that the strong coupling of nuclear surface oscillations to the motion of individual nucleons is the reason to the observed static deformations in nuclei.

The idea was not new, and in fact it was proposed a decade earlier by Jahn and Teller [72] in the context of molecular collective motion. As early as 1927 Born and Oppenheimer [29] successfully described molecular motion by assuming that the fast electrons were strongly coupled to the equilibrium position of the comparatively slow and much heavier atoms. However, this picture breaks down when the electronic subsystem has degenerate energy states. Jahn and Teller proved that in such cases the configuration of atoms can develop a stable symmetry-breaking configuration, provided the coupling between degenerate electronic excitations and collective motion is sufficiently strong. This phenomenon is usually referred to as spontaneous symmetry breaking or the Jahn-Teller effect [48]. Thus, in such a symmetry-breaking system it is possible to define an intrinsic deformed frame of reference, determined by the instantaneous position of the slow degrees of freedom. The mean-field solutions referring to the intrinsic system are then characterized by self-consistent symmetries. The ground-state is no longer a unique absolute minimum on the energy surface, rather there exist a continuous set of degenerate ground-states with different orientations. In the molecular case the orientation, i.e. the collective degrees of freedom, are well defined by the positions of the atoms.

However, in contrast to the molecular case, it is not clear a priori what the slow degrees of freedom are in the nuclear system: the choice of proper nuclear collective coordinates is a long-standing problem (see for example Ref. [133]). Nowadays, the deformation mechanism in nuclei is well understood [133]; for sufficiently high level density in the vicinity of the Fermi surface, or for sufficiently strong residual interaction, the first 2^+ excited state (a quadrupole surface phonon) comes down to zero energy (it "freezes out"), effectively creating a condensate of quadrupole phonons that give rise to a static deformation of the mean-field ground state.

In order to calculate excitations in these deformed nuclei the RPA theory outlined in the previous section can be used. One has to remember, however, that these excitations are intrinsic in as much as they are relative to the local deformed ground-state, and do not have good angular momentum. Nevertheless, the application of the RPA to the intrinsic excitations of deformed nuclei is formally completely analogous to that for spherical nuclei. The only difference comes from the fact that the configuration space used is composed of single particle orbitals *without* good angular momentum. For this reason it is not possible to use the angular momentum coupled representation to reduce the dimensions of the RPA matrix. However, in the case of axial symmetry reductions are possible which comply with the constraints imposed by the projection of the angular momentum projection on the symmetry axis.

A direct consequence of the artificial separation between intrinsic and rotational excited states (the later referred to the collective degrees of freedom) is that one has to be careful comparing the results of calculations with experiment; allowance must be made for the rotational motion in relating intrinsic excitation energies and matrix elements to the observable quantities. Of particular importance are experimental observables, such as transition densities, BEL-values or multipole moments, which refer to the laboratory system frame of reference, and thus cannot be calculated simply in the intrinsic system using deformed wave functions. One has first to transform these wave functions to the laboratory frame by angular momentum projection, i.e. only matrix elements calculated with projected wavefunctions can be compared with experimental results.

5.1 Density Functional Theory in deformed nuclei

Let us suppose that there exist a symmetry operator $\mathcal{O}$ such that the energy density functional is invariant under the symmetry transformations $e^{i\alpha\mathcal{O}}$, i.e. for a transformed density $\tilde{\rho}$

$$\tilde{\rho} = e^{-i\alpha\mathcal{O}}\,\rho\,e^{i\alpha\mathcal{O}} \tag{5.1}$$

we have

$$E[\tilde{\rho}] = E\left[e^{-i\alpha\mathcal{O}}\,\rho\,e^{i\alpha\mathcal{O}}\right] = E[\rho] \tag{5.2}$$

Examples of such a symmetry in even-even nuclear systems would be rotational and translational symmetries and the third component of isospin (i.e. the charge). If the density has the same symmetry, i.e. $\tilde{\rho} = \rho$, we can restrict the set of variational densities to those with this symmetry. However, such a symmetric solution is not necessarily at the minimum in the energy surface defined by $E[\rho]$, that is, the best solution. Because of the non-linearity of the variational equation (3.24) it is possible spontaneous symmetry breaking solutions, i.e., the energy density is invariant under $\mathcal{O}$-transformations but the density is not $\tilde{\rho} \neq \rho$.

Rotations are one of such continuous symmetry transformations. Nuclei with one closed shell are special in the sense that one can always write their ground state wavefunction as a rotationally invariant Slater determinant. On the other hand, most nuclei throughout the periodic table have both open shells, and thus their respective determinantal single particle densities *cannot* be invariant under rotations. However, since each single-particle orbital is separately invariant under rotations about the z-axis, it follows that all nuclei have an axially symmetric variational solution of (3.24). But, even though such a solution exists, it does not necessarily have to be the lowest in energy. So, as was remarked in the introduction, the existence of a deformed wavefunction which minimises the energy is the direct consequence of the variational procedure, in particular the requirement for it to be a Slater determinant of single particle orbitals. Conversely, although it is always possible to find a solution to the variational problem with good angular momentum, in general neither the single particle orbitals nor the many particle determinant need to preserve rotational symmetry, and it does not follow that the spherical solution is the best, and frequently it is not.

The present investigation is restricted to nuclei that can be adequately described by an axially symmetric variational wave function, and so the projection of the angular momentum on the symmetry axis is a conserved quantity. It is therefore convenient to use cylindrical coordinates $(r_\perp,\, \theta,\, z)$, were, as usual, the symmetry axis is labeled as the z-axis. The single-particle Dirac spinors, solution of (3.27), are then characterized by the angular momentum projection Ω, the parity π and the isospin projection t. Their general form is

$$\varphi_i(\mathbf{r}) = \frac{1}{\sqrt{2\pi}} \begin{pmatrix} f_i^+(r_\perp, z)e^{i(\Omega_i-1/2)\phi} \\ f_i^-(r_\perp, z)e^{i(\Omega_i+1/2)\phi} \\ ig_i^+(r_\perp, z)e^{i(\Omega_i-1/2)\phi} \\ ig_i^-(r_\perp, z)e^{i(\Omega_i+1/2)\phi} \end{pmatrix} \chi_{t_i(t)} \tag{5.3}$$

For even-even nuclei, for each solution ψ_i with positive Ω_i there exists a time-reversed one with the same energy, denoted by a bar, $\bar{i} := \{\epsilon_i,\, -\Omega_i,\, \pi_i\}$. The time reversal operator takes the usual form $i\sigma_y\hat{K}$, where $\hat{K}$ is the complex conjugation.

$$i\sigma_y\hat{K}\varphi_i = \frac{1}{\sqrt{2\pi}} \begin{pmatrix} f_i^-(r, z)e^{i(-\Omega_i+1/2)\phi} \\ -f_i^+(r, z)e^{i(-\Omega_i-1/2)\phi} \\ -ig_i^-(r, z)e^{i(-\Omega_i+1/2)\phi} \\ ig_i^+(r, z)e^{i(-\Omega_i-1/2)\phi} \end{pmatrix} \chi_{t_i(t)} \tag{5.4}$$

It is clear from (5.3, 5.4) and (3.26, 3.25) that the densities and meson fields do not depend on the azimuthal coordinate ϕ, and are thus axially symmetric

$$\rho := \rho(r_\perp, z) \qquad \phi := \phi(r_\perp, z) \tag{5.5}$$

5.2 Configuration space for the RPA and QRPA equations

Because the angular momentum projection operator J_z and the parity operator Π commute with the effective Dirac Hamiltonian (3.16)

$$\begin{aligned} \left[\hat{h}, J_z\right] &= 0 \\ \left[\hat{h}, \Pi\right] &= 0 \end{aligned} \tag{5.6}$$

that is, they leave the configuration space basis set $\{\varphi_i\}$ invariant

$$\begin{aligned} J_z\{\varphi_i\} &= \{\varphi_i\} \\ \Pi\{\varphi_i\} &= \{\varphi_i\} \end{aligned} \tag{5.7}$$

and they also commute with the residual interaction (4.16)

$$\begin{aligned} [\hat{v}, J_z] &= 0 \\ [\hat{v}, \Pi] &= 0 \end{aligned} \tag{5.8}$$

it follows that the total angular momentum projection and parity are conserved both in the ground-state and at the RPA level. Or more explicitly, in order for the matrix elements (4.16) of the residual interaction to be non-zero, the following two selection rules must hold

$$\begin{aligned} \Omega_m + \Omega_i &= \Omega_n + \Omega_j \\ \pi_m \pi_i &= \pi_n \pi_j \end{aligned} \tag{5.9}$$

We can thus define particle-hole excitations with good angular momentum projection K that automatically satisfy (5.9) as

$$Q^+_{\nu,K} = \sum_{mi} \mathcal{X}^{(\nu,K)}_{mi} a^\dagger_m a_{\bar{i}} - \sum_{mi} \mathcal{Y}^{(\nu,K)}_{mi} a^\dagger_i a_{\bar{m}} \tag{5.10}$$

and similarly for quasi-particle excitations

$$Q^+_{\nu,K} = \sum_{kk'} \mathcal{X}^{(\nu,K)}_{kk'} \alpha^\dagger_k \alpha^\dagger_{k'} - \sum_{kk'} \mathcal{Y}^{(\nu,K)}_{kk'} \alpha_{\bar{k}} \alpha_{\bar{k}'} \tag{5.11}$$

where the bar indicates the conjugate state such that $\Omega_i = -\Omega_{\bar{i}}$ and $K = \Omega_m + \Omega_i$ is the excited state total angular momentum projection. With these definitions for the coupled excited states it is easily shown that the RPA equation (4.11) is block-diagonal in parity and in angular momentum projection. So it makes perfect sense to label the different excitation modes as

$$K^{\pi} = 0^{\pm}, 1^{\pm}, 2^{\pm}, \cdots \tag{5.12}$$

where

$$K^{\pi} = (\Omega_m + \Omega_i)^{(\pi_m \pi_i)} \tag{5.13}$$

For even-even nuclei, as we have seen before, one can define the conjugation operation as time reversal, and thus for each level $i := \{\epsilon_i,\, \Omega_i,\, \pi_i\}$ there exists a degenerate time reversed one $\bar{i} := \{\epsilon_i,\, -\Omega_i,\, \pi_i\}$. One has to be careful handling time reversal symmetry in the case of coupling to $K = 0$, where for each pair of the form (5.13) there exists the time reversed one

$$K^{\pi} = (\Omega_{\bar{m}} + \Omega_{\bar{i}})^{(\pi_m \pi_i)} \tag{5.14}$$

with the same energy that also satisfies (5.9), and has to be considered explicitly when calculating the matrix elements. In particular, and depending on the Dirac basis chosen, in this case ($K = 0$), some of the Dirac spatial components of the matrix elements vanish identically.

5.3 Evaluation of the residual interaction matrix elements

As we have seen in Section 4.2, the residual interaction can be derived from the energy functional as its second functional derivative

$$\hat{v}^{ph}_{mnij} = \frac{\delta^2 E}{\delta \hat{\rho}_{mi} \delta \hat{\rho}_{jn}} = \sum_{m=\sigma,\omega,\rho,\gamma} \Gamma_m G_m(\boldsymbol{r}, \boldsymbol{r}')\Gamma'_m \tag{5.15}$$

In the case of the non-linear and density dependent energy functionals, the propagator takes a Yukawa form, and the integral to be calculated is four dimensional in the axial symmetry case. For a linear interaction, however, the propagator in momentum space is diagonal, i.e. $\Delta(\mathbf{k}, \mathbf{k}') \equiv \Delta(\mathbf{k})$, so in principle it should be possible to express the interaction in momentum space and take advantage in the implementation of this reduction in dimensions (from four to two) for the calculation of the integrals. Taking the Fourier transform of the residual interaction we obtain

$$V^{ph}_{minj} = \sum_{m=\sigma,\omega,\rho,\gamma} \int \frac{d^3k}{(2\pi)^3} Q^{\mu}_{mi}(\mathbf{k}) \Delta_m(\mathbf{k}) Q_{nj,\mu}(-\mathbf{k}) \tag{5.16}$$

with the propagator

$$\Delta_m(\mathbf{k}) = \frac{1}{\mathbf{k}^2 + m^2} \tag{5.17}$$

and the single-particle matrix elements

$$Q^{\mu}_{mi}(\mathbf{k}) = \int d^3r \bar{\varphi}_m(\mathbf{r})\Gamma^{\mu}(\mathbf{r})\varphi_i(\mathbf{r})e^{-i\mathbf{kr}} \tag{5.18}$$

where $\Gamma(\mathbf{r}) \equiv \Gamma$ is independent of the coordinate $\mathbf{r}$ in the case of linear interactions in the non-linear density functionals, and depends on it via the coupling constant g in the case of density dependent interactions.

However, for the point coupling models the propagator in coordinate space G is in fact a function of the δ distribution, and finally only a two dimensional integration is needed for the actual calculation of its matrix elements. It is very clear then that there is no advantage in going to a Fourier space, so the actual implementation for point coupling models is in fact in coordinate space. The general procedure for the calculation of matrix elements for linear density functionals is outlined in the next section. The required extensions and particular cases, arising from the non-linearities in the case of Non Linear Meson Exchange density functionals, and from the explicit density dependence in Density Dependent Meson Exchange and Density Dependent Point Coupling functionals, are given in Appendix A.

5.3.1 Matrix elements for linear density functionals

The starting point in the actual evaluation of the residual interaction matrix elements for linear functionals is Equation (5.16). In the case of axial symmetry, the computation of the required single particle matrix elements (5.18) is best accomplished in cylindrical coordinates. The momentum coordinates involved would be then $\mathbf{k} = (k_x, k_y, k_z) = (k_{\perp}\cos\chi, k_{\perp}\sin\chi, k_z)$, and the dot product $i\mathbf{kr}$

$$i\mathbf{kr} = k_{\perp} r \cos(\chi - \phi) + k_z z \tag{5.19}$$

Each single particle matrix element $Q^{\mu}_{mi}(\mathbf{k})$ (5.18) therefore can be written as

$$Q^{\mu}_{mi}(k_{\perp}, \chi, k_z) = \int \frac{d\phi}{2\pi} r dr\, dz\, \overline{\varphi}_m(r,z,\phi)\, \Gamma^{\mu}\, \varphi_i(r,z,\phi)\, e^{ik_z z + ik_{\perp} r\cos(\phi-\chi)} \tag{5.20}$$

Furthermore, it is very easily shown that in the Dirac basis, defined by

$$\{\gamma^0, \gamma^+ = \frac{-1}{\sqrt{2}}(\gamma^1 + i\gamma^2), \gamma^- = \frac{1}{\sqrt{2}}(\gamma^1 - i\gamma^2), \gamma^3\} \tag{5.21}$$

for each μ, the factor $\overline{\varphi}_m(r,z,\phi)\, \Gamma^{\mu}\, \varphi_i(r,z,\phi)$ can be expressed as

$$\overline{\varphi}_m(r,z,\phi)\, \Gamma^{\mu}\, \varphi_i(r,z,\phi) = \frac{1}{2\pi}\alpha^{\mu}_{mi}\, F^{\mu}_{mi}(r,z)\, e^{in^{\mu}_{mi}\phi} \tag{5.22}$$

where n^μ_{mi} is an integer of the form $n^\mu_{mi} = -\Omega_m + \Omega_i \pm \{0, 1\}$, $\alpha^\mu_{mi} = \{\pm 1, \pm i\}$ is a phase and $F^\mu_{mi}(r, z)$ is a real function that does not depend on the azimuthal angle. Dropping the μ and super index for F, α and n, the single particle matrix element (5.18) can be expressed in this particular Dirac basis as

$$Q_{mi}(\mathbf{k}) = \alpha \iiint r dr\, dz\, \frac{d\phi}{2\pi}\, F_{mi}(r, z)\, e^{in\phi}\, e^{ik_z z}\, e^{ik_\perp r\, \cos(\phi-\chi)} \tag{5.23}$$

Carrying the analytical calculations as far as possible (see Appendix A)

$$Q_{mi}(\mathbf{k}) = i^n \alpha\, e^{in\chi} \iint r dr\, dz\, F_{mi}(r, z)\, J_n(k_\perp r)\, e^{ik_z z} \tag{5.24}$$

in which J_n is a Bessel function of the first kind. Naturally, the phase α, the function F and the integer n all depend on the particular μ being considered. Expressions for all cases are given in Appendix A. The case of energy functionals with explicit density dependent meson-nucleon couplings is quite analogous to that of the linear functionals. However, now one has to take into account that the vertex operator Γ depends on the coordinates via the coupling constant. The final expression for the single particle matrix element is thus

$$Q_{mi,m}(\mathbf{k}) = i^n \alpha\, e^{in\chi} \iint r dr\, dz\, F_{mi,m}(r, z)\, J_n(k_\perp r)\, e^{ik_z z} \tag{5.25}$$

5.3.2 Multipole strength and sum rules

Experimental nuclear spectra show excitations as finite width resonances which cannot be described in the lowest order of the RPA, which is only able to specify the position and strength of the transition, not their widths. Higher order correlations, included for example in the phonon coupling model [96] or in two particle two hole RPA [75], are needed in order to be able to describe transition widths. To overcome this problem, we shall adopt the philosophy of averaging the RPA strength distributions for a given multipole operator with a Lorentzian function of the form

$$R(E) = \sum_\nu B^T((E/M)J, K, \omega_\nu) \frac{1}{\pi} \frac{\Gamma/2}{(E - \omega_\nu)^2 + (\Gamma/2)^2} \tag{5.26}$$

resulting in a continuous strength function which can be compared with observations. The reduced transition probabilities B^T are given by the reduced matrix elements

$$\begin{array}{lrcl} \text{electric} & B^T(EJ, K, \omega_\nu) & = & \frac{1}{2} \left| \langle \nu || \hat{Q}_{IK} || 0 \rangle \right|^2 \\ \text{magnetic} & B^T(MJ, K, \omega_\nu) & = & \frac{1}{2} \left| \langle \nu || \hat{M}_{IK} || 0 \rangle \right|^2 \end{array} \tag{5.27}$$

The Lorentzian (5.26) function is defined in such a way that it gives the same EWSR as calculated with the discrete response.

$$S_{EW}(E) = \sum_{\nu} E_{\nu} B^{T}((E/M)J, K, \omega_{\nu}) = \int ER(E)dE \tag{5.28}$$

In the present work the EWSR is evaluated in the interval below 30 MeV excitation energy. The knowledge of the sum rules is of special interest, since it represents a useful test of the models describing the collective excitations [133]. The energy weighted sum (5.28) for a transition operator $\hat{\mathcal{O}}$ can be represented in a double commutator form

$$S_{EW}(E) = \langle \phi | [\hat{\mathcal{O}}, [H, \hat{\mathcal{O}}]] | \phi \rangle \tag{5.29}$$

If only contributions from the kinetic energy term are taken into account,

$$S_{EW}(E) = \frac{\hbar}{2m} \frac{(2\lambda + 1)^2}{4\pi} Z \langle r^{2\lambda - 2} \rangle \tag{5.30}$$

These classical values for the sum rules are only approximate estimates. In practical calculations they may be enlarged by an enhancement factor due to the nucleon-nucleon interaction of the nuclear Hamiltonian. Sum rules also offer the possibility of a consistent definition of the excitation energies of giant resonances, via the energy moments of discrete transition strength distribution

$$m_k = \sum_{\nu} E_{\nu}^{k} B^{T}((E/M)J, K, \omega_{\nu}) \tag{5.31}$$

In the case $k = 1$ this equation defines the energy weighted sum rule (5.28). If the strength distribution of a particular excitation mode has a well pronounced and symmetric resonance shape, its energy is well described by the centroid energy

$$\bar{E} = \frac{m_1}{m_0} \tag{5.32}$$

Alternatively, mean energies are defined as

$$\bar{E}_k = \sqrt{\frac{m_k}{m_{k-2}}} \tag{5.33}$$

where the difference between the values $\bar{E}_1$ and $\bar{E}_3$ can be used as an indication of how much the strength distribution corresponding to and excitation mode is actually fragmented. If the multipole response is characterized by a single dominant peak, the two moments are equal, i.e. $\bar{E}_1 = \bar{E}_3$. In the relativistic approach, due to the *no-sea* approximation, the sum in (5.31) runs not only over the positive excitation energies, but also includes transitions to the empty states in the Dirac sea. They contribute with negative terms to the sum, and as it was pointed out in [116, 144, 102], for the EWSR the double commutator (5.29) vanishes. It means that in RRPA the ordinary particle hole contributions are approximately canceled by the response of the vacuum due to excitations in the Dirac sea

$$\sum_{\nu} E_\nu B^T((E/M)J, K, \omega_\nu) \approx 0 \tag{5.34}$$

5.3.3 Transition strength angular momentum projection

Transition probabilities are the physical quantities that have most sensitivity to the approximations made to the wave functions. For instance, transition probabilities have selection rules that cannot be reproduced unless the wave functions are eigenstates of J^2 and J_z. It is important then in the case of a deformed intrinsic mean field state to project on to good angular momentum. Wave functions $|\Psi_{IM}\rangle$ eigenstates of J^2 and J_z with eigenvalues $I(I+1)$ and M respectively can be built out of a given deformed mean field state $|\Phi\rangle$ by applying the angular momentum projector

$$|\psi_{IM}\rangle = \sum_{K} g^I_K \hat{P}^I_{MK} |\Phi\rangle \tag{5.35}$$

where the angular momentum projector operator $\hat{P}^I_{MK}$ is given by [47]

$$\hat{P}^I_{MK} = \frac{2I+1}{8\pi^2} \int d\Omega \mathcal{D}^{I\star}_{MK}(\Omega)\hat{R}(\Omega) \tag{5.36}$$

where Ω represents the set of Euler angles (α, β,γ), $\mathcal{D}^I_{MK}(\Omega)$ are the well-known Wigner functions [39] and $\hat{R}(\Omega) = e^{-i\alpha \hat{J}_z} e^{-i\beta \hat{J}_y} e^{-i\gamma \hat{J}_z}$ is the rotation operator. Taking into account the transformation law for the multipole operators $\hat{Q}_{\lambda\mu}$ under rotations

$$\hat{R}(\Omega)\hat{Q}_{\lambda\mu}\hat{R}^\dagger(\Omega) = \sum_{\nu} \mathcal{D}^\lambda_{\nu\mu}(\Omega)\hat{Q}_{\lambda\nu} \tag{5.37}$$

The matrix element of a multipole operator between two states with good angular momentum is given by

$$\langle \Psi_{I_f M_f} | \hat{Q}_{\lambda\mu} | \Psi_{I_i M_i} \rangle = \frac{\langle I_i M_i \lambda\mu | I_f M_f \rangle}{\sqrt{2I_f + 1}} \langle I_f || \hat{Q}_\lambda || I_i \rangle \tag{5.38}$$

with the reduced matrix element defined by

$$\begin{aligned}\langle I_f||\hat{Q}_\lambda||I_i\rangle &= \frac{(2I_i+1)(2I_f+1)}{8\pi^2}(-)^{I_i-\lambda}\sum_{K_i,K_f,\nu,\mu'}(-)^{K_f}g^{I_f\star}_{K_f}g^{I_i}_{K_i} \\ &\times\begin{pmatrix} I_i & \lambda & I_f \\ \nu & \mu' & -K_f\end{pmatrix}\int d\Omega\mathcal{D}^{I_i\star}_{\nu K_i}(\Omega)\,\langle\phi_f|\hat{Q}_{\lambda\mu'}\hat{R}(\Omega)|\phi_i\rangle \qquad (5.39)\end{aligned}$$

In the case of axial symmetry, it further reduces to

$$\begin{aligned}\langle I_f||\hat{Q}_\lambda||I_i\rangle &= (2I_i+1)(2I_f+1)(-)^{I_i-\lambda}\frac{1+(-)^{I_i}}{2}\sum_{\mu'}\begin{pmatrix} I_i & \lambda & I_f \\ -\mu' & \mu' & 0\end{pmatrix} \\ &\times\int_0^{\frac{\pi}{2}} d\beta\sin(\beta)d^{I_i\star}_{-\mu'0}(\beta)\,\langle\phi_f|\hat{Q}_{\lambda\mu'}e^{-i\beta\hat{J}_y}|\phi_i\rangle \qquad (5.40)\end{aligned}$$

To evaluate the overlap integrals in the last equation we restrict to the first order in a Kamlah [133] expansion

$$\langle\phi_f|\hat{Q}_{\lambda\mu'}e^{-i\beta\hat{J}_y}|\phi_i\rangle = \langle\phi_f|\hat{Q}_{\lambda\mu'}|\phi_i\rangle\,\langle\phi_f|e^{-i\beta\hat{J}_y}|\phi_f\rangle \qquad (5.41)$$

In the case of very large deformations we obtain the so called needle approximation [159, 171]

$$\langle\phi_f|\hat{Q}_{\lambda\mu'}e^{-i\beta\hat{J}_y}|\phi_i\rangle \simeq \langle\phi_f|\hat{Q}_{\lambda\mu'}|\phi_i\rangle\,\delta_{\mu'0} \qquad (5.42)$$

which gives the final formula used in the E1 and M1 transition strength calculation

$$\langle I_f||\hat{Q}_\lambda||I_i\rangle = (2I_i+1)(2I_f+1)(-)^{I_i-\lambda}\frac{(-)^{I_i+1}-1}{2\sqrt{3}}\,\langle\phi_f|\hat{Q}_{\lambda\mu'}|\phi_i\rangle \qquad (5.43)$$

5.4 Transition densities

Let us now consider the baryon four-current operator in coordinate space

$$\hat{j}^\mu(\mathbf{r}) = \sum_i \gamma^\mu\delta(\mathbf{r}-\mathbf{r}_i) \qquad (5.44)$$

with single-particle matrix elements in the Dirac basis

$$j^\mu_{kk'} = \varphi_k(\mathbf{r})\gamma^\mu\varphi_{k'}(\mathbf{r}) \qquad (5.45)$$

which can be written as

$$\hat{j}^\mu(\mathbf{r}) = \sum_{kk'} j^\mu_{kk'}a^\dagger_k a_{k'} \qquad (5.46)$$

In order to calculate its RPA transition probability for a particular excitation mode ν, we use equation (4.22), which results in

$$\delta j^\mu(\mathbf{r}) = \sum_{mi} (j^\mu_{im} \mathcal{X}^{(\nu)}_{mi} + j^{\mu\,*}_{mi} \mathcal{Y}^{(\nu)}_{mi})(u_m v_i + v_m u_i) \tag{5.47}$$

Thus, the total time dependent baryon four-current for a given excitation mode ν with energy ω_ν is

$$j^\mu(\mathbf{r}, t) = j^\mu_0(\mathbf{r}) + \delta j^\mu(\mathbf{r}) e^{-i\omega_\nu t} + \delta j^\mu(\mathbf{r})^* e^{i\omega_\nu t} \tag{5.48}$$

In particular, the baryon density $\rho(\mathbf{r}, t) = j^0(\mathbf{r}, t)$ can be written as

$$\rho(\mathbf{r}, t) = \rho_0(\mathbf{r}) + \delta\rho(\mathbf{r}) e^{-i\omega_\nu t} + \delta\rho(\mathbf{r})^* e^{i\omega_\nu t} \tag{5.49}$$

Throughout the rest of this document, all instances of intrinsic transition densities refer to the *baryon* intrinsic transition density in coordinate space, $\delta\rho(\mathbf{r})$, as defined by the zero component of equation (5.47), which is not necessarily the density used in the definition of the density functionals. In a fully classical system the baryon transition density would describe the actual movement of particles. However, in a quantum mechanical system they have to be regarded as a measure of the contribution of the different excited states that conform to the evolution of a time-dependent wavepacket composed of all possible excitation modes. How close these transition densities can be interpreted in the classical sense depends on the actual transition strength exhausted by each excitation mode ν. Nevertheless, they provide an intuitive understanding of the nature of the excitation modes, and will be used in qualitative discussions about them.

The particularization of (5.47) to axial symmetry gives, as a result, intrinsic transition densities with the following formal decomposition

$$\delta\rho(\mathbf{r}) = \delta\rho(r_\perp, z) e^{-iK\phi} \tag{5.50}$$

where K is the angular momentum projection of the excitation mode under study. Substituting this last expression in equation (5.49) and taking advantage of the fact that $\delta\rho(r_\perp, z)^* = \delta\rho(r_\perp, z)$ we arrive at

$$\rho(r_\perp, z, \phi, t) = \rho_0(r_\perp, z) + 2\delta\rho(r_\perp, z) \cos(K\phi + \omega_\nu t) \tag{5.51}$$

The two dimensional quantities $\delta\rho(r_\perp, z)$ will be plotted when discussing intrinsic transition densities, and no further reference to the phase expressed by the cosine will be made. In particular, and because the excitation modes have good parity π, only the positive z semiplane will be included. To interpret these plots, it is useful to keep in mind that $\delta\rho(r_\perp, z)$ has to be considered together with equation (5.51) in order to obtain the full three dimensional geometrical picture.

To be able to compare with experimental transition densities measured in the laboratory frame of reference, it is interesting to project the two dimensional intrinsic transition densities $\delta\rho(r_\perp, z)$ on to good angular momentum. In order to do so, we expand the current operator (5.46) using the set of spherical harmonics $\{Y_{\lambda\mu}(\Omega)\}$ as basis

$$\hat{j}^\mu(\mathbf{r}) = \sum_{\lambda\geq K,kk'} j^\mu_{\lambda,kk'}(r) Y_{\lambda K}\, a^\dagger_k a_{k'} \tag{5.52}$$

where

$$j^\mu_{\lambda,kk'}(r) = \int d\Omega\; j^\mu_{kk'}(\mathbf{r}) Y^*_{\lambda K}(\Omega) \tag{5.53}$$

and apply the expression (5.43) to obtain that, for a particular angular momentum $\lambda \geq K$, the projected transition density reads

$$\delta\rho(\mathbf{r}) = \delta\rho_\lambda(r) Y_{\lambda,K}(\Omega) \tag{5.54}$$

with the radial projected transition density

$$\delta_\lambda\rho(r) = \int d\Omega\; \delta\rho(r_\perp, z) Y_{\lambda K}(\Omega) \tag{5.55}$$

Even though this last equation only holds approximately, we will see that the results for well deformed nuclei are excellent. Transition density patterns for, for example, the Giant and Pygmy Dipole Resonances, are in agreement with those found experimentally and in other theoretical RPA studies in spherical symmetry.

5.5 Broken symmetries and spurious (Goldstone) modes

Coming back to the symmetry transformations (5.1), let us consider the case of a broken symmetry, i.e. $\tilde{\rho} \neq \rho$. The property $\rho^2 = \rho$ holds for arbitrary values of α. This means that for ρ being a stationary (i.e. self-consistent) solution the variational equation (3.24), $\tilde{\rho}$ must also be such a solution

$$\left[\hat{h}\left[\tilde{\rho}, \phi\right], \tilde{\rho}\right] = 0. \tag{5.56}$$

Considering only small values of α we obtain, in first order and for a specific $\delta\rho$, for the transformation

$$\tilde{\rho} = \rho + \delta_\alpha\rho = \rho - i\alpha\left[\mathcal{O}, \rho\right] \tag{5.57}$$

with $\delta_\alpha \rho = -i\alpha \left[\mathcal{O}, \rho\right]$, which only has *ph*-matrix elements proportional $\mathcal{O}_{mi}$ and $\mathcal{O}_{im}$

$$\begin{aligned} \delta_\alpha \rho_{mi} &= -i\alpha \mathcal{O}_{mi} \\ \delta_\alpha \rho_{im} &= +i\alpha \mathcal{O}_{im} \end{aligned}$$

the *pp*- and *hh*-matrix elements vanish. Substituting in (5.56), we gain, to first order in α

$$0 = \left[\hat{h}\left[\rho, \phi\right], \delta_\alpha \rho\right] + \left[\frac{\delta \hat{h}\left[\rho, \phi\right]}{\delta \rho} \delta_\alpha \rho, \rho\right] \tag{5.58}$$

which is exactly the RPA equation (4.11) with an excitation energy $\Omega = 0$. It shows that there is a *spurious solution* (*Goldstone mode*) with vanishing energy with the wave functions

$$X_{mi} = \mathcal{O}_{mi} \qquad \text{and} \qquad Y_{mi} = \mathcal{O}_{im} = \mathcal{O}^*_{mi}. \tag{5.59}$$

corresponding to the symmetry transformation generated by $\mathcal{O}$. Of course, in the case where the density is invariant under the symmetry transformation, i.e. $\tilde{\rho} = \rho$, equation (5.56) provides no new information. It is thus apparent that the RPA equation (4.11) has such a solution only for the case of a broken symmetry.

One such broken symmetry is always associated with the center-of-mass motion. This is because any wave function based in any sense on an independent particle picture (barring the case of a slater determinant of plane waves) is inevitably localized in space, and does not, therefore, conserve the total momentum as a good quantum number. The same applies when considering deformed wave functions. For example, an axially deformed mean field ground state defines a characteristic direction in space, namely the symmetry axis, and rotations around it leave the density unchanged. However, any rotation around an axis perpendicular to it produces a different density, even though the energy remains the same (the interaction *is* rotationally invariant), and thus it appears as a spurious excitation at the RPA level. A similar argument can be used to show that another spurious excitation is associated with the particle number violation in the Quasiparticle Random Phase Approximation.

In principle, and for purposes of nuclear spectroscopy, this should not be significant, since it is concerned only with the intrinsic structure of the nucleus. In practice, one should be able to distinguish this spurious excitations from the true excitations of the nucleus, as the physical states tend to be mixed together with spurious response, leading to seriously over estimated strength distributions. It was Thouless (1961) who observed that, to the extent that the RPA is executed exactly, it separates out the spurious excitations exactly and with exactly zero energy. Oddly enough, this very nice property of the RPA is usually not present in higher order approximations. In normal practice, however, because of numerical inaccuracies, truncation of the *ph* configuration space and inconsistencies among the ground state and RPA equations, the spurious states are located at energies somewhat higher than zero. There are several approaches to overcome this problem, usually involving the adjustment with a free parameter of the residual interaction until the spurious modes are properly decoupled or the extraction *a posteriori* of the spurious components from the physical states. In this investigation a fully self-consistent implementation of the RPA is used, and thus as long as numerical inaccuracies are kept to a minimum, the spurious modes should decouple without further complications. In fact, they provide a very accurate test of the actual implementation, and will be used as a tool to check and optimize the numerical parameters of the calculations in the next section.

5.6 Decoupling of spurious modes and spherical symmetry

The spurious modes offer a very precise check on the numerical implementation. Because the block-wise structure of the RPA matrix, they are expected to appear only when specific symmetry constraints are met. The scope of the present investigation is restricted to E1 and M1 excitations, which involves the diagonalization of the RPA matrix for $K^\pi = 0^-, 0^+, 1^-$ and 1^+. The expected appearance of spurious modes can be summarised as

- A rotational spurious mode for $K^\pi = 1^+$, associated with rotations of the nucleus as a whole around a perpendicular of the symmetry axis. Its generator is the angular momentum operator $\hat{\mathbf{J}}$.
- A translational spurious mode for $K^\pi = 0^-, 1^-$, associated with the translation of the nucleus as a whole. Its generator is the linear momentum operator $\hat{\mathbf{P}}$.
- A pairing spurious mode for $K^\pi = 0^+$, which is related with the particle number conservation. Its generator is the number operator $\hat{N}$.

As stated in section 5.5, in theory these spurious modes should decouple at exactly zero energy. However, this is not the case in actual calculations due to several factors. The RQRPA for axial symmetry implementation presented in this work is fully self consistent, i.e., the same interaction is used both in the ground state and in the excitations calculation, so in principle the only factors influencing the position of the spurious modes are of numerical nature.

In fact, the position of the spurious modes is so sensitive to differences in the interaction between the ground state and the RPA, that their sole appearance is a very strong hint

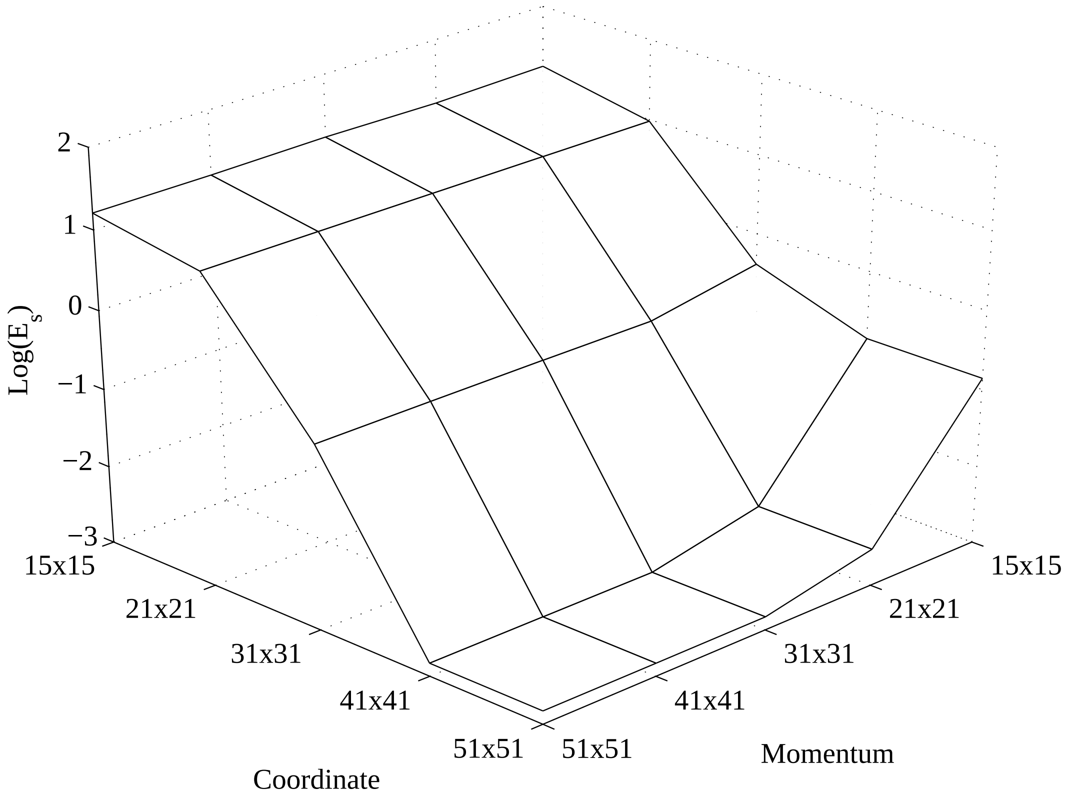

Figure 5.1: Dependence of the $K^\pi = 1^+$ rotational spurious mode on the coordinate and momentum mesh size for the non-linear model NL3 parametrization. For a coordinate and momentum mesh size of (41x41) and (31x31), respectively, the accuracy limit of the diagonalization procedure is achieved. The logarithmic scale in the z-axis is used to enhance the readability of the graph. The lowest z value corresponds to a value of 0.05 MeV.

of the formal correctness of the implementation. Regretfully, the opposite is not true: due to numerical inaccuracies, a correct implementation does not guarantee the proper decoupling of the spurious modes. It is very interesting, thus, to study the dependence of the spurious modes on the numerical parameters which control the precision of the calculations. As an additional benefit, optimal values for these parameters can be found.

There are nine numerical parameters in total that can be categorized in two groups. The first group controls the precision of the numerical integrations. In this category are the number of coordinate and momentum lattice points and the maximum momentum for which the integration takes place. The second group deals with the size of the configuration space, and includes the particle and anti particle energy cutoff, and the particle hole cutoff. Since it is unfeasible to study this nine-dimensional surface

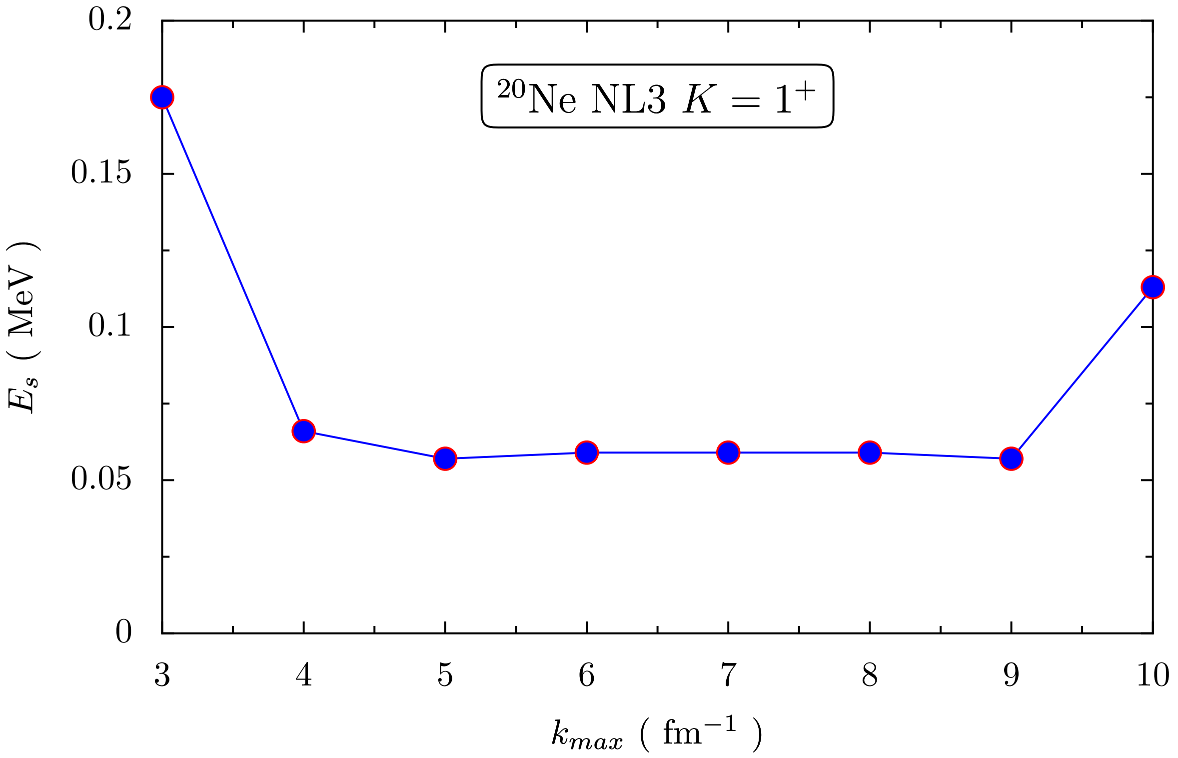

Figure 5.2: Spurious $K^\pi = 1^+$ rotational mode dependence on the maximum interaction momentum while keeping the number of mesh points constant. Good numerical results for a momentum mesh size of (31x31) can be achieved with a maximum momentum in the interval $5 < k_{max} < 9$.

in detail, when studying the dependence of the spurious modes on one, or a set of, parameters, those not under scrutiny were fixed to the maximum precision possible. This means, in particular, that the full *ph* configuration space is taken if not otherwise stated, and that the maximum momentum is fixed to $8\,\mathrm{fm}^{-1}$, well above the Fermi momentum of the nucleus.

In figure 5.1 the position of the rotational spurious mode in ^{20}Ne is plotted against the number of points in the coordinate and momentum lattices. For a relatively low number of points a plateau is reached where further improvement of the accuracy cannot be achieved. The optimal number of evaluation points for the integrations is therefore around 41x41, which allows for very precise calculations. Furthermore, additional tests show that the overall precision in the determination of the energy of excited states of the code is capped out at 0.01 MeV, which is surprisingly good. In general, it was observed that, if the position of the spurious mode is below 1 MeV, the strength function of the rest of the spectrum is mostly unaffected. The spectrum in the low energy region, below 5 MeV, is, however, more sensitive to admixtures coming from the spurious modes; as a rule of thumb, the confidence limit in the position of the spurious mode, for a proper decoupling, has been consistently found around 0.5 MeV.

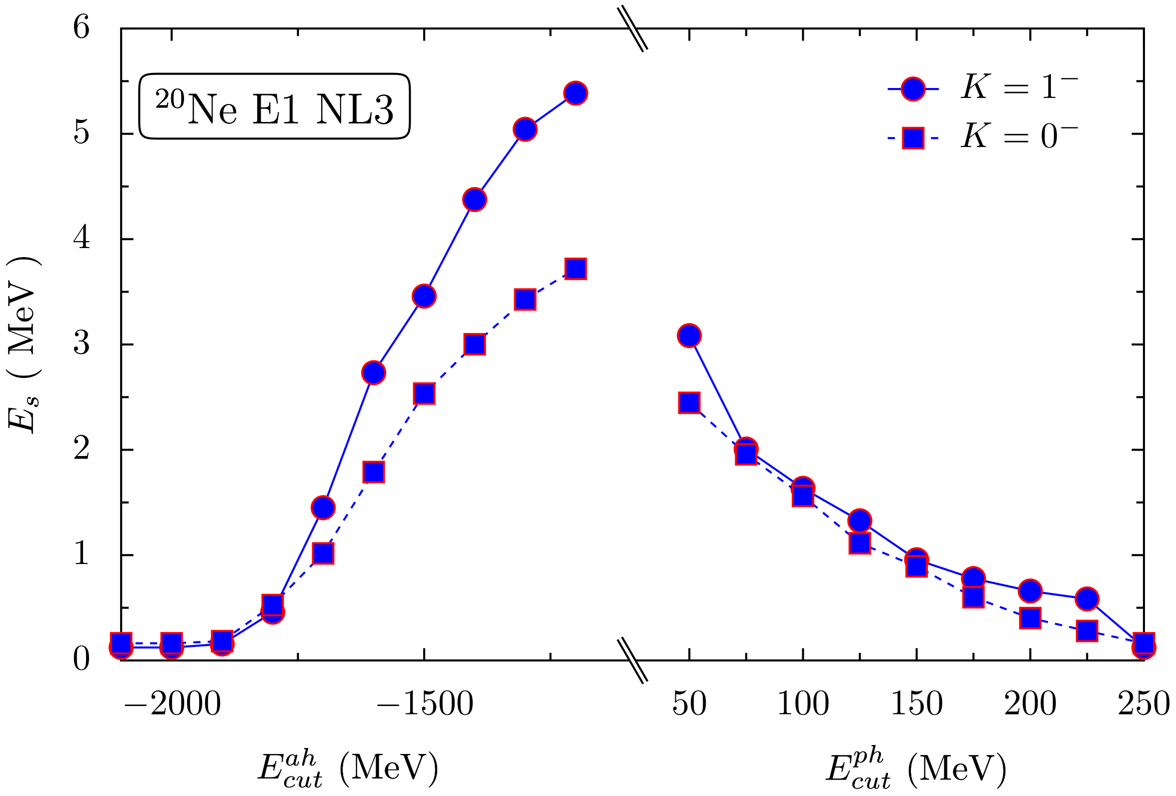

Figure 5.3: Translational spurious mode dependence on the configuration space size.

Figure 5.2 depicts the position of the rotational spurious mode for ^{20}Ne against the maximum momentum of the expansion used for the calculation of the single particle matrix elements. The flat region between 5 and 9 fm^{-1} hints that a maximum momentum of 5 fm^{-1} provides enough precision for the proper spurious mode decoupling. The increase in the position of the spurious mode for momentum values larger than 9 fm^{-1} is an artifact due to the number of points for the momentum lattice being fixed at 31x31, while the maximum momentum is increased. Figures 5.1 and 5.2 show that convergence to a stable solution is achieved with a relatively low number of points for the coordinate and momentum integration meshes. This is important because, for a 2-dimensional problem such the one we want to solve numerically, the total number of points of the numerical integration lattices, and therefore program running time, increases quadratically with the number of points in each direction.

Figures 5.3 and 5.4 show the dependence of the translational and rotational spurious modes, respectively, on the configuration space size for ^{20}Ne calculated with the NL3 parameter set. In the translational case of two curves are plotted, one for the $K^\pi = 0^-$ mode and one for the $K^\pi = 1^-$ mode. It is interesting to note that, even if the spurious mode can be brought very close to zero, it requires the inclusion of almost all the possible *qp*-pairs in the configuration space. In this specific case, ^{20}Ne, that amounts

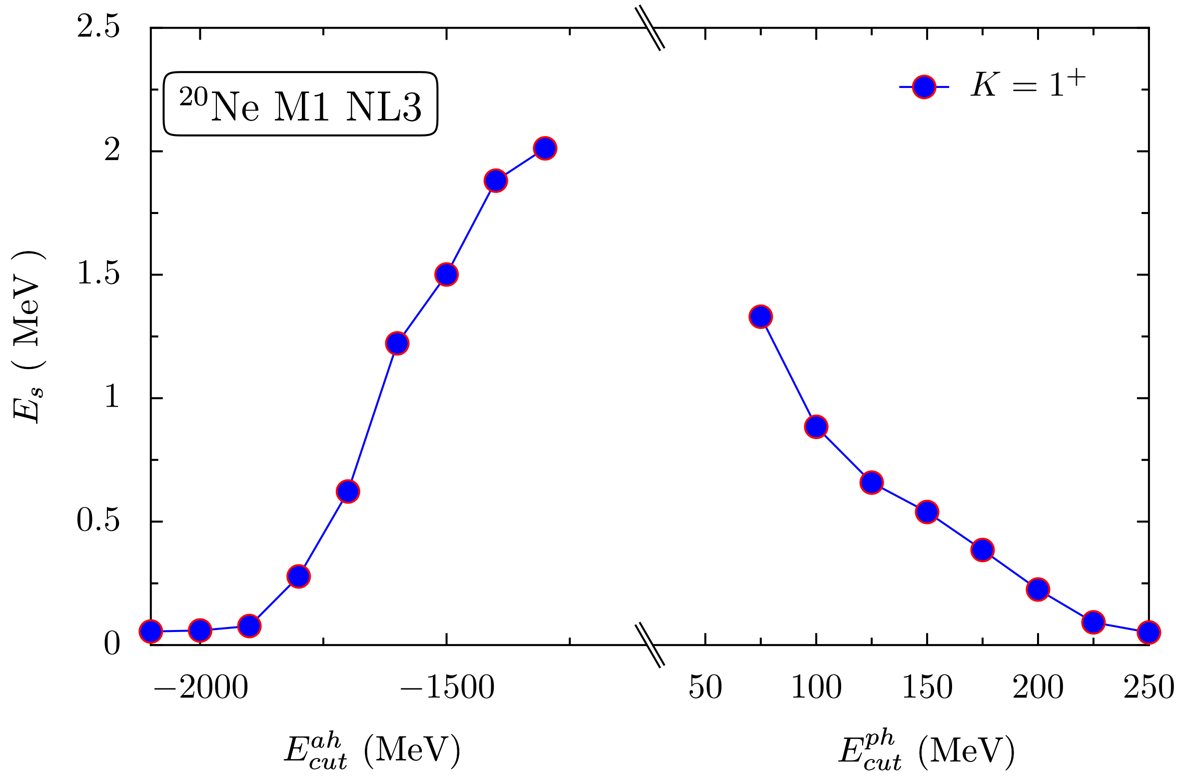

Figure 5.4: Rotational spurious mode dependence on the configuration space size.

to roughly five thousand pairs. The situation improves greatly in heavier nuclei, where usually 5% percent of all possible *qp*-pairs are enough to decouple the spurious modes at energies around 0.5 MeV. To give an idea of the problem-size involved in real-world practical calculations, for the calculation of the response of ^{156}Gd to the M1 operator (see Chapter 6), 15 thousand *qp*-pairs were enough for the decoupling of the spurious mode at an energy of 0.15 MeV. And, for the study of the Giant Dipole Resonance and Pygmy Dipole Resonance in ^{100}Mo (see Chapter 7), a calculation with around 14 thousand pairs brings down the translational spurious mode to energies very close to 0.3 MeV.

Since for the static calculation the ground-state wavefunctions are expanded in an harmonic oscillator basis, the configuration space where the RPA is solved does not spawn the whole Hilbert space. How good is this expansion depends on the number of major oscillator shells used. All results and calculations will be influenced by this approximation. In particular, the proper decoupling of the translational spurious mode is very sensitive. In Figure 5.5 the translational spurious mode is plotted versus the number of oscillator shells used in the ground state calculation for the DDME energy functional. Already with only 12 harmonic oscillator shells is enough to achieve a precision in the spurious mode of around 0.1 MeV. In all practical cases presented

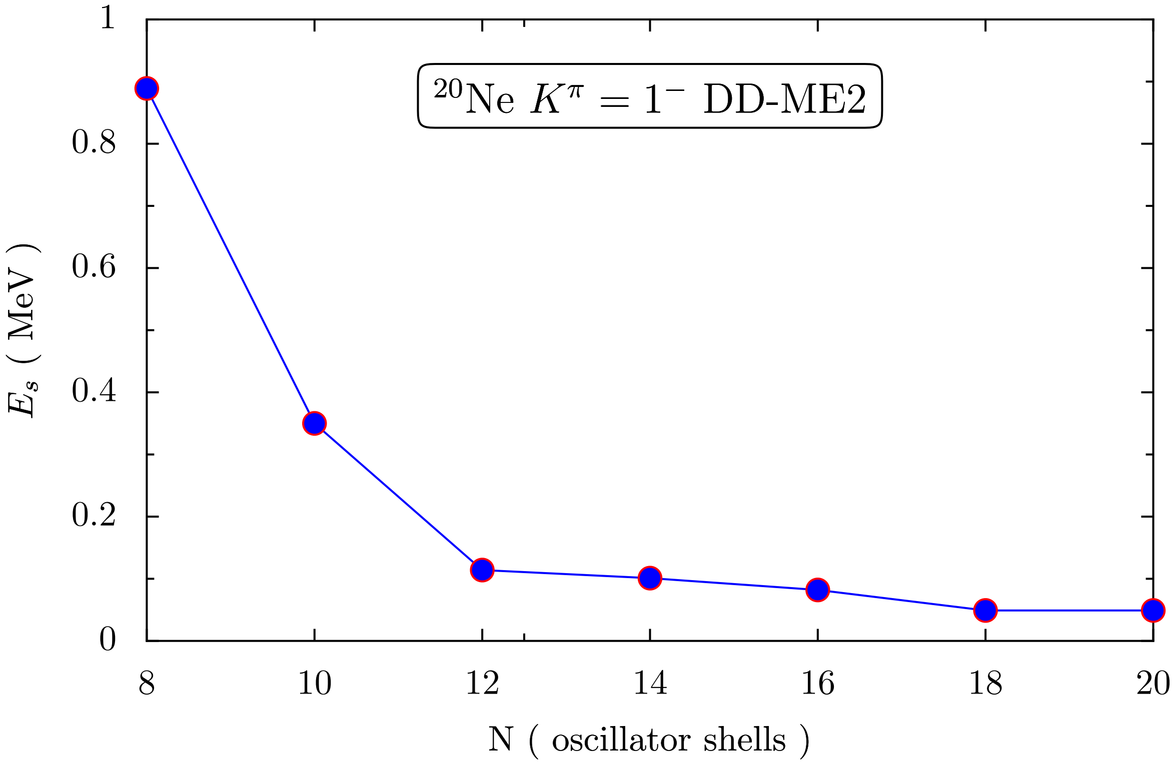

Figure 5.5: Translational spurious mode dependence on the configuration space size for the DD-ME2 interaction.

in the present study the number of oscillator shells was chosen between 12 and 16, depending on the desired final precision and the availability of computer resources. It has to be stressed that convergence was throughly checked for all the results discussed.

It is interesting to note that, due to the sparseness of the lattice for the computation of the integrals, the procedure for the solution of the non-linear Klein Gordon equation introduces inaccuracies that are reflected in the position of the spurious modes, but not in the rest of the spectrum. Specifying the same numerical parameters, for the same nucleus, usually the spurious mode lies somewhat closer to zero for the DDME and DDPC energy functionals than with the NLME energy functional. However, the difference is minimal, and, in general, the most accurate calculations when comparing with experimental data are achieved using the already quite veteran NL3 parameter set.

Perhaps more important that the position of the spurious modes is their actual admixture with the real physical states. For the same reasons the spurious mode does not appear at exactly zero energy, the physical states are not completely orthogonal (in the sense of Equation (4.13)) to it, and thus producing unreal results and overestimated strength distributions. As another confirmation of the validity of the implementation

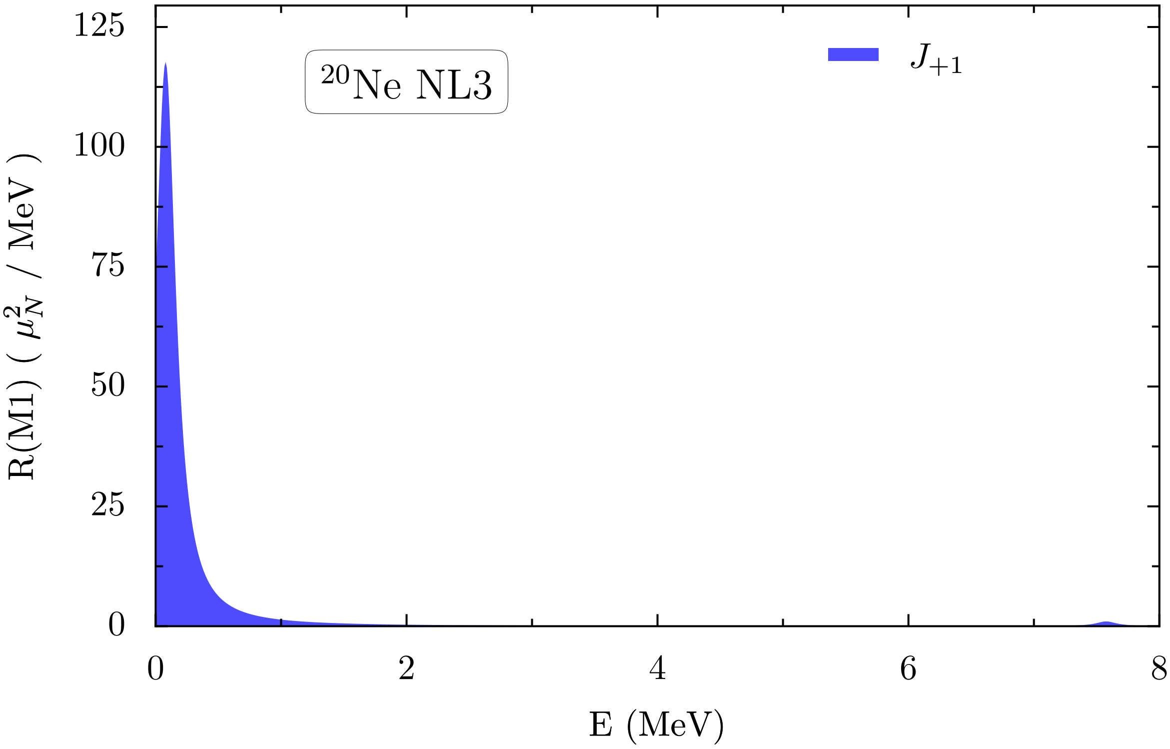

Figure 5.6: Response in ^{20}Ne to the operator J_{+1}, generator of rotations around a perpendicular of the symmetry axis. Almost 100% of the strength is exhausted by the spurious mode (0.08 MeV for ^{20}Ne, 0.15 MeV for ^{156}Gd), minimizing its admixture with the real physical states.

and its accuracy, when the spurious mode is located below 1 MeV, the RPA orthogonality relation is preserved with a precision of 10^{-10} between different states and the actual norm of the spurious state is over 10^3 smaller than the next smallest norm. As an example of the low expected admixture of spurious components with physical states, Figures 5.6 and 5.7 shows the response to the rotational spurious generator, the operator J_{+1} which represents rotations around a perpendicular of the symmetry axis. Almost 100% of the strength is exhausted by the spurious modes, located at 0.08 MeV for ^{20}Ne and 0.15 MeV for ^{156}Gd.

There is still another test that can be devised in order to check the consistency of the whole framework, namely the conservation of spherical symmetry. Even though all the formulas are particularized to the case of axial symmetry, the interaction is rotationally invariant, so they should still be valid when a spherical ground-state is taken as basis for the RPA configuration space, i.e., they should preserve spherical symmetry.

In Figures 5.8 and 5.9 is plotted the E1 excitation strength for the spherical nuclei ^{16}O and ^{142}Nd. Since the E1 operator is a rank-one tensor, it has three possible angular momentum projections, $K = -1, 0, 1$, that have to be calculated separately. The

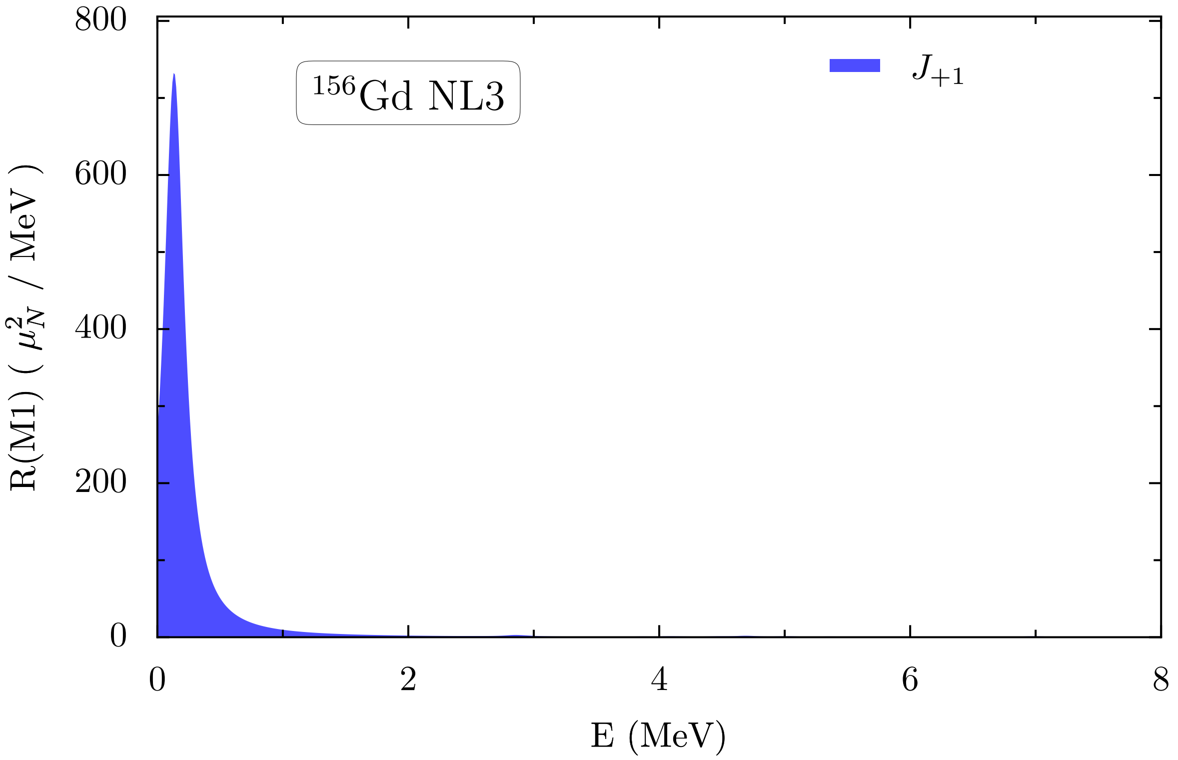

Figure 5.7: Same as Figure 5.6 for ^{156}Gd. The spurious mode is located at 0.15 MeV.

response for the modes with $K = -1$ and $K = 1$ are identical and correspond to vibrations perpendicular to the symmetry axis, i.e. one can calculate only one of them and double its contribution. The $K = 0$ mode corresponds to vibrations along the symmetry axis. If the nucleus is prolate, like ^{20}Ne, the response for in the $K = 0$ mode should lie at lower energies than the $K = 1$ mode, as the potential is flatter in the direction of the symmetry axis. However, if the nucleus is spherical, like ^{16}O and ^{142}Nd, there is no distinction between the $K = 0$ and $K = 1$ modes, and their corresponding excitation strength should lie at exactly the same energies. From Figures 5.8 and 5.9 we can attest that, in fact, the procedure for the solution of the RPA equation in axial symmetry indeed preserves rotational symmetry to a high degree of accuracy.

In summary, we have shown, with the results concerning the decoupling of the spurious modes and the preservation of spherical symmetry, that the computer implementation indeed solves the equations posed by the self-consistent RHB+RQRPA framework in axial symmetry. We have also ascertained that a high degree of accuracy can be achieved in real calculations, as well as validated the good reproduction of formal and mathematical aspects of the RPA theory. In the next two chapter we shall study the response of different deformed nuclei to the action of the M1 and E1 operators. With confidence in the numerical implementation, we shall relegate the numerics and concentrate in physical aspects and comparison of the results with the available experimental

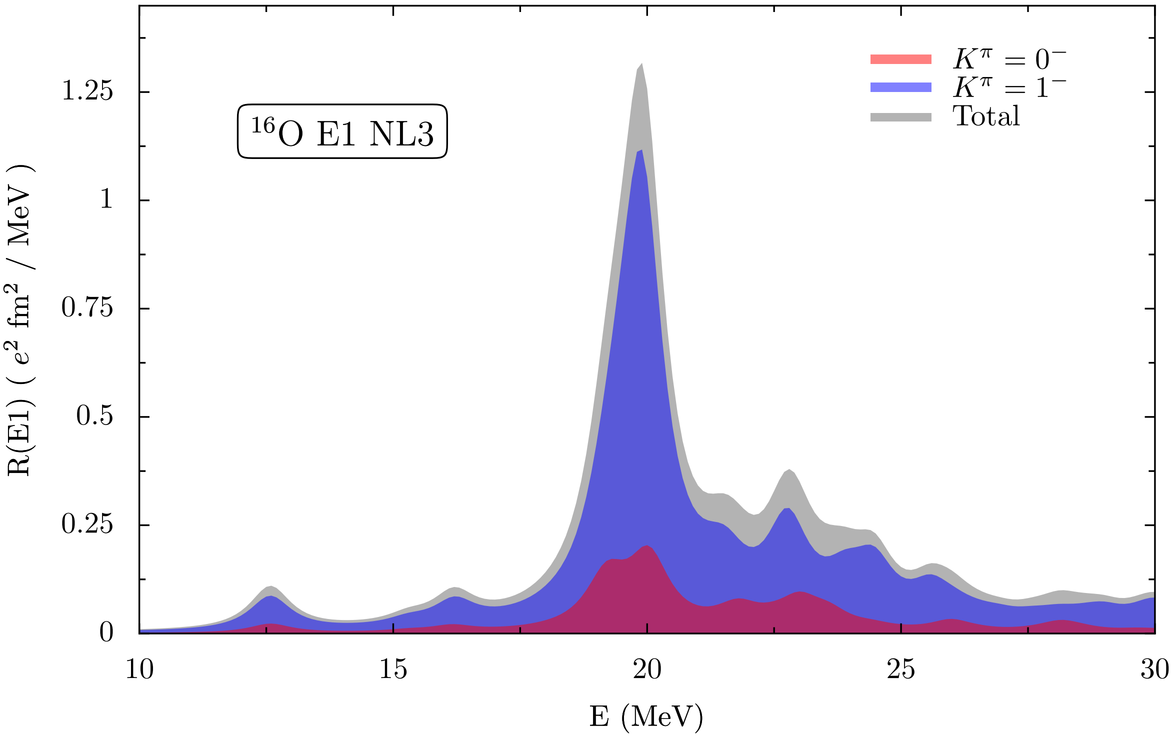

Figure 5.8: $K^\pi = 0^-$ and $K^\pi = 1^-$ response to the E1 transition operator for the spherical nucleus ^{16}O.

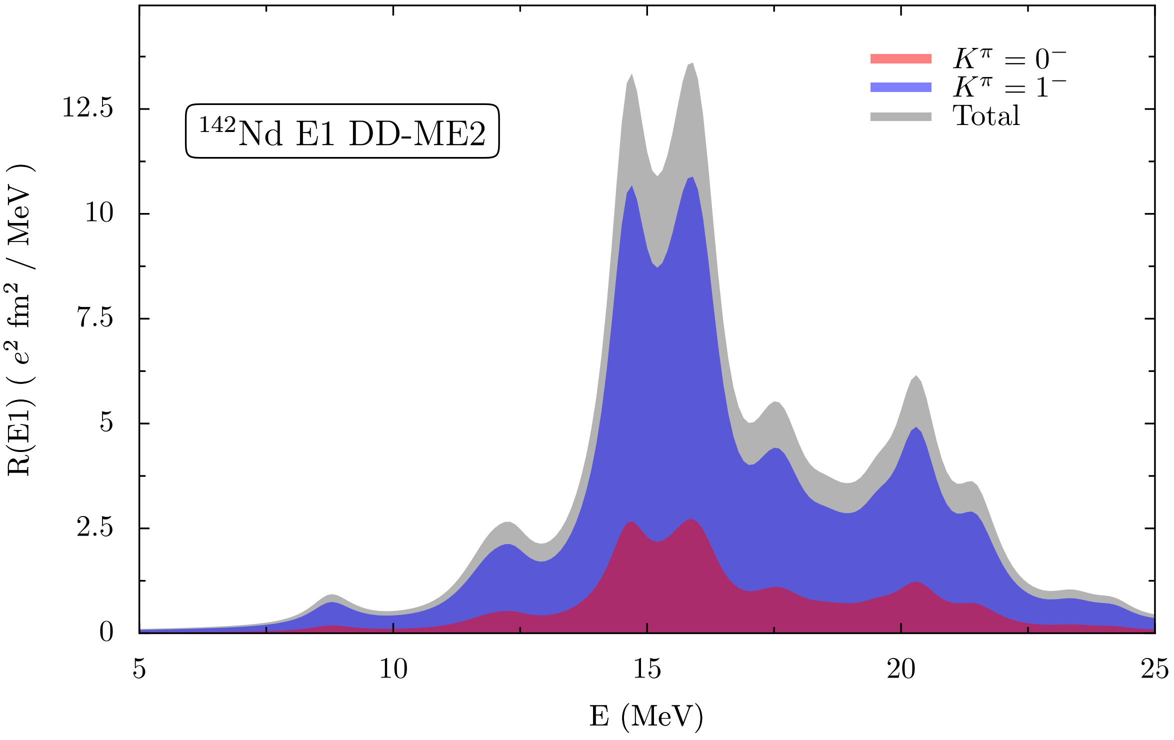

Figure 5.9: $K^\pi = 0^-$ and $K^\pi = 1^-$ response to the E1 transition operator for the spherical nucleus ^{142}Nd.

data.

Chapter 6

M1 transitions in deformed nuclei

"The most exciting phrase to hear in science, the one that heralds new discoveries, is not 'Eureka!' but 'That's funny...'."

— Isaac Asimov, 1920-1992

The discovery of low-lying M1 excitations, known as scissors mode, was made by Richter and collaborators in ^{156}Gd in Darmstadt through a high-resolution inelastic electron scattering experiment [25]. The search for such a mode was stimulated by the prediction, made within the Two Rotor Model [98, 64, 147], of a collective M1 mode promoted by a rotational oscillation of proton versus neutron densities. In fact, the name "scissors mode" was indeed suggested by such a geometrical picture. An excitation of similar nature was also predicted by other models [69, 1, 63].

The discovery led to a renaissance of low-energy nuclear spectroscopy in the mid-80's, and the mode has been detected in most of the deformed nuclei ranging from the fp-shell to rare-earth and actinide regions. The mode has been well characterized, and it is well established that it is fragmented into several closely packed M1 transitions. In even-even nuclei the total magnetic dipole excitation strength of the scissors mode is closely correlated to the strength of the 2_1^+ state [69, 1, 63] and, thus, depends quadratically on the nuclear deformation parameter [125, 126, 127, 129, 160].

A byproduct of the systematic study of the "scissors mode" was the discovery of spin excitations. Inelastic proton scattering experiments on ^{154}Sm and other deformed nuclei [50] found a sizable and strongly fragmented M1 spin strength distributed over an energy range of 4 MeV to 12 MeV. The experimental discovery stimulated the proliferation of theoretical investigations, were most of the microscopic studies [65] were carried out in the RPA or TDA approximation.

Even though the Two Rotor Model is too simple to fully explain the low-lying strength found in M1 transitions, it will be outlined as to give an intuitive picture where to base the interpretation of the following results. In the next section basic facts about the experimentally found nature of the M1 will be presented. Then the deformed QRPA framework outlined in the previous chapters will be applied to the study of M1 transitions in several sample nuclei. Results for light and heavy nuclei, calculated with the different relativistic density functionals, will be presented and compared with available experimental data.

6.1 The Two Rotor Model (TRM)

In principle, the angular momentum carried by the nucleus does not produce any intrinsic excitation. This reflects the spherical symmetry of the nuclear interaction just as its translational invariance forbids the occurrence of an isoscalar collective E1 mode. One can, however, extend further the analogy with dipole translations and assume that protons and neutrons have two distinct deformed densities that are free to rotate separately about a common axis (perpendicular to their symmetry axis in the case of axial deformation). Because of their mutual interaction, they may undergo a rotational oscillation giving rise to an intrinsic M1 excitation. Because the excitation mechanism is similar to that of the Giant Dipole Resonance, it was named Giant Angular Dipole (GAD). This is the underlying idea of the TRM [98], which represents the rotational counterpart of the semi classical picture of the E1 giant resonance [57, 145]. One can readily write a Hamiltonian for such a model as

$$H_{TR} = \frac{1}{2\mathcal{J}_p}\boldsymbol{J}_p^2 + \frac{1}{2\mathcal{J}_n}\boldsymbol{J}_n^2 + V(\theta) \tag{6.1}$$

where $\mathcal{J}_p$ and $\mathcal{J}_n$ are the proton and neutron moments of inertia and $\boldsymbol{J}_p$ and $\boldsymbol{J}_n$ are their angular momenta. Expressed in terms of the total and relative momenta

$$\boldsymbol{J} = \boldsymbol{J}_p + \boldsymbol{J}_n \qquad S = \boldsymbol{J}_p - \boldsymbol{J}_n \tag{6.2}$$

and neglecting a Coriolis-like term, the Hamiltonian decouples into a rotational and an intrinsic part. For small values of θ, the intrinsic part assumes the form of a two-dimensional harmonic oscillator Hamiltonian

$$H_{int} = \frac{1}{2\mathcal{J}_{sc}}(S_1^2 + S_2^2) + \frac{1}{2}C_\theta(\theta_1^2 + \theta_1^2) \tag{6.3}$$

where θ_k $(k = 1, 2)$ play the role of coordinates in the intrinsic frame of reference and S_k $(k = 1, 2)$ that of their conjugate momenta. The TRM Hamiltonian parameters are thus $\mathcal{J}_{sc}$ and C_θ, that correspond to the effective moment of inertia and the spring oscillator constant, respectively. The energy eigenvalues of this simple Hamiltonian are

$$\omega_{n,K} = \omega(2n + K + 1) \tag{6.4}$$

The scissors mode corresponds to the first excited level, with quantum numbers $n = 0$ and $K = 1$, that defines a positive parity band of intrinsic excitation energy ω. Decomposing in a rotational and intrinsic parts following the TRM, one obtains for the M1 intrinsic strength the expression

$$\mathcal{M}(M1, \mu) = \frac{3}{16\pi}\mathcal{J}_{sc}\omega(g_p - g_n)^2\mu_N^2 \tag{6.5}$$

6.2 Nature of low-lying M1 excitations

A level with the properties of the $J^\pi = 1^+$, $K^\pi = 1^+$ state predicted by the TRM was discovered in a high resolution (e, e') experiment on ^{156}Gd [25]. It was detected by scattering at backwards angles, where transverse magnetic transitions are dominant. The analysis of the experimental data soon revealed that the simple picture of two fluids rotating against each other of the TRM was not able to explain the full spectrum. The discrepancy was linked to the absence of spin contributions in the TRM [23, 124]. Further (γ, γ') experiments [17] confirmed the existence of this strongly excited state. Subsequent experiments were able to confirm the existence of the mode in three regions of the nuclear table, i.e., the deformed rare-earth nuclei, the fp-shell nuclei and the actinides. Its absence in (p, p') reactions provided a strong evidence in favour of the orbital nature of the mode, while joint (e, e') and (γ, γ') experiments [24] showed that the mode is fragmented into several peaks closely packed around a prominent one with a total strength $B(M1) \uparrow \approx 3\mu_N^2$ that grows quadratically with the deformation parameter [173] and is proportional to the strength of the E2 transition to the lowest 2^+ state [120]. The main features extracted from several review articles on the experimental status can be summarized as:

- The M1 strength is fragmented and distributed around an energy centroid, which has an approximate value of 3 MeV in rare-earth nuclei.

- The transition is mainly promoted by the convection current. The orbital response is typically an order of magnitude bigger than the spin one.
- The integrated M1 strength depends quadratically on the deformation parameter and is strictly correlated with the strength of the E2 transition to the lowest 2^+ state.

While consistent with the observed properties of the mode on a qualitative round, the TRM is unable to predict either the exact position of the energy centroid nor the size of the total strength.

6.3 M1 transition in the RQRPA

The goal of QRPA and RQRPA calculations for the scissors mode is very clear, and can be summarized in the following points. They should i) account for the collective properties of the mode such as the quadratic deformation dependence of the total M1 strength, ii) put on display the microscopic structure of the M1 states so as to enable one to decide about the true nature of the mode, and iii) test the ability of the different density functionals to reproduce the energy distribution of the M1 strength.

Concerning the first point, calculations carried out by different groups using not self-consistent interactions have already reproduced fairly well the deformation law [59, 118, 62]. The crucial role of pairing correlations in enforcing such a law was particularly stressed, so it is not clear whether with the simple BCS approximation used in the present approach is good enough.

As mentioned before, the experimental systematic study of the scissors mode has led to the discovery of spin excitations [51, 128]. These have been detected in ^{154}Sm and ^{156}Gd in the energy range of 5-11 MeV and have very peculiar properties. The profile of the spectrum exhibits two distinct bumps. These transition have been studied with relatively good success in the TDA [41, 42] as well as in RPA [169, 170, 101, 118]. There is however no conclusive answer to the interpretation of the observed two-peak structure. It is indeed not clear whether these two peaks correspond to different proton and neutron excitations or are of isovector and isoscalar nature. RPA calculations have been carried out to describe the M1 excitations not only in rare earth nuclei, but also in actinides [49, 107], in medium-light [106] and medium nuclei [105]. On the whole, the results are satisfactory. An unsolved problem remains however. The energy distribution of the M1 strength is not well reproduced. This suggests that maybe the RPA space should be enlarged so as to allow for higher configurations. In the present study this configuration space has been taken as large as possible within the limits of the hardware used. Convergence of the results has been throughly checked. Because the approach is fully self-consistent, many problems that plague other theoretical studies like admixtures with spurious modes, are avoided. In particular, no further parameters need to be adjusted. The same interaction used in the ground state is used for the excited states calculation. However, as happens with other low-lying excitations, the scissors mode and spin excitations are very sensitive to the single particle structure around the Fermi energy. It is a known problem of the self consistent approaches in general, and of the relativistic approach in particular, to the nuclear many-body problem, that the effective mass is too low [161] as to be able to reproduce well the single particle structure. The coupling to collective surface vibrations plays an important role and is not taken into account on the RPA level.

6.3.1 Matrix elements of the M1 excitation mode

The M1 operator is defined as [133]

$$\hat{M}_{1\mu} = \mu_N \left(g_s \mathbf{s} + g_l \mathbf{l} \right) \cdot \left(\nabla r Y_{1\mu}(\theta, \phi) \right) \tag{6.6}$$

with g_s the gyromagnetic factor for protons and neutrons and $g_l = 0, 1$ for neutrons and protons respectively. The angular momentum operator $\mathbf{l}$ acts only on the coordinates of the wave function and not on the spherical harmonic $Y_{1\mu}$. The matrix element that connects an initial state $|i\rangle$ and a final state $\langle m|$ is

$$\langle m|\hat{M}_{1\mu}|i\rangle = \mu_N \delta_{\Omega_m - \Omega_i, \mu} \frac{1}{\sqrt{2}} \sqrt{\frac{3}{4\pi}} \int r \mathrm{d}r \mathrm{d}z F_\mu(r, z) \tag{6.7}$$

where $F_\mu(r, z)$ is a function that depends on the upper and lower components of the Dirac spinor. Its full expression for the case of axial symmetry can be found in the Appendix B.

6.3.2 Scissors mode in ^{20}Ne

As a first application of the RHB+RQRPA framework we have undertaken a model study of the first multipole magnetic excitations in ^{20}Ne. This nucleus offers several advantages. Its ground state is well deformed and exhibits a prolate shape in the RHB model, with a quadrupole deformation parameter $\beta \approx 0.5$. Another advantage is the reduced number of nucleons to take into account in the calculations, which translates in fast running times and thus in the possibility of detailed analysis. With the optimal number of oscillator shells for a full precision ground state calculation, the number of *qp* pairs never exceeds five thousand. Furthermore, because the number of protons and neutrons is the same, switching off the electromagnetic interaction should give similar results for both protons and neutrons. Using this technique, very detailed checks can be carried out on the isospin part of the interaction, and its consistency can be further established. Finally, the absence of pairing correlations simplifies both the handling of numerical factors that influence the results and their interpretation. These reasons make ^{20}Ne the ideal theoretical playground where to introduce the concepts that will later be used in the study of more complex systems.

Figure 6.1 shows the response in ^{20}Ne to the M1 magnetic dipole operator that has been previously defined. Results for two parameter sets corresponding to two functionals are presented one above the other for easy comparison. The non-linear meson exchange functional using the NL3 parameter set will be used as a reference in all further calculations. Its maturity and proven performance make it the perfect choice. In order not to clutter the document with excessive details and many plots, we will present results only for one of the other two functionals to compare their performance. In this case we have chosen the DDPC functional, even though there is no available parameter set that can match the performance of the best forces for the other two functionals. Nevertheless, it is interesting to see how well it does.

In both cases the calculations were performed with the maximum precision allowed by the current implementation of the computer code. The number of pairs is around five thousand. Optimal numerical parameters were chosen with the aid of the study presented in the last chapter. The rotational spurious mode is well separated, situated for both functionals below 0.1 MeV, i.e. no admixture with the vibrational response is observed. The total M1 response is depicted in Figure 6.1, as well as the orbital $\mathbf{l}_{M1}$ and spin $\mathbf{s}_{M1}$ contributions

$$\mathbf{l}_{M1} = \mu_N g_s \mathbf{s} \tag{6.8}$$

$$\mathbf{s}_{M1} = \mu_N g_l \mathbf{l} \tag{6.9}$$

Only one prominent peak is found around 6 MeV. In the case of the NL3 parameter set its exact position is 5.7 MeV. For the point coupling functional with the PC-F1 parameter set, it is slightly shifted to a higher energy, 5.9 MeV. Calculations performed with the three functionals best parameter sets (NL3, DD-ME2 and PC-F1) show good agreement, with an energy dispersion of less than half an MeV in the position of the main peak. Regrettably, there is no experimental data available for the magnetic response in this nucleus. Theoretical studies using large scale shell model calculations [36] predict a low lying orbital mode around 11 MeV for ^{20}Ne, in disagreement with the results presented in this study. However, other calculations [97] performed in ^{22}Ne,

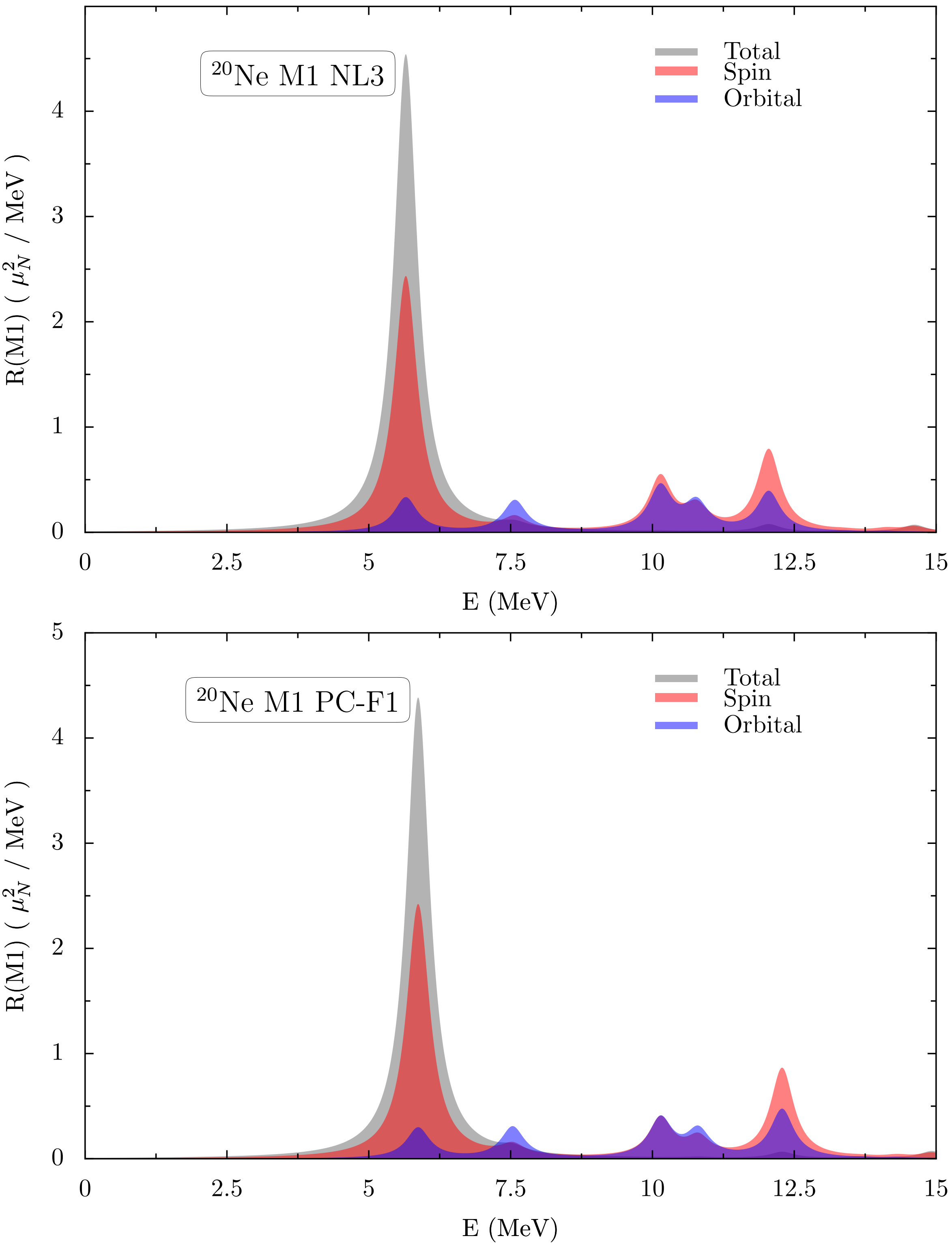

Figure 6.1: M1 Excitation strength for ^{20}Ne, using the NL3 parameter set on the upper plot and PC-F1 on the lower plot. A very well developed peak can be seen around 5.8 MeV in both cases. Its structure is composed mostly of spin flip transitions.

with the same shell model interaction, exhibit two dominant low lying peaks around 5-6 MeV. The orbital character of these two modes is less than 25% of the total response. This is in better agreement with results found within our RHB+RQRPA calculations, where fragmented strength with similar characteristics is found in the same energy region.

Regarding the contributions from the orbital and spin components of the M1 operator to the total response strength, it can be observed in Figure 6.1 that there are two differentiated energy regions. Around the main excitation peak at 6 MeV there is an enhancement of the response due to the addition of the orbital and spin contributions. In contrast, in the energy region above 6.5 MeV it is the opposite, both contributions cancel. This feature of the M1 strength distribution is much more evident when studying heavier nuclei and will be discussed in detail in the next section in Gadolinium isotopes,

From the figure it can also gathered that the main contribution to the total response strength comes from spin excitations. The supposed orbital character of the low lying spectra in the M1 transitions is eclipsed by the preponderance of spin flip strength, three times larger than the orbital response. Again, this comes in disagreement with the cited theoretical calculations, which predict a much bigger orbital contribution to the total strength. However, low lying collective transitions in such a light nucleus as ^{20}Ne cannot be expected to be exceptionally well described by the RHB+RQRPA theory. In few nucleon systems, the single particle structure around the Fermi surface is of the utmost importance in the calculation of low-lying excitations. As such, the results produced in a self-consistent mean field calculation are not so reliable. A better description would require a proper account of excitations to the continuum above the coulomb barrier and probably for higher order correlations at the time dependent mean field level. The situation improves in heavier nuclei, were mean field theories were designed to yield good results at low computational costs. However, as will be shown in the next section on the study of Gadolinium isotopes, quantitative comparison of M1 excitation energies with experimental data still needs considerable improvement.

Nevertheless, it is still interesting to delve further into the study of the properties of the main excitation peak. Many of the general features will also be present in heavier nuclei, and a clear idea of what to expect is useful. The study of the structure of the excitation peaks can be carried out in detail attending to their single particle structure. The contribution C_{qph} from a particular proton or neutron qph configuration to a RPA state is determined by

$$C_{qph} = (|\mathcal{X}^{\nu}_{ph}|^2 - |\mathcal{Y}^{\nu}_{ph}|^2)\eta^{-}_{ph} \tag{6.10}$$

where the occupation factor η^{-} is defined in Equation (4.19). $\mathcal{X}^{\nu}$ and $\mathcal{Y}^{\nu}$ are the RQRPA amplitudes associated with a particular RQRPA excitation energy. Table 6.1

Peak at 5.7 MeV, NL3 parameter set			ΔE (MeV)
proton	49.1%	$-\frac{1}{2}^+([220]\,93\%) \rightarrow +\frac{3}{2}^+([211]\,94\%)$	5.15
neutron	48.9%	$-\frac{1}{2}^+([220]\,94\%) \rightarrow +\frac{3}{2}^+([211]\,95\%)$	5.22
proton	1%	$+\frac{1}{2}^+([220]\,93\%) \rightarrow +\frac{1}{2}^+([211]\,64\%)$	9.73
neutron	0.9%	$+\frac{1}{2}^+([220]\,94\%) \rightarrow +\frac{1}{2}^+([211]\,70\%)$	10.17

Peak at 5.9 MeV, NL3 parameter set			ΔE (MeV)
proton	49.0%	$-\frac{1}{2}^+([220]\,93\%) \rightarrow +\frac{3}{2}^+([211]\,94\%)$	5.31
neutron	48.9%	$-\frac{1}{2}^+([220]\,94\%) \rightarrow +\frac{3}{2}^+([211]\,95\%)$	5.42
proton	0.9%	$+\frac{1}{2}^+([220]\,93\%) \rightarrow +\frac{1}{2}^+([211]\,64\%)$	9.68
neutron	0.9%	$+\frac{1}{2}^+([220]\,94\%) \rightarrow +\frac{1}{2}^+([211]\,70\%)$	10.13

Table 6.1: *ph* structure for the 5.7 MeV and 5.9 MeV M1 transition mode in ^{20}Ne for NL3 and PC-F1 parameter sets, respectively. The second column refers to the normalization of the RPA amplitudes. The level quantum numbers in the third column are $\pm\Omega^\pi$, where $\pm\Omega$ is the angular momentum projection over the symmetry axis and π is the parity. In parenthesis are the quantum numbers of the oscillator state which contributes most to the mean field single particle level, with its corresponding percentage. The effect of coulomb interaction can be seen as the small differences in the mixing percentages for protons and neutrons. A calculation with the electromagnetic interaction switched off gives as a result a perfect isospin symmetry, with no differences observable within the accuracy of the computed results.

outlines the single particle decomposition of the dominant M1 peaks observed in Figure 6.1. For both density functionals all the strength of the excitation mode is provided by a single particle transition within the sd-shell, from the last level in the Fermi sea to the first consecutive unoccupied level. The low collectivity indicates that, within the RHB+RQRPA model, the spectrum of the M1 operator in ^{20}Ne is of single particle character.

It is difficult to form a mental image of the nature of the excitation with only the aid of Table 6.1. For that purpose, it is always useful to plot the neutron and proton transition densities and compare them. Figure 6.2 shows a color plot of the transition densities at an excitation energy of 5.7 MeV, for the case of the NLME functional. The color is used to indicate the value of the function, with blue for negative values and red for positive ones. Zones with the same color for both protons and neutrons are indicative of in-phase vibration, while regions where the color is different mean they are out-of-phase. In this case, there is only one region where the transition densities are non-zero and shows that it corresponds to an isovector transition mode, where the neutrons (left) vibrate in opposition to protons (right), i.e., the typical excitation

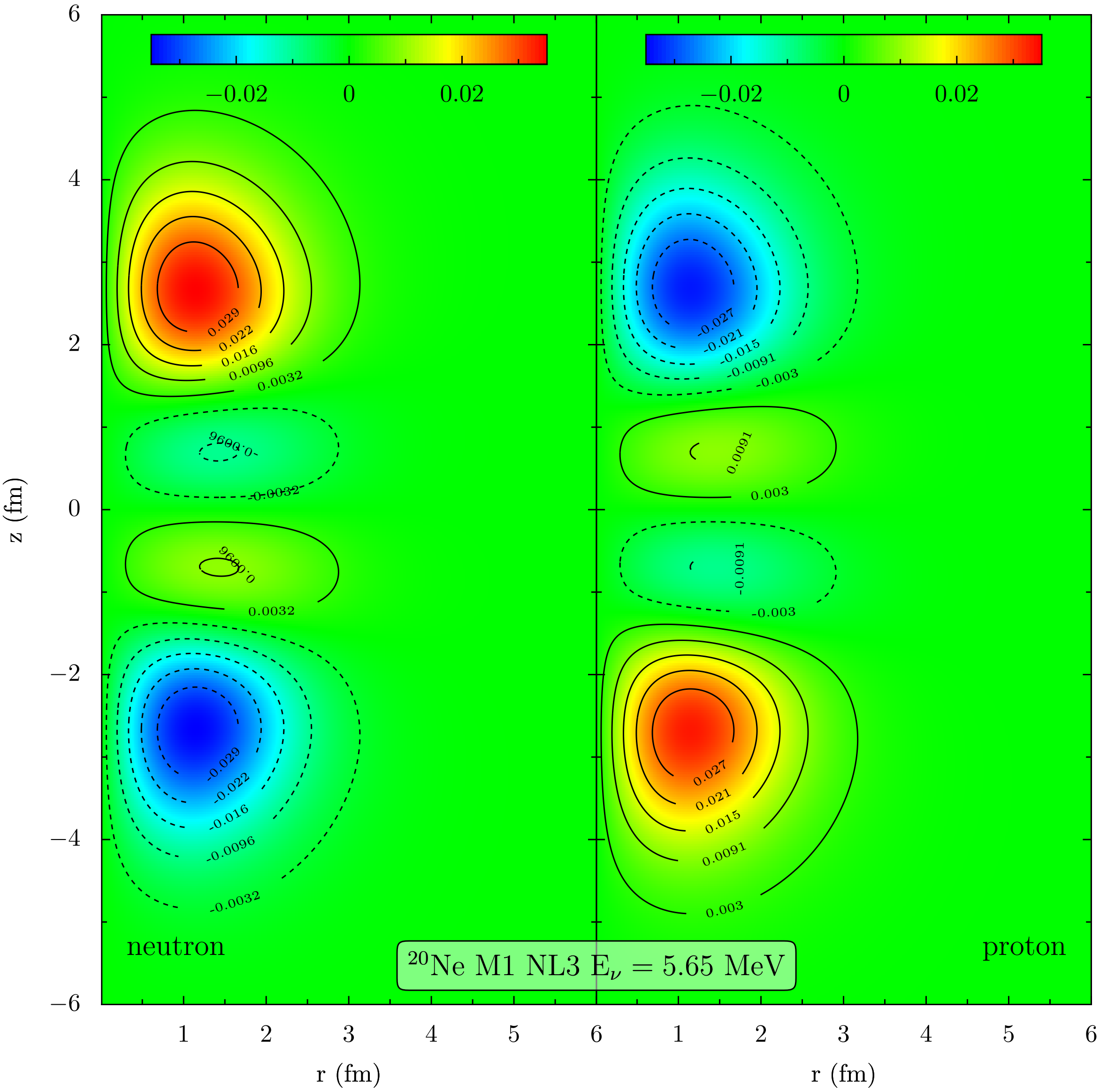

Figure 6.2: Color plot of the two dimensional transition densities for the M1 $K^\pi = 1^+$ peak at 5.7 MeV, as calculated with the NL3 parameter set. The left panel corresponds to the neutron transition density, while the right panel to the proton density. The color scale is the same for both plots; negative values appear in blue and positive ones in red. Solid contour lines depict positive values and dashed ones negative values. Even though the excited states have a well-defined parity, for clarity, the z-axis range has been extended to include also negative values. The well known scissors mode excitation pattern can be clearly recognized (refer to Equation (5.51)).

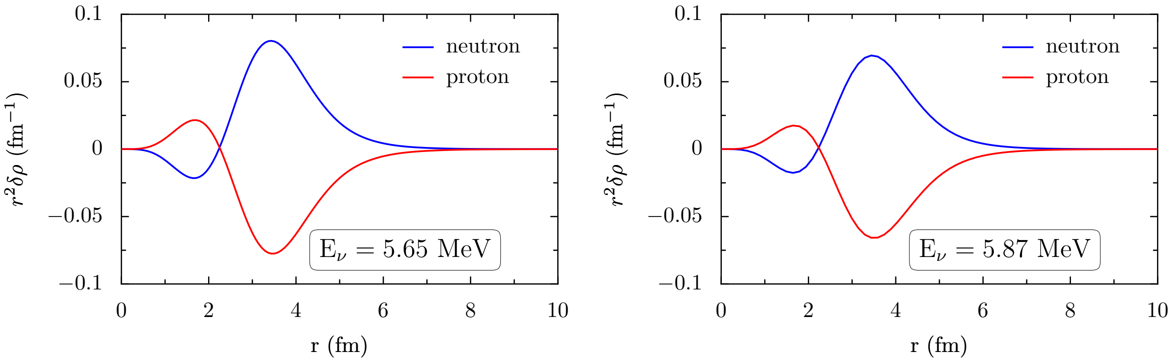

Figure 6.3: Radial part of the projected (to $J = 1$, $M = 1$) transition densities of the peaks at 5.7 MeV and 5.9 MeV for, respectively left and right, NL3 and PC-F1 parameters sets. The prominent isovector nature of the excitation is well reflected by the graphs.

pattern of the scissors mode.

In such a simple case as the one found in ^{20}Ne the interpretation of the two dimensional color plot for the transition densities is very clear. They represent the intrinsic transition densities, referred to the intrinsic frame of reference, where only the total angular momentum projection on the symmetry axis is well defined. In that regards, they are expected to contain admixtures from all possible angular momenta. However, the transition operator (M1 in this specific case) restricts to its own total angular momentum the major contributions from the transition densities to the total response strength. It is therefore very advisable to project out the weaker-contributing angular parts from the densities to obtain the actual transition density that would be observed in the laboratory frame of reference. For the M1 operator that means retaining only the contributions coming from $J = 1$ angular momentum, with the help of equation (5.55). In Figure 6.3 the radial part of such a projected transition density is plotted for the main peaks in the ^{20}Ne M1 response. The isoscalar and isovector transition densities are defined as

$$\begin{aligned} \delta\rho_{IS} &= \delta\rho_n + \delta\rho_p \\ \delta\rho_{IV} &= \delta\rho_n - \delta\rho_p \end{aligned} \tag{6.11}$$

and are a direct measure of how neutrons and protons vibrate in-phase or out-of-phase, respectively. The almost nonexistent isoscalar transition density is a clear indicative of the pure isovector nature the mode at 6 MeV for the M1 operator in ^{20}Ne. In simple geometrical terms it can be interpreted as a rotation of neutrons against protons around the perpendicular of the axis of symmetry. Furthermore, details in Figure 6.2 show that two distinct regions can be distinguished. They are separated at around 2 fm from the origin, where the direction of rotation for protons and neutrons changes. The traditional qualitative picture given to this particular excitation mode is to consider the neutrons and protons densities as the blades of a scissor, and represent their movement as the one it makes when operated. In addition, one has to take into account the angular momentum inherent in a $K = 1$ excitation: it could be regarded as the movement made by a scissors when in operation, and at the same time rotating around its longitudinal symmetry axis. However, the picture we find is a little different. The sole appearance of two regions (as depicted in Figure 6.3) is a strong hint that the simple picture of the proton density rotating against the neutron density as rigid rotors (as in the TRM model) does not reflect reality. In the next section, with the study of the M1 response in ^{156}Gd, we shall see how the scissors mode looks like in a heavy nucleus, and how it can be interpreted in geometrical terms.

6.3.3 Scissors mode in ^{156}Gd

Even though the study of the scissors mode in light nuclei, like for example ^{20}Ne, is a very good academic exercise to become familiar with the techniques and main physical features, it is in heavy nuclei where the true character of a collective orbital mode like the low lying M1 response can be fully investigated. In particular, as a starting point for the study of M1 excitations in heavy nuclei within the RHB+RQRPA framework, we have chosen ^{156}Gd, the nucleus where it was first experimentally observed the scissors mode [25]. In that experiment, it was shown the existence of a low lying M1 collective mode with an excitation energy of 3.075 MeV and heavy fragmentation, that consumed approximately $3\,\mu_N^2$ of the total energy weighted sum rule.

RHB calculations of ^{156}Gd predict a normally deformed prolate nucleus with a quadrupole deformation parameter of $\beta = 0.3$, in agreement with experimental data. Its open shell character requires the inclusion of pairing correlations at the mean field level, and, for consistency, in the RPA interaction. However, the realistic calculation of collective excitations in such a heavy nucleus, with pairing correlations, is both a challenge and a very good performance test on the future practical applications of the framework presented in this document. With a very large configuration space, drastic cutoffs in the numerical parameters where needed in order to make the computations feasible. The particle energy cutoff was taken at 65 MeV, the antiparticle one at -1650 MeV. The quasiparticle cutoff parameter was fixed at 0.1 . These restrictions limit the number of quasiparticles to a little more than fourteen thousand. The pairing strength constants for neutrons and protons were adjusted to reproduce the experimental energy gap ($\Delta_n = 1.2$ MeV, $\Delta_p = 1.3$ MeV), as calculated with a simple three point formula from even-odd mass differences [133]. With these numerical parameters the position of the rotational spurious mode is around 0.15 MeV. Full convergence of the results was observed already within ten thousand *qp* pairs even if the separation of the spurious mode was not perfect.

Figure 6.4 shows the transition strength of the M1 transition operator in ^{156}Gd for two different functionals, the NLME with the NL3 parameter set on the upper plot and the DDME with the DD-ME2 parameter set on the lower plot. In the calculated spectrum there are two main different regions that can be distinguished. Below 5 MeV, the response has a strong orbital component that adds up with the spin excitation strength to give the total M1 strength. On the other hand, in the energy interval 5-10 MeV, the orbital response contribution is much weaker in comparison with the spin-flip contribution to the total strength. In addition, it is worth to note that in this energy region the orbital and spin contributions cancel each other.

Both models perform equally well in predicting the position of the scissors mode, with a very similar overall shape for the M1 operator response. The experimental data point is the position of the main scissors peak found in [25]. Heavy fragmentation is observed around a mean energy of 3 MeV, in good agreement with the conclusions of reference [25]. Even though the folded response (with a Lorentzian with a folding parameter of $\Gamma = 0.2$ MeV) for both models is remarkably similar, several differences appear in the fine grained structure. In the case of the DD-ME2 parameter set the main contribution to the 2.5-3 MeV peak comes from only one RPA excitation mode, located at 2.75 MeV. The orbital contribution to the strength is roughly double than of the spin one. On the other hand, for the NL3 parameter set two different RPA excitation modes, located at 2.6 MeV and 2.61 MeV, contribute to the overall response in the vicinity of the 2.5-3 MeV peak.

This discrepancy has its origin in numerical inaccuracies connected with the truncation of the *qp* configuration space. The effect of slightly different pairing interaction constants and the number of *qp* pairs used in the different calculations influence the final precision. These inaccuracies occur mostly in the low lying energy region where the level configuration near the Fermi energy is of great importance. However, attending to the single particle structure of the split RPA modes for the NL3 parameter set (see Table 6.2), one can easily conclude that they are fragmented parts of the same resonance. Both modes are composed of the same four main single particle transitions, being those with under 1% total contribution what differences them, and explains their slight energy deviation.

In Table 6.2 we present the single particle structure of the RPA excitation modes corresponding to the lowest lying orbital peak. For both models more than 75% percent of the strength of the mode is made up from three transitions, i.e., the collectivity is not very high. Most of that strength is provided by neutron excitations, while the protons

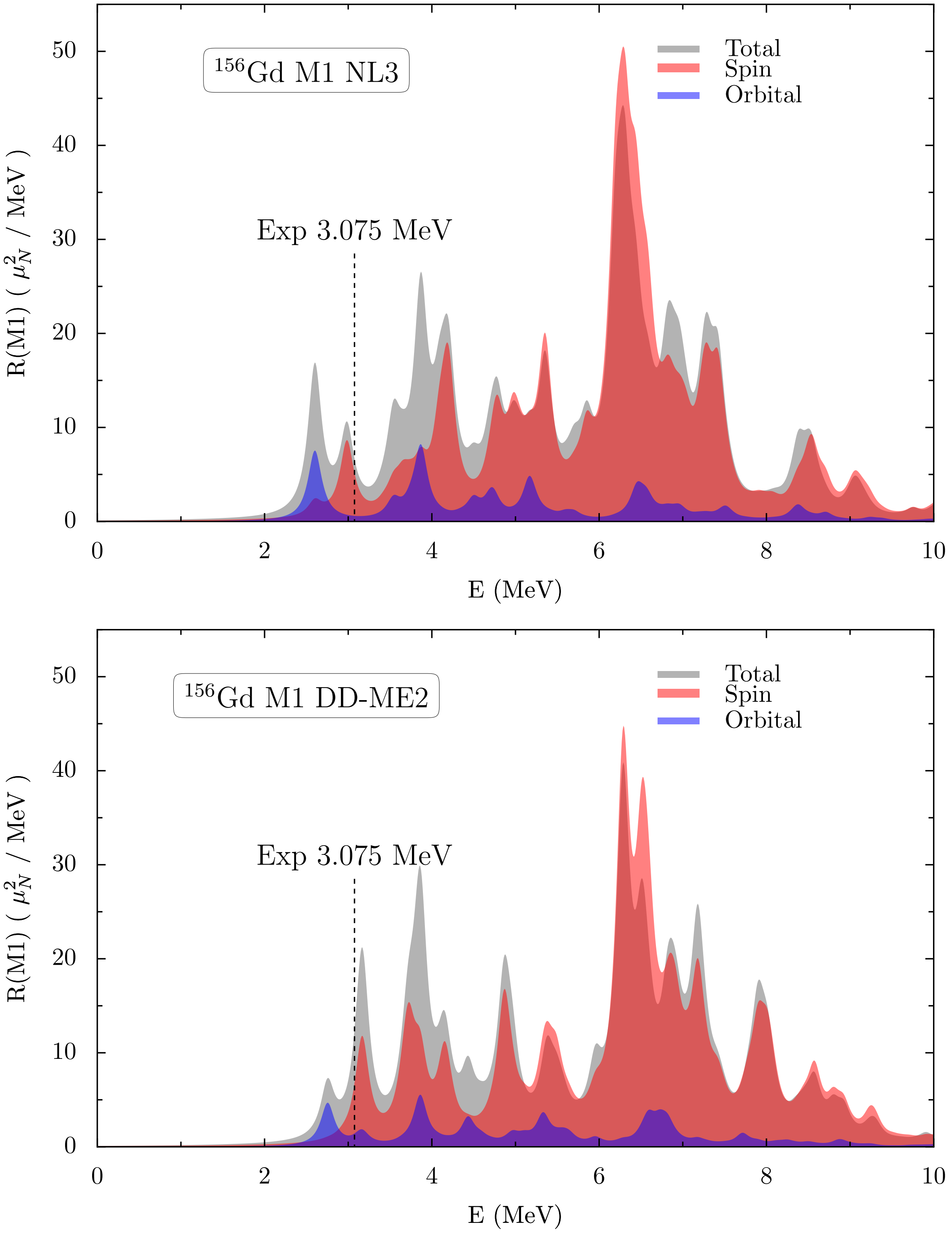

Figure 6.4: M1 excitation strength for ^{156}Gd (upper NL3, lower DD-ME2). The orbital response dominates in the low lying region at 2-5 MeV. On the other hand, in the energy interval 5-10 MeV the spin flip excitations provide most of the response. The experimental value for the scissors mode is 3.075 MeV. Two peaks with a strong orbital contributions are candidates to be labeled as the classical scissors mode, situated at 2.6 MeV and 4 MeV, respectively.

NL3 parameter set, M1 in ^{156}Gd

2.6 MeV				ΔE (MeV)
	neutron	45%	$-\frac{3}{2}^{+}([651]\,72\%) \rightarrow +\frac{5}{2}^{+}([642]\,82\%)$	2.66
	proton	30%	$-\frac{5}{2}^{+}([413]\,94\%) \rightarrow +\frac{7}{2}^{+}([404]\,95\%)$	3.32
	neutron	3%	$-\frac{3}{2}^{-}([532]\,84\%) \rightarrow +\frac{5}{2}^{-}([523]\,90\%)$	3.79
	neutron	3%	$-\frac{1}{2}^{+}([660]\,55\%) \rightarrow +\frac{3}{2}^{+}([651]\,72\%)$	2.90
2.62 MeV				ΔE (MeV)
	neutron	65%	$-\frac{3}{2}^{+}([651]\,72\%) \rightarrow +\frac{5}{2}^{+}([642]\,82\%)$	2.66
	proton	20%	$-\frac{5}{2}^{+}([413]\,94\%) \rightarrow +\frac{7}{2}^{+}([404]\,95\%)$	3.32
	neutron	1%	$-\frac{3}{2}^{-}([532]\,84\%) \rightarrow +\frac{5}{2}^{-}([523]\,90\%)$	3.79
	neutron	1%	$-\frac{1}{2}^{+}([660]\,55\%) \rightarrow +\frac{3}{2}^{+}([651]\,72\%)$	2.90

DD-ME2 parameter set, M1 in ^{156}Gd

2.75 MeV				ΔE (MeV)
	proton	56%	$-\frac{5}{2}^{+}([413]\,94\%) \rightarrow +\frac{7}{2}^{+}([404]\,96\%)$	3.43
	neutron	20%	$-\frac{3}{2}^{+}([651]\,73\%) \rightarrow +\frac{5}{2}^{+}([642]\,83\%)$	3.14
	neutron	7%	$-\frac{1}{2}^{+}([660]\,56\%) \rightarrow +\frac{3}{2}^{+}([651]\,73\%)$	3.25
	neutron	3%	$-\frac{9}{2}^{-}([514]\,96\%) \rightarrow +\frac{11}{2}^{-}([505]\,98\%)$	4.74
	proton	2%	$-\frac{3}{2}^{-}([541]\,78\%) \rightarrow +\frac{5}{2}^{-}([532]\,87\%)$	3.83

Table 6.2: *ph* structure of the lower dominant RPA excitation modes with orbital character in the M1 response for ^{156}Gd, for the NL3 and the DD-ME2 parameter sets.

play a relatively minor role. It is not very striking that all contributions come from the first transitions allowed by symmetry constrains from a level below the chemical potential to one just above. The orbital response is pushed up in energy by the influence of pairing correlations. We have performed test calculations in samarium isotopes that show clearly that, as the pairing constants are increased the position of the peaks with strong orbital component shift upwards. When the BCS pairing constants are taken to reproduce the experimental pairing gaps, the positions for the orbital response is roughly fixed with two strong peaks at ~ 2.5 MeV and ~ 4 MeV, regardless of the model interaction used. Even though a more detailed study would be necessary to draw a general conclusion, this fact strongly hints that the overall invariance of the position of the scissors mode is a direct consequence of the pairing interaction. Even though our feeling is that the BCS approximation is good enough in this specific case, it would be very interesting to be able to compare with a more elaborate pairing scheme.

The quantum numbers of the major oscillator contributor to the components of a excitation peak provide detailed structure information. These oscillator levels are characterized by quantum numbers n_z, n_ρ and Λ, where Λ is the projection of the orbital angular momentum on to the symmetry axis. With

$$N = n_z + 2n_\rho \tag{6.12}$$

being the major quantum number. For axial symmetry Λ is a good quantum number. The same is true for the spin component s_z and the z-component j_z of the total angular momentum, which has the eigenvalue

$$\Omega = \Lambda + m_s = \Lambda \pm \frac{1}{2} \tag{6.13}$$

Thus, it is usual to characterize the eigenstates of the harmonic oscillator Hamiltonian in axial symmetry by the set of quantum numbers

$$\Omega^\pi [N n_z \Lambda] \tag{6.14}$$

where π is the parity of the states ($\pi = (-1)^N$). In the notation used throughout this document we have added the sign of the total angular momentum projection as it is relevant for the formation of *qp* pairs with a good total angular momentum projection $K = \Omega_k + \Omega_{k'}$ with a definite sign.

$$\pm\Omega^\pi [N n_z \Lambda] \tag{6.15}$$

In the case of both peaks for the NL3 parameter set, the three most relevant single particle contributions share a common pattern in the change of the representative oscillator quantum numbers, i.e., for them it holds that $\Delta n_z = -1$ and $\Delta\Lambda = +1$. Thus there is no change of the spin projection over the symmetry axis. That means that the projection of the orbital angular momentum has to increase by one unit and confirms the strong orbital character of the peak. The major single-particle spin-flip contribution has a share of only 3%. Those single-particle components with less than 3% percent contribution generally are between levels that change the spin projection quantum number, i.e. $\Delta m_s = 1$. A similar situation is found for the DD-ME2 parameter set, where for the five major single-particle contributions it holds that $\Delta n_z = -1$ and $\Delta\Lambda = +1$. However, protons play a much more important role as their share is larger than 50% of the total strength. The first spin-flip contribution, as with the NL3 case, is below 1% of the total strength.

However, more informative, and perhaps better suited for geometrical interpretation than the single particle structure, are the total intrinsic transition densities. In Figures 6.5 and 6.6 we plot the intrinsic two dimensional transition densities for the RPA excitation modes contributing to the lowest lying peak with strong orbital component in their respective functionals. Even though the detailed structure is different, the

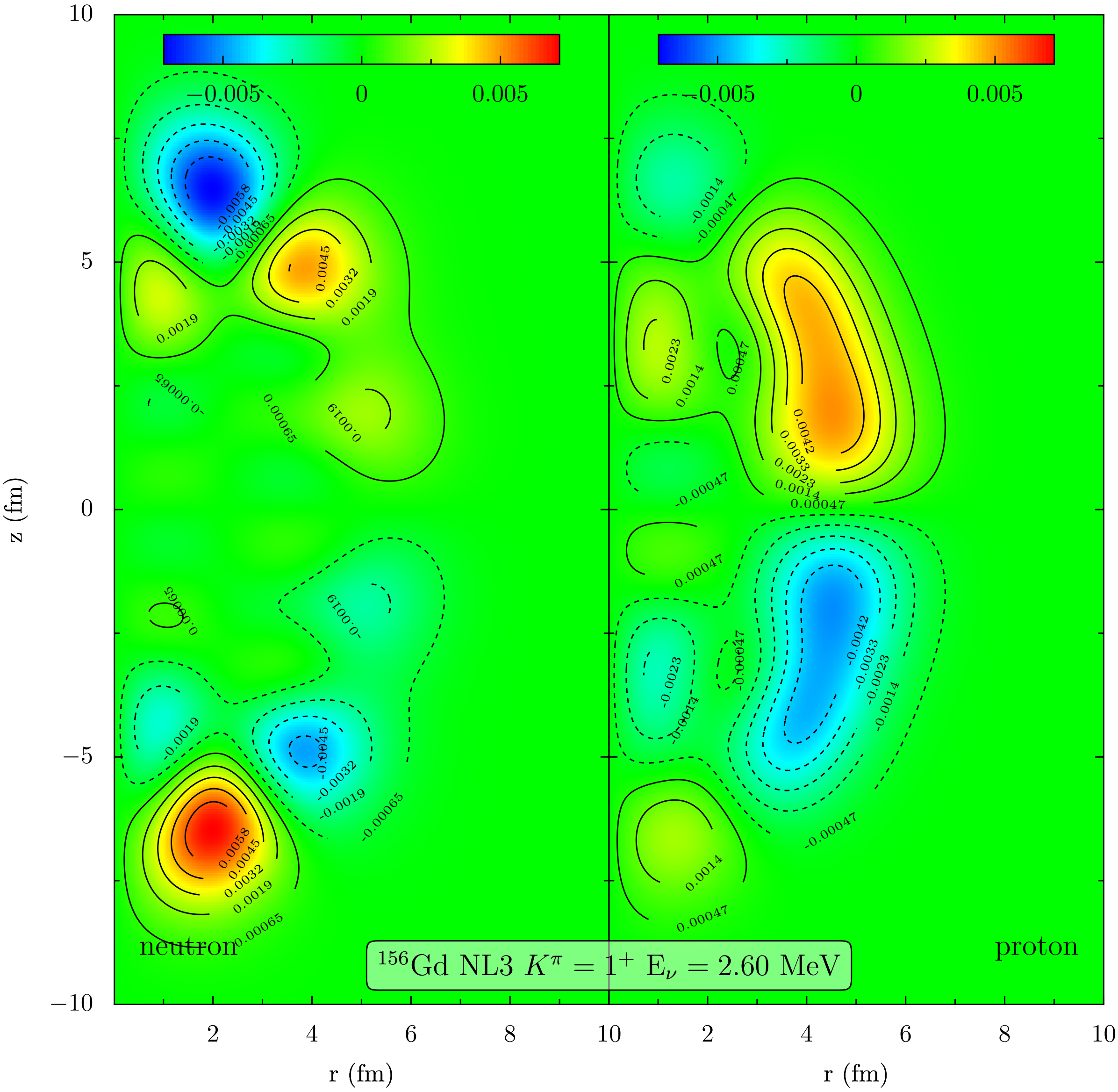

Figure 6.5: ^{156}Gd low lying orbital mode transition density, for the NL3 parameter set. Only one of the two excitation modes at ~ 2.6 MeV are plotted, as they show they same structure (see text for explanation). Both are similar to that calculated with the DD-ME2 parameter set (see Fig. 6.6).

total transition density main features are strikingly similar for both models. It is of particular interest the overall coincidence that can be observed in the shape for the split peak in the NL3 calculation, giving weight to their interpretation as the same excitation.

Attending to the different regions delimited by the contour lines, it is easily seen that in most of them the actual proton neutron vibration is in phase. What differs is their absolute value, not the sign of the result. In the regions where there is a high value

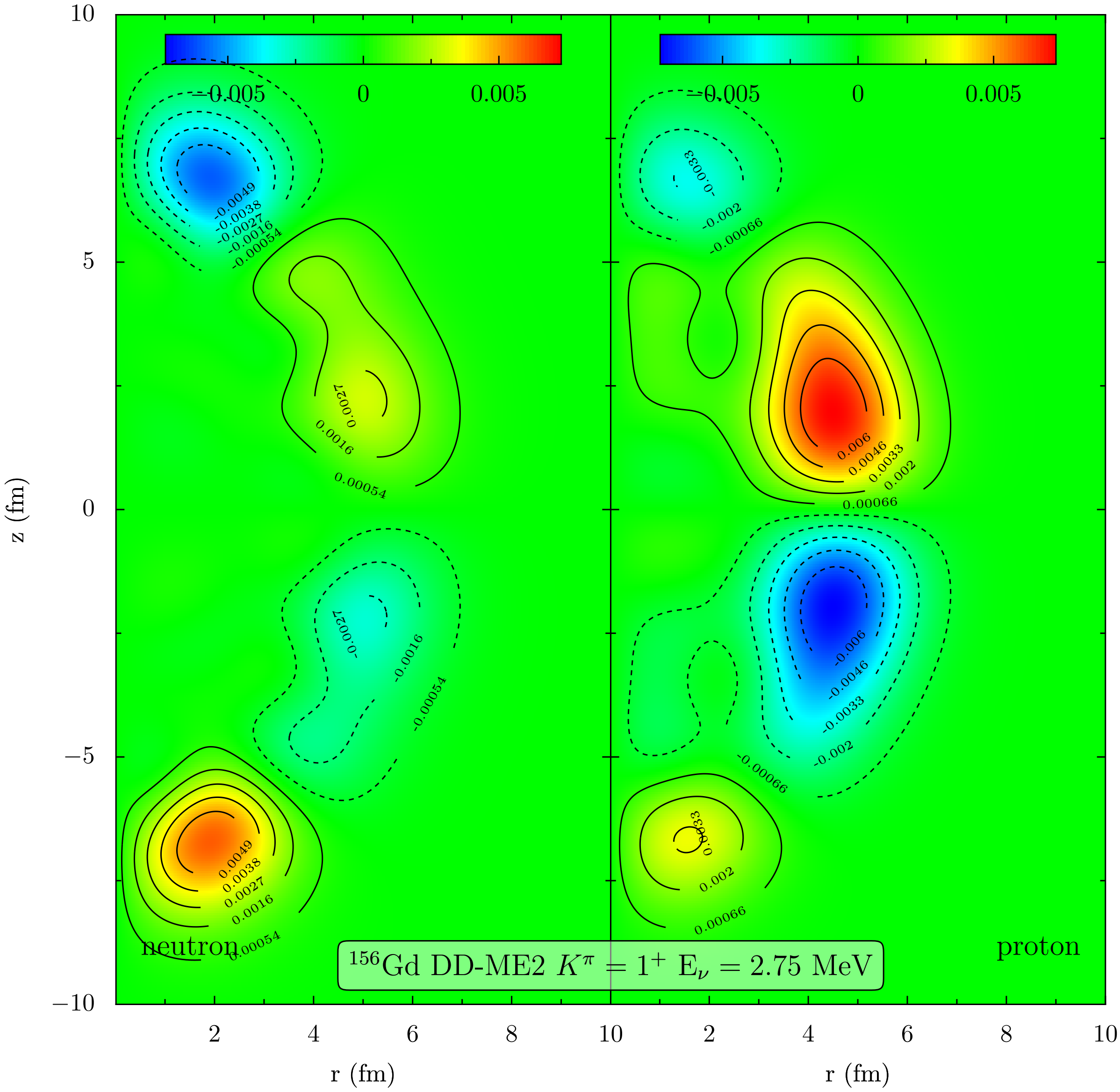

Figure 6.6: ^{156}Gd orbital mode at 2.75 MeV transition density for the DD-ME2 parameter set. It is almost identical to the one obtained with the NL3 parameter set (see Fig. 6.5).

for the neutron transition density, protons tend to share the same phase, but with a considerably different absolute value. It is evident from the plots that the greater transition probability occurs at the outer edges of the nucleus, near the surface. The core stays relatively unperturbed. It is very clear, however, that it does not correspond to the scissors mode excitation pattern; there is almost no isovector component, and certainly the protons do not rotate against the neutrons. We must therefore conclude that this is another kind of collective mode, maybe the isoscalar counterpart to the scissors mode. In particular, the detailed study of the intrinsic transition densities seem to suggest a skin mode. Unlike the case of the scissors mode, the isospin of this

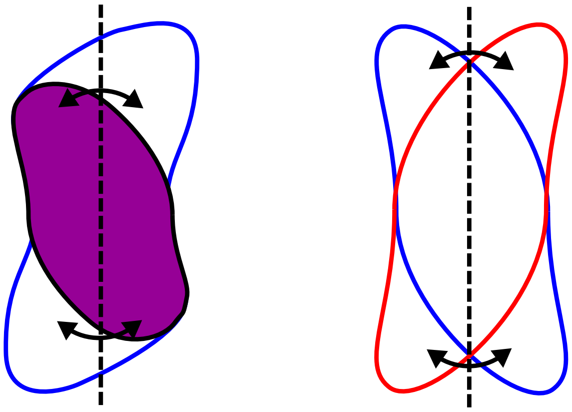

Figure 6.7: Schematic drawing of the two low-lying orbital modes. The left-hand side corresponds to the low lying skin mode. On the right is the typically scissors-like motion, which corresponds to the higher lying peak with strong orbital character.

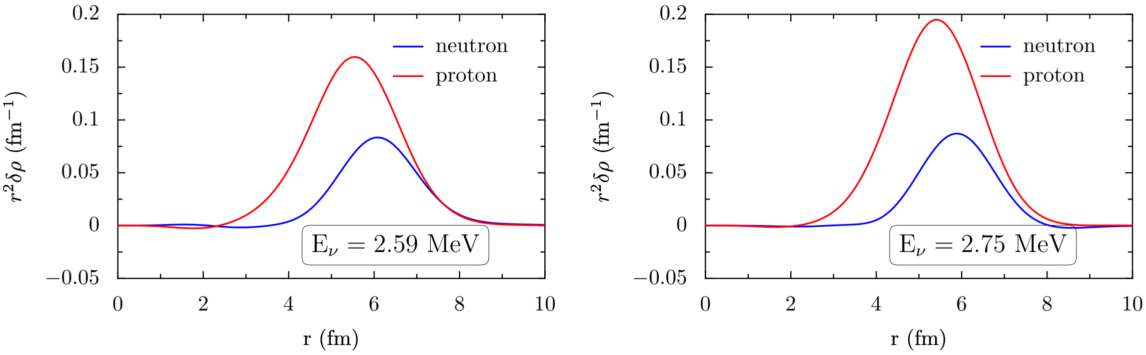

Figure 6.8: Radial dependence of the projection to good angular momentum ($J = 1$) of the transition density in Figures 6.5 and 6.6.

excitation mode is not well defined. While near a perpendicular to the symmetry axis (r-axis) neutrons and protons are in phase and have a comparable transition density, at the far end of the nuclear surface along the symmetry axis the neutron transition density is three times as big as the proton one. It is thus the case that in the central surface region this mode is an isoscalar ($T = 0$) mode, while at the caps there is an admixture of $T = 0$ and $T = 1$. The schematic representation on the left of Figure 6.7 portrays such a situation. The shaded region represents the nuclear core composed of neutrons and protons rotating in phase. The full blue line represents the extended neutron skin at the cap, which rotates out of phase against the core.

It can perhaps be seen more easily looking at the radial components of the projected transition densities. Figure 6.8 confirm many of the first impressions one receives from the two dimensional plots. Up to 4 fm the densities are essentially zero, i.e. there is practically no contribution coming from the core. It can also be gathered from the plot that this precise mode has a very high isoscalar nature, neutrons and protons are in phase. The proton maximum is twice the magnitude of that of neutrons, and is located 1 fm closer to the origin. Many of the fine-grained details that can be seen in the intrinsic transition density plots are lost because of the smearing caused by the projection to good angular momentum; however, comparing with the typical projected transition density of the scissors mode (see Figure 6.9)

Thus, the simple geometrical picture portrayed by the TRM does not reflect the results obtained in the present self-consistent investigation for the lowest lying orbital M1 excitation peak. However, this is not the only one with a large orbital component, even if it is in the only energy region where the orbital contribution dominates the response. As can be seen in Fig. 6.4, around 4 MeV, 5.5 MeV and 6.5 MeV, even if the spin response dominates, the transition strength has a non negligible orbital component. Whether this excitation modes have anything to do with what is known as the scissors mode, or their nature, is a difficult question that we will try to address in the following.

The intrinsic transition densities (both models) for the 3.8 MeV peak are shown in Figures 6.9 and 6.10. Below are also the projected densities for both parameters sets. At a first glance there is a stark contrast with those densities shown in Figure 6.8. It is evident that this mode has a very marked isovector nature, in contrast to the lower lying peak around 3 MeV. Roles are reversed concerning the neutron an proton densities. While the proton contribution is stronger near the center, the neutron density is larger further away from the origin.

Differences between the two functionals used in the calculations are also evident. In Figure 6.4 it can be seen that, while for the NL3 calculation the peak at 3.87 MeV is dominantly of orbital nature, the same does not happen for DD-ME2. In the later case the excitation peak is dominated by the spin part of the M1 operator. The excitation pattern for the NL3 peak can be connected with the classical scissors mode description easily: the neutron and protons rotate against each other around a perpendicular of the symmetry axis. However, the same cannot be said about the peak for the DD-ME2 parameter set, where even if the protons rotate against neutrons, they do it at different distances from the origin. It can be regarded as a couple of onion shells that rotate in different directions. Thus, the spin-flip contribution to the mode smears its neutron-proton rotational character.

It is very interesting to compare the single particle structure of this mode around 3.5-4 MeV with that at 2.5-3 MeV. Table 6.3 shows that in fact the same structure of transitions where the $\Delta n_z = -1$ and $\Delta\Lambda = 1$ trait is present. Again, the largest spin-flip contribution is under 1% share of the total strength. Even though the transition

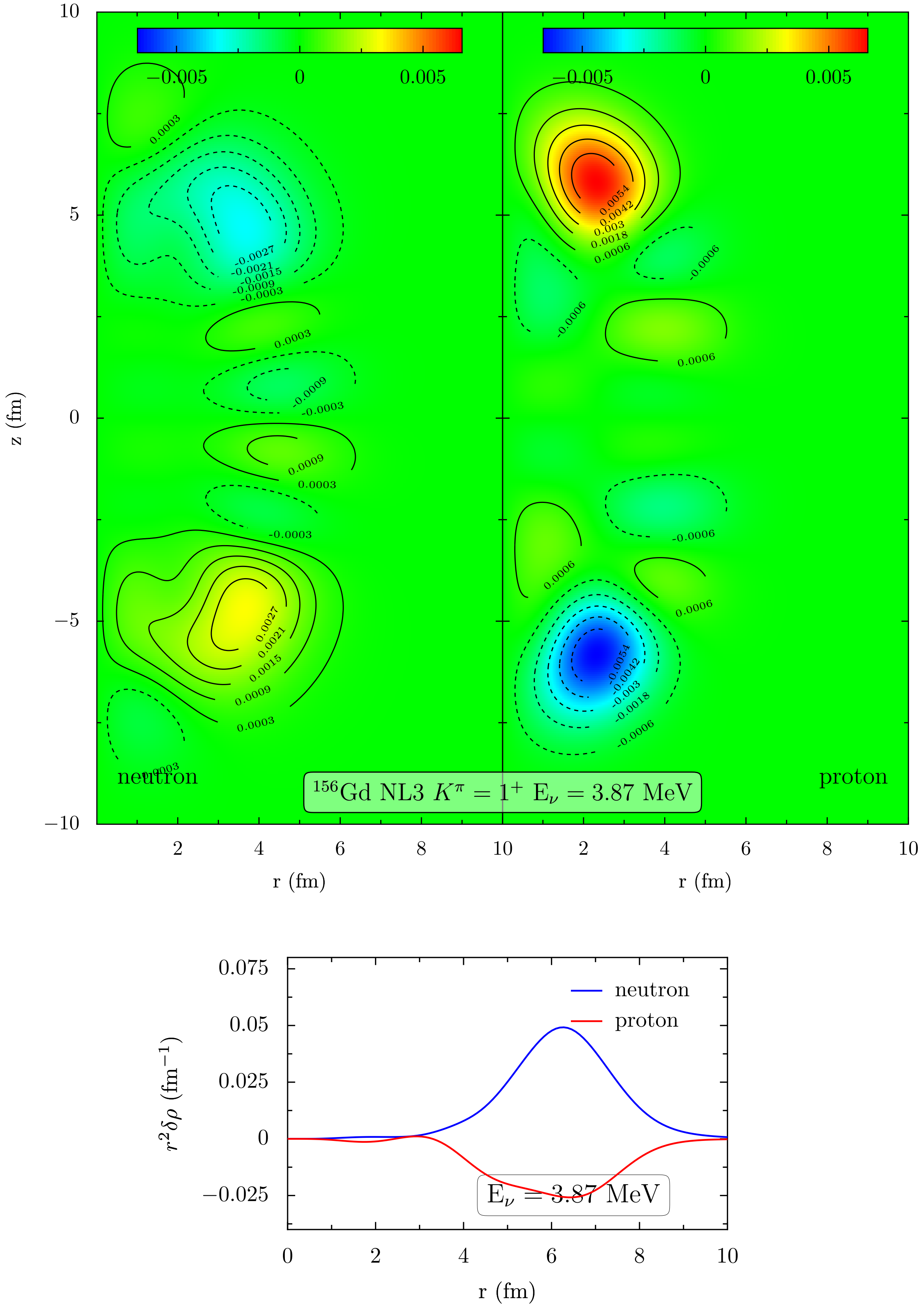

Figure 6.9: ^{156}Gd transition density for the peak with strong orbital component at 3.87 MeV for the NL3 parameter set.

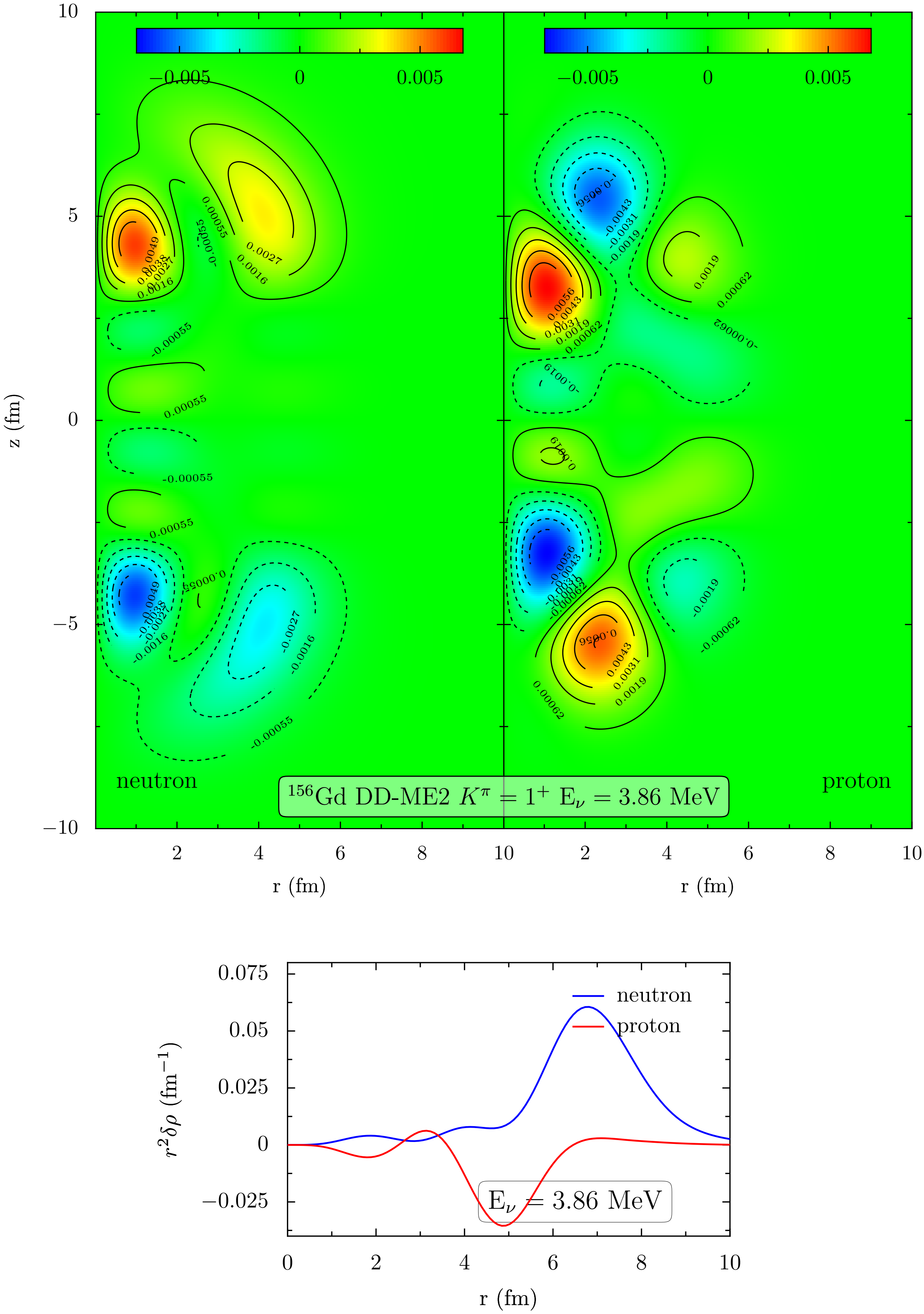

Figure 6.10: ^{156}Gd transition density for the peak with strong orbital component at 3.86 MeV for the DD-ME2 parameter set.

NL3 parameter set, M1 in ^{156}Gd

3.87 MeV				ΔE (MeV)
	proton	73%	$-\frac{3}{2}^-([541]\,78\%) \rightarrow +\frac{5}{2}^-([532]\,87\%)$	3.91
	neutron	15%	$-\frac{3}{2}^-([532]\,84\%) \rightarrow +\frac{5}{2}^-([523]\,90\%)$	3.79
	neutron	4%	$-\frac{1}{2}^-([530]\,74\%) \rightarrow +\frac{3}{2}^-([521]\,84\%)$	3.67
	neutron	2%	$-\frac{3}{2}^+([651]\,72\%) \rightarrow +\frac{5}{2}^+([642]\,82\%)$	2.66
	neutron	2%	$+\frac{3}{2}^-([530]\,74\%) \rightarrow +\frac{5}{2}^-([521]\,84\%)$	4.59

DD-ME2 parameter set, M1 in ^{156}Gd

3.86 MeV				ΔE (MeV)
	proton	67%	$-\frac{3}{2}^-([541]\,78\%) \rightarrow +\frac{5}{2}^-([532]\,87\%)$	3.83
	neutron	10%	$-\frac{1}{2}^-([530]\,75\%) \rightarrow +\frac{3}{2}^-([521]\,85\%)$	4.12
	proton	6%	$-\frac{1}{2}^+([420]\,81\%) \rightarrow +\frac{3}{2}^-([411]\,89\%)$	4.52
	proton	4%	$-\frac{5}{2}^-([532]\,87\%) \rightarrow +\frac{3}{2}^-([523]\,92\%)$	3.46
	neutron	2%	$-\frac{1}{2}^+([400]\,93\%) \rightarrow +\frac{3}{2}^-([651]\,73\%)$	4.10

Table 6.3: *ph* structure of the peaks with large orbital contribution around 4 MeV in the M1 response for ^{156}Gd, for the NL3 and the DD-ME2 parameter sets.

densities in Figures 6.9 and 6.10 seem to suggest the contrary, in both functionals the main single particle component in this transition is the same, $-\frac{3}{2}^- \rightarrow +\frac{5}{2}^-$, with exactly the same oscillator quantum numbers. Thus, the two parameter sets predict the same structure and energy for this peak with a surprising degree of precision. Compared with the lowest lying orbital peak at ~ 2.5 MeV, both share the same excitation pattern of $\Delta n_z = -1$ and $\Delta\Lambda = 1$, which is not present in all the rest of the spectrum. Therefore, it is not totally illogical to speculate that both peaks belong to the same kind of rotational excitation. However, none of the two is obviously, or even unambiguously, connected with the classical scissors mode described by the Two Rotor Model, or the interpretation of all the available experimental results.

Regarding the high energy part of the spectrum, the general picture above 5 MeV is quite different. As already noted, the tendency in this region is for the orbital and spin M1 contributions to cancel each other, being the spin-flip the dominant excitation mechanism. In the lower lying region, up to 6 MeV the strength is very fragmented. The folded curve contains contributions from many different single particle configurations. However, in the region above 6 MeV, most of the strength for the different peaks comes from one RPA mode. Attending to the single particle structure of these excitations, it is very clear that they are mostly spin excitations, with $\Delta m_s = \pm 1$ and most of the time $\Lambda = 0$.

This fact has important consequences that become obvious looking at the projected transition densities for the main peaks in the region, in Fig. 6.11. Comparing with the lower lying peaks where the orbital part of the M1 operator plays a very important role, in these cases no general feature with simple geometrical interpretation can be extracted. It is, however, of interest to note that the two "bumps" that can be seen in the spectrum, one in the 5-6 MeV interval and the other in the energy region above, have markedly different excitation patterns. When the total response has non negligible contribution coming from the orbital part of the M1 operator the collectivity of the peaks increase almost to the levels observed in the lower lying peaks. However, when that does not happen, the strength is almost exclusively provided by a unique single particle transition with up to a 90% share.

A closer look reveals that the important orbital contribution in the 5-7 MeV region explains the seemingly collective and isoscalar nature of the spin excitations in that interval (six upper plots in Fig. 6.11). The two lower plots, however, indicate that in the energy interval 7-10 MeV the response is mostly due to single particle transitions between spin orbit partners. Inconclusive experimental results proposed an interpretation based on isoscalar excitations for the 5-7 MeV energy region, and isovector ones in the 7-10 MeV region. Our analysis cannot confirm those reports, even though it is true that the lower "bump" seems to correspond with isoscalar excitations with a somewhat high collectivity.

In summary, further study in other nuclei, from the same and others nuclear chart regions, is of course needed to draw general conclusions. However, from the results obtained in ^{156}Gd it has been found that the pairing strength plays a dominant role in the position of M1 excitations. When pairing correlations are absent, the single-particle energy gap is not so pronounced and the whole spectrum is shifted to lower energies. As one increases the pairing constants, the low lying response curve moves almost unaltered in shape to higher energies. When the gap is chosen to be the experimental one, the excitation at 3 MeV is not of orbital character, in disagreement with experimental results from reference [25].

Two major peaks with strong orbital character below 4 MeV excitation energy are found. We have tentatively labeled as the classical scissors mode the higher lying one at 3.8 MeV, which is 0.8 MeV off the experimental value. The orbital and spin contributions for this excitation mode are roughly the same. The simple picture of protons rotating against neutrons does not properly describe the results found, being the geometrical interpretation closer to a very specific kind of surface shear along a perpendicular of the symmetry axis (see the schematic Figure 6.7). The collectivity of the mode has been found to be rather low, with only a few single particle transitions contributing to the overall response. The integrated M1 strength for the scissors mode, however, predicts a low value of $2.6\,\mu_N^2$, almost $0.5\,\mu_N^2$ off the experimental value. In

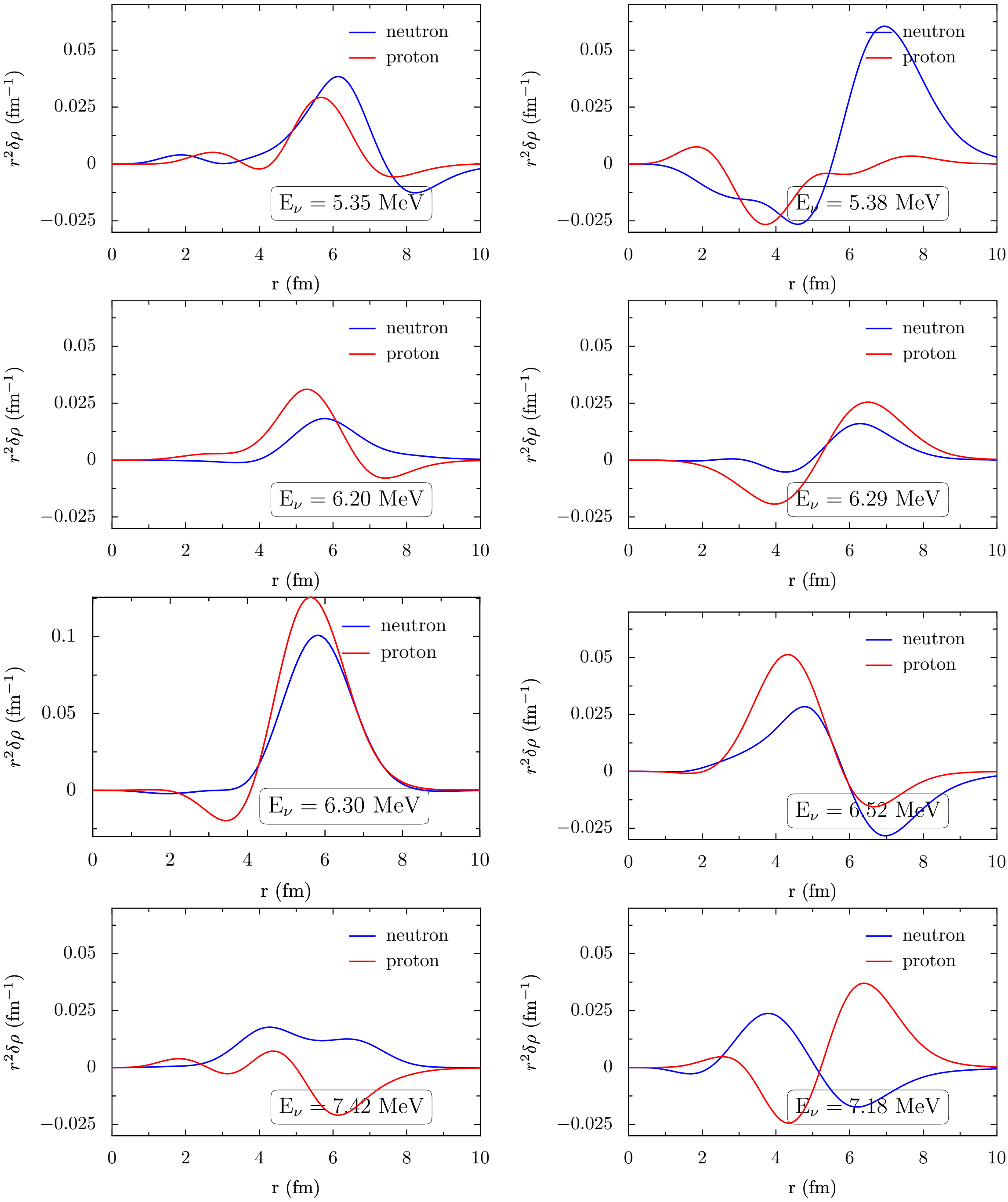

Figure 6.11: M1 projected transition densities for the spin excitations in the energy interval 5-12 MeV in ^{156}Gd. NL3 left, DD-ME2 right.

addition, another strong orbital peak is found around 2.5-3 MeV, which shares the same excitation pattern as the scissors mode and is of isoscalar nature. Its geometrical interpretation is, however, not clear, as it is a surface excitation where a skin of neutrons rotates against a core composed of neutrons and protons, and can be the rotational equivalent of the pygmy dipole resonance in the magnetic case. The similarities with the classical scissors mode, in particular the identical single particle excitation pattern, is a strong hint that they belong to the same kind of rotational collective excitation.

Regarding the structure of the high lying response in the 5-10 MeV energy region, two main zones can be identified attending to whether the orbital and spin response add up or cancel to form the total M1 response, as was already noted when studying ^{20}Ne. Between 5 MeV and 7 MeV there is non negligible orbital response, while it disappears from the response at higher energies. The almost isoscalar nature of the lower peaks contrast to the almost pure single particle structure of the high lying ones. They correspond to the experimentally well known “bumps” in the spin-flip part of the M1 spectrum.

Attending to their configuration, both show a radically different single particle structure compared with the tentatively identified scissors mode peaks at 3 MeV and 4 MeV. Comparisons of these results with calculations we have performed in other gadolinium isotopes, demonstrate that this particular region of the response is very fragmented and highly dependent on the nucleus under consideration. The exact position of the peaks is also very sensitive to the strength of pairing constants used in the calculations, showing a much cleaner spectrum when no pairing force is present. However, the general features remain grossly the same, without much variation in the configuration that composes the different excitation states.

In summary, we feel that the overall experimentally observed features of the M1 response in ^{156}Gd are well reproduced within the present relativistic functionals. However, a detailed systematic study of such excitations in isotopic chains in the actinide and other regions should cast light into the reasons behind the quantitative divergences observed with some of the experimental results, and clarify the true nature of the scissors mode and the soft skin mode our calculations predict at low energies.

Chapter 7

E1 transitions in deformed nuclei

"It doesn't matter how beautiful your theory is, it doesn't matter how smart you are. If it doesn't agree with experiment, it's wrong."
— Richard P. Feynman, 1918-1988

7.1 E1 response in Ne isotopes

In recent years, the study of the low lying collective soft modes has been a very attractive subject, both experimentally and theoretically. They correspond to the oscillation of the mantle composed from excess neutrons out of phase against a core formed from the rest of the neutrons and protons. The structure of such modes is deeply linked with the single particle structure near the Fermi surface, and thus its study can provide valuable information regarding the performance of the different functionals. Originally thought to be an exclusive phenomenon of heavy nuclei with large isospin asymmetries, a very similar excitation pattern has also been observed in light nuclei. The first systematic experimental effort in light nuclei, based on electromagnetic excitations in heavy-ion collisions, indicated the appearance of low-lying dipole strength in oxygen isotopes ^{17}O-^{22}O [11, 152]. It has been also throughly investigated within a variety of theoretical tools [123, 40, 151], including the RHB+RQRPA in spherical symmetry [108, 110, 163, 109], with different degrees of success in comparison with experimental data.

Recent experiments [55] performed in ^{26}Ne show an enhancement of the isovector dipole response in the low lying region; tentatively, it has been identified as a possible pygmy mode. We present a systematic study in the RHB+RQRPA framework of the dipole response in the Ne isotopic chain, from ^{20}Ne to ^{28}Ne, using two different relativistic density functionals, the veteran NL3 and the more recent DD-ME2. New IVGDR features arising from the explicit use of a deformed formalism will be given consideration. In particular, it is of interest to establish the evolution of the low lying E1 excitation strength with increasing number of neutrons and the question of the existence and properties of pygmy modes in deformed light nuclei.

In Figure 7.1 the evolution of the E1 dipole response in neon isotopes with increasing number of neutrons, from ^{20}Ne to ^{28}Ne is plotted. On the left are the excitation strengths for the NLME functional with the NL3 parameter set, and on the right those for the DDME functional with the DD-ME2 parameter set. The red curve corresponds to excitations along the symmetry axis with $K^{\pi} = 0^{-}$, while the blue curve are those perpendicular to the symmetry axis with $K^{\pi} = 1^{-}$. In principle, for prolate nuclei, as is the case for the studied neon isotopes, the strength due to the $K^{\pi} = 0^{-}$ mode should lie at lower energies compared to the $K^{\pi} = 1^{-}$ mode. An intuitive argument that accounts for that fact is to remember that the nuclear potential must be flatter (more extended) along the symmetry axis, and thus it is more favorable energetically for the nucleons to oscillate in that direction than perpendicular to the symmetry axis, where the nuclear potential is narrower. It is possible, therefore, to relate the nuclear deformation with the energy separation of the two modes. In the numerical chapter it has been checked that for spherical nuclei peaks for both excitation modes appear at the same energies.

The splitting of the response due to the broken spherical symmetry, and its interpretation, can be observed in Figures 7.2 and 7.3. The upper plot is the transition density for the main IVGDR peak at 16.73 MeV observed in the $K^{\pi} = 0^{-}$ response in ^{20}Ne for NL3. The other corresponds to the peak at 21.31 MeV in the $K^{\pi} = 1^{-}$ mode. The prolate deformation is evident, as the densities are elongated in the direction of the z-axis. The character of the $K^{\pi} = 1^{-}$ mode as a vibration along a perpendicular of the symmetry axis is recognizable in Figure 7.3. By comparison, in Figure 7.2 is then easily interpreted as a vibration along the symmetry axis. Warm colors (red) indicate positive values, while cold colors (blue) represent negative values. As expected for the IVGDR, the neutron-proton vibrations are out of phase over the same spatial regions. It is more evident still looking at their respective projections to the laboratory system of reference, which are shown in the lower plots. In general, the transition densities for the absolute value for the $K^{\pi} = 1^{-}$ mode are always larger than that of the $K^{\pi} = 0^{-}$ mode.

Coming back to Figure 7.1, the response in the energy region between 15 MeV and

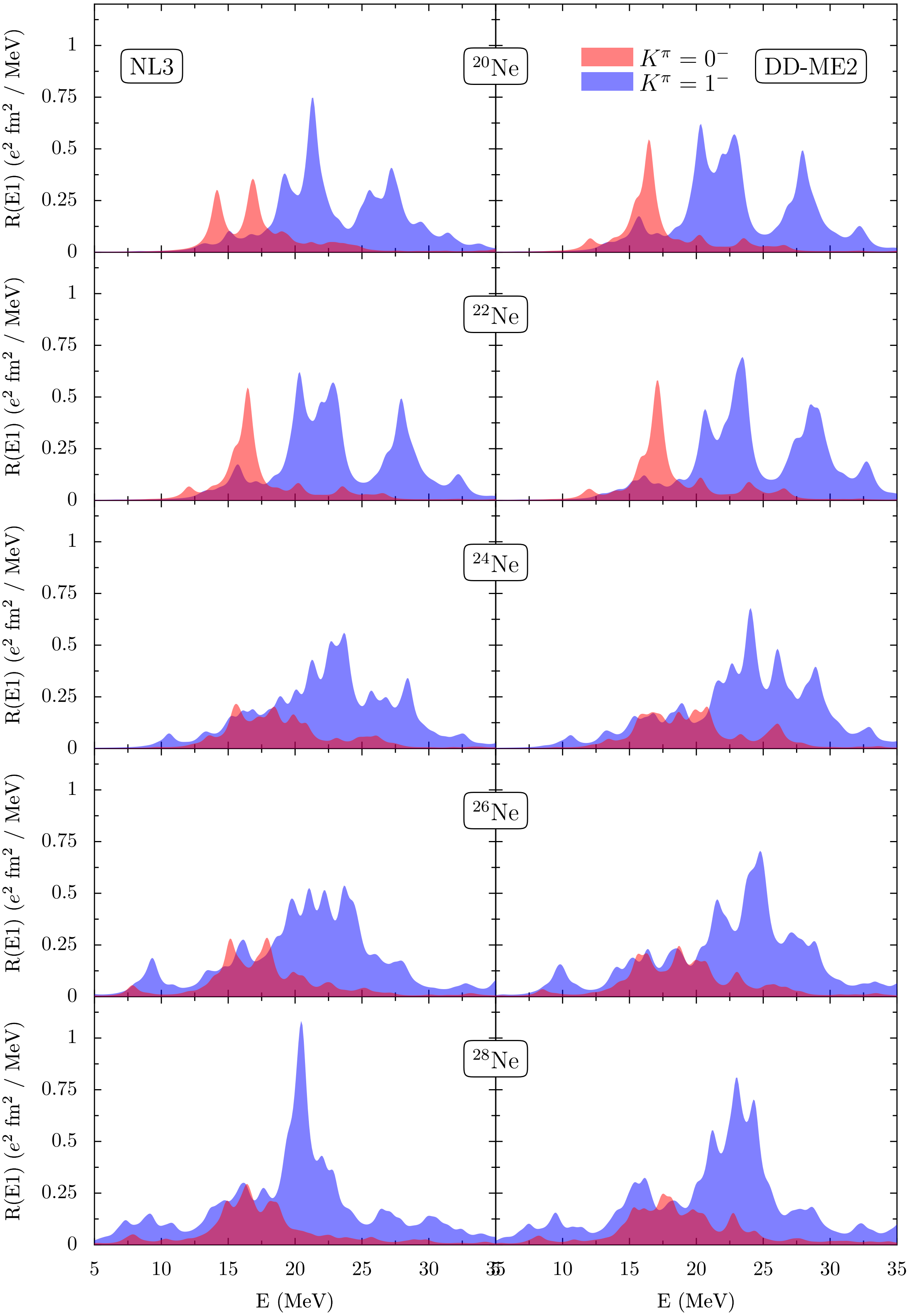

Figure 7.1: Evolution of the E1 excitation strength from ^{20}Ne to ^{28}Ne for two different relativistic functionals.

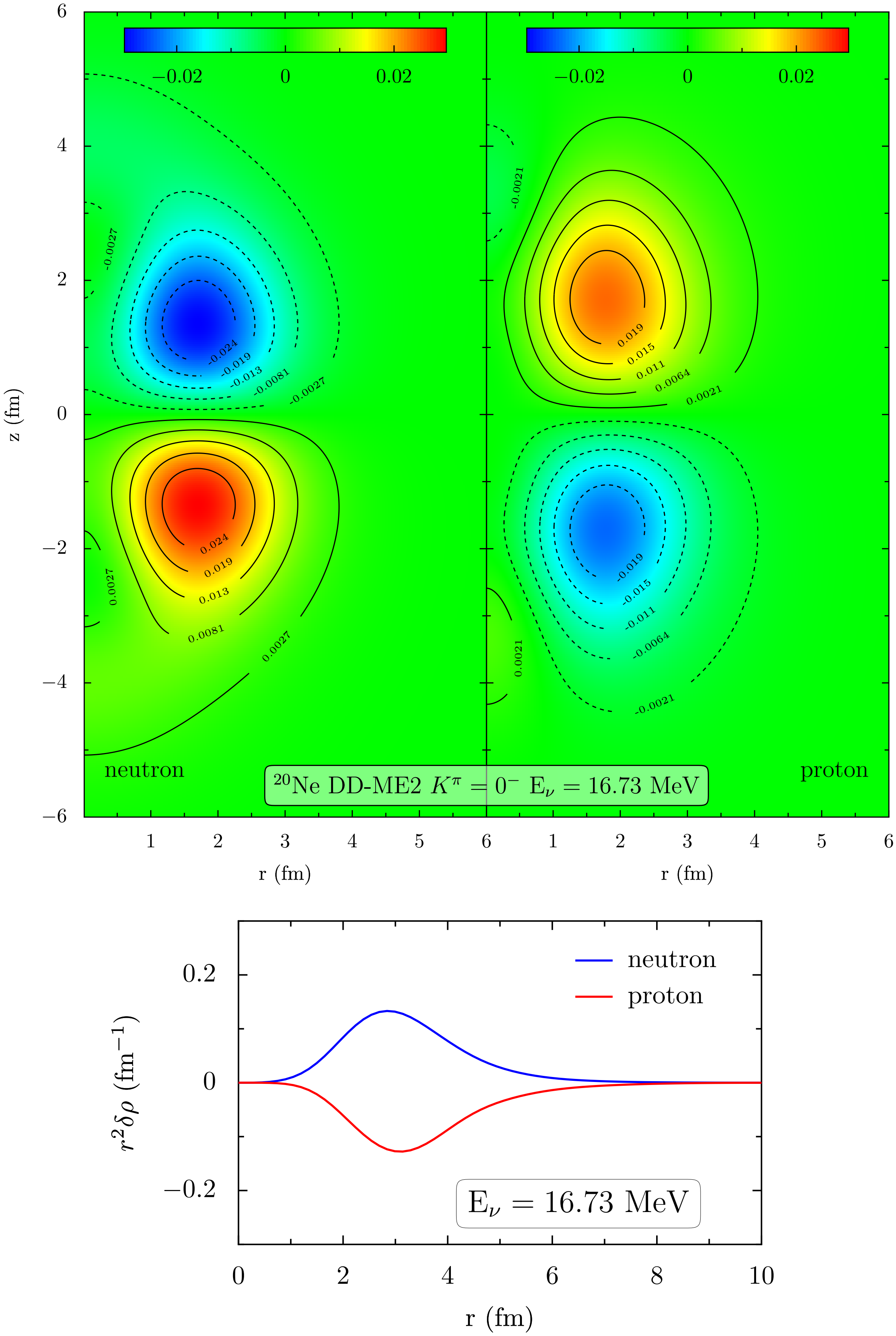

Figure 7.2: ^{20}Ne IVGDR transition density for the $K^{\pi} = 0^{-}$ peak at 16.7 MeV, NL3 parameter set.

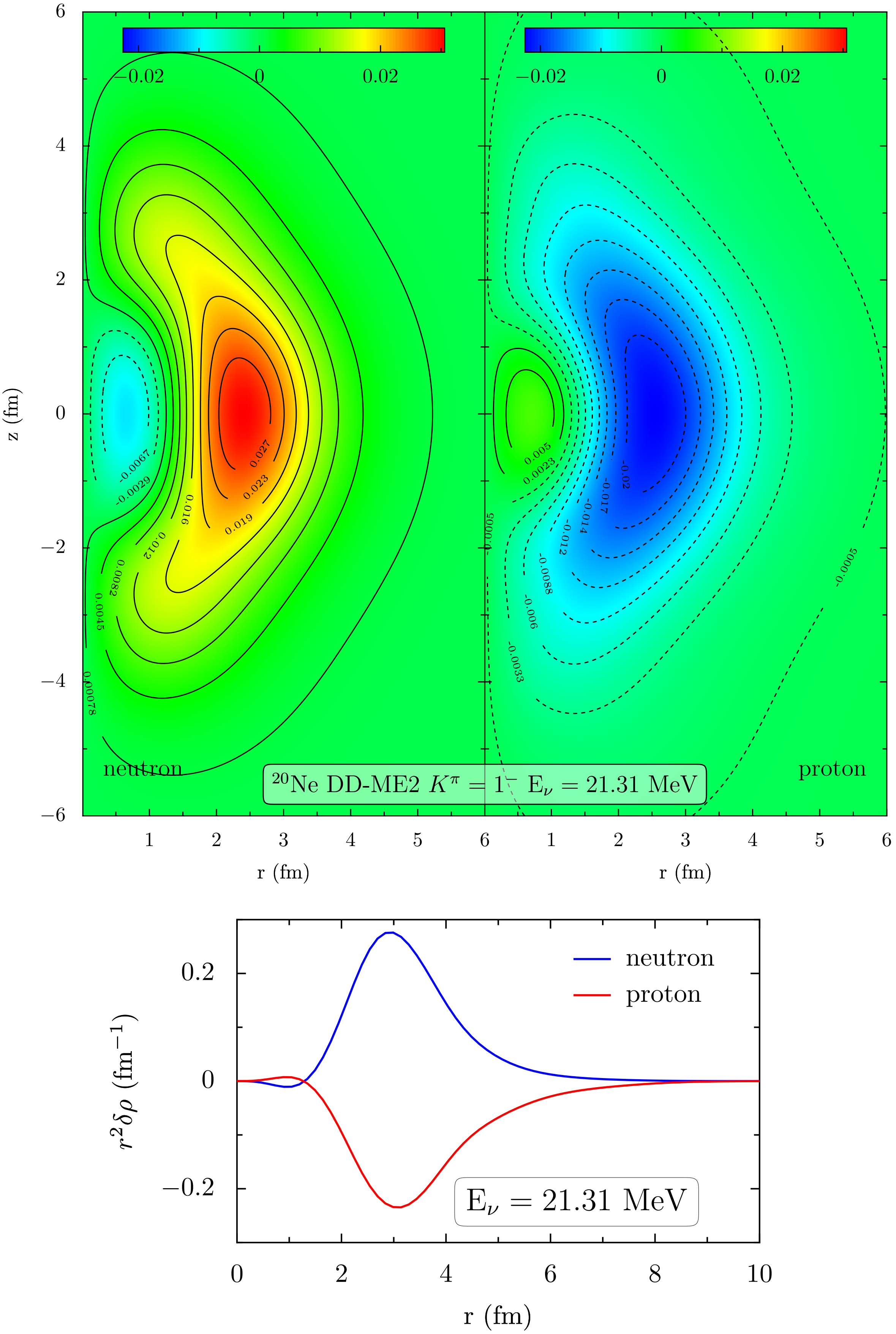

Figure 7.3: ^{20}Ne IVGDR transition density for the $K^\pi = 1^-$ peak at 21.3 MeV, NL3 parameter set.

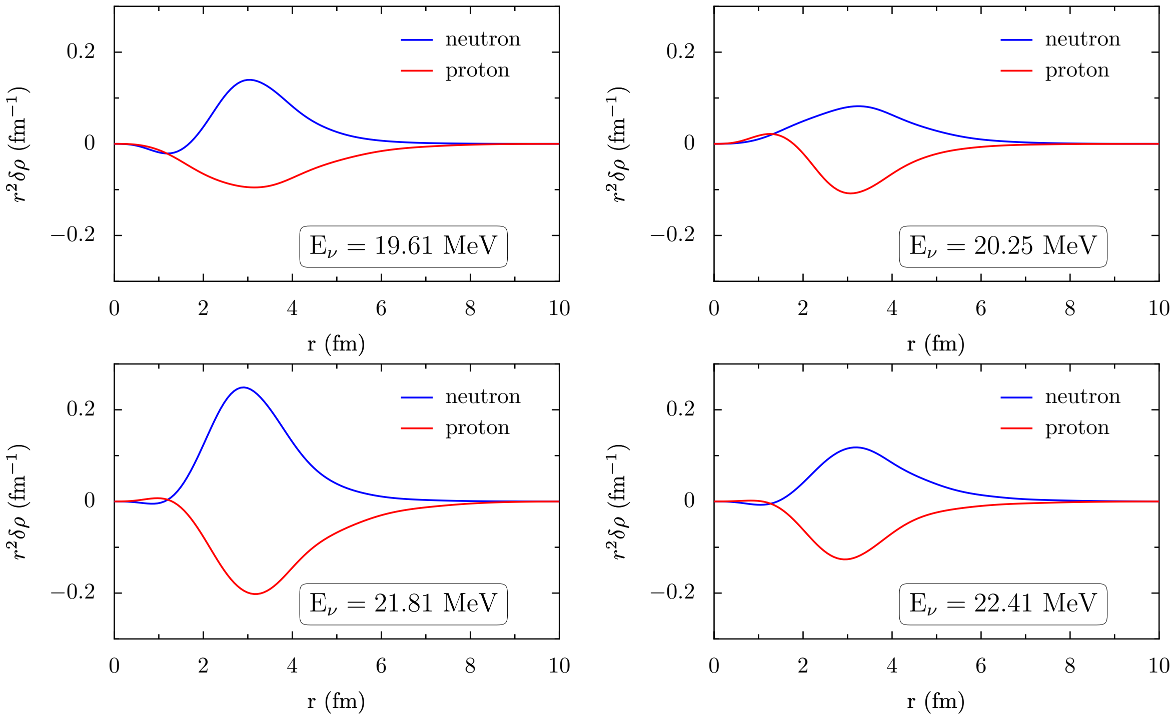

Figure 7.4: Projected transition densities for the main contributing peaks in the dipole response in ^{20}Ne, as calculated with the DD-ME2 parameter set.

25 MeV corresponds to the IVGDR. Its strength is heavily fragmented in several peaks in an energy interval of about 3-4 MeV for both excitation modes. The main contributions to the strength curve (arbitrarily defined as more than 25% of the maximum) come from at least four different peaks. For example, in ^{20}Ne for the $K^\pi = 1^-$ mode with the DD-ME2 parameter set the IVGDR is composed by four separate peaks, at 19.61, 20.25, 21.81, and 22.41 MeV respectively. The high collectivity of these peaks indicate a very coherent excitation pattern that fits into the properties of a giant resonance. Their projected transition densities, in Figure 7.4, show that all four peaks can be classified as a vibration of neutrons against protons.

Starting in ^{20}Ne, and as the number of neutrons increases, two main effects are observed: a) an increased fragmentation of the dipole strength, and b) the appearance of low lying strength below 10 MeV. These results are similar to those obtained for oxygen isotopes within the spherical RHB+RQRPA framework.

Even though the main motivation of the present investigation is the study of the low lying strength below 10 MeV, it is worthwhile to do a little detour and compare the results obtained for the GDR with the available experimental data, and to dig into the differences observed for the different functionals employed. The dependence of the position, width and strength of the GDR on the mass number and the deformation can all provide valuable information. In order to do just so, the discrete RPA spectra

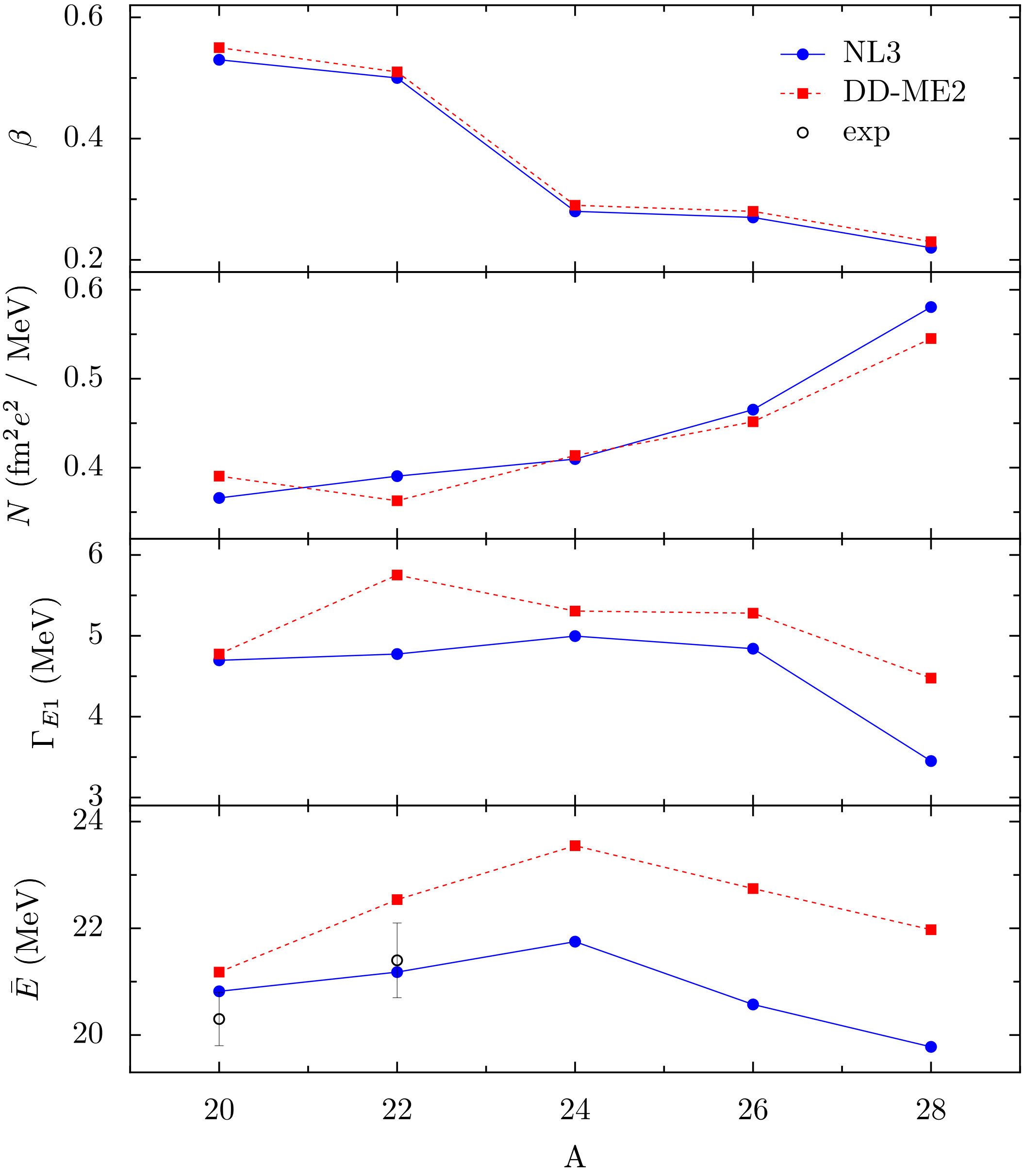

Figure 7.5: Top panel: evolution of the ground state quadrupole deformation versus the mass number. The three lower plots depict the change with the mass number of the Lorentzian parameters that describe the best Lorentz adjustment to the calculated response in Neon isotopes for two different parameter sets.

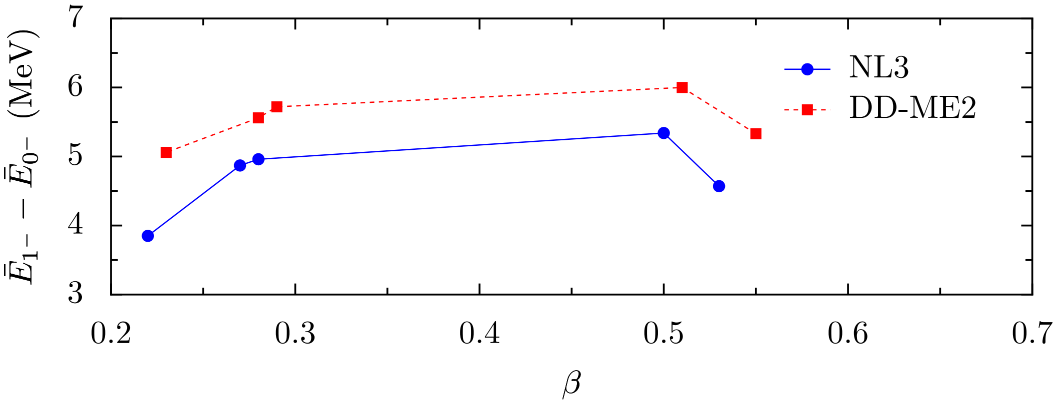

Figure 7.6: Difference between the positions of Lorentzian fits to the $K^\pi = 0^-$ and $K^\pi = 1^-$ main IVGDR peaks for two different parameter sets.

obtained from the deformed RHB+RQRPA calculations was adjusted to the Lorentzian function

$$R(E) = \frac{1}{2}\frac{N\Gamma}{(E-\bar{E})^2 - \Gamma^2/4} \tag{7.1}$$

in the energy interval 12.5-32.5 MeV by means of a non-linear least squares fit. The result is plotted versus the isotope mass number in Figure 7.5. As can be seen in the upper plot, both models predict the same deformation for all nuclei, and even though they are a little high for ^{20}Ne and ^{22}Ne, they agree well with the experimental values. The total Lorentzian height, N_{E1}, depicted in the second plot is fairly stable across the isotope chain. However, systematic differences between the models appear in the position of the IVGDR. While the results of both models predict a energy of 21 MeV for ^{20}Ne within a deviation of less than 0.3 MeV, that difference increases as one moves along the isotope chain up to 2 MeV for ^{28}Ne.

There is, however, the general trend of an increase in the position if the IVGDR up to ^{24}Ne where it is maximal, and then a decrease until ^{28}Ne, which is common to both parameter sets. The divergence in these results should be, in principle, due to the distinct isospin dependence encoded in the parameter sets used. As they are adjusted to properties of selected nuclei, almost always chosen to be in the valley of β-stability, it can be expected to find this kind of deviations. It would be very interesting to undertake a broad study of nuclear excitation properties to be able to constrain and improve the isospin dependence of such forces. However, such a study is out of the scope of the present investigation.

In Figure 7.6 is depicted the difference, in MeV, of the position of the main peaks $K^\pi = 0^-$ and $K^\pi = 1^-$ as a function of deformation. They were obtained through a least squares fit to a Lorentzian function. In principle, the splitting should be directly related to the nuclear deformation. However, for such light nuclei the single particle structure plays a dominant role, as can be gathered from the figure in conjunction with Figure 7.5. It is interesting to note that a systematic discrepancy between the two density functionals employed is clearly observed, with the DD-ME2 functional consistently predicting approximately 1 MeV more splitting than the NL3 functional throughout all isotopes. The greater dispersion in the response for the IVGDR that can be seen in Figure 7.5 for the DD-ME2 parameter set is directly related with the energy splitting between the two excitation modes. This broadening of the GDR with deformation is even more evident when studying heavier nuclei.

In the present investigation of the Neon isotopes, we also analyse the structure of the main peaks in the low energy region for the isovector dipole strength distribution. In particular, we will focus our attention on properties in ^{26}Ne, where recent experimental results [55] indicate the presence of a non negligible response in the 8-12 MeV energy region. Neutron contributions to the isovector dipole strength in ^{26}Ne dominate in the low energy region. The strength function below 12 MeV is fragmented into several different peaks, with major contributions at 7 MeV and 9 MeV for $K^\pi = 1^-$ and $K^\pi = 0^-$ transitions, respectively.

In contrast to the well known radial dependence of the IVGDR transition densities (proton and neutron oscillate with opposite phases), the proton and neutron transition densities are mostly in phase in the nuclear interior. Furthermore, there is almost no contribution from the protons in the surface region. The strong neutron transition density displays a long tail in the radial coordinate. The different radial dependence of the transition densities that correspond to the soft low-energy states as compared to those of the giant resonances are due to the contribution of the loosely bound excess neutrons. Studies in light neutron halo nuclei [137] have shown that these soft modes in light nuclei, which result from the large spatial extension of the bound single particle states, represent a new type of non-resonant independent single particle excitations. The narrow width and the large transition strength, which characterize these excitations, are not caused by a coherent superposition of *ph* configurations as in collective states.

In our calculations in ^{26}Ne, the isovector dipole response in the low energy region below 12 MeV is mainly characterized by unique neutron single particle transitions, with minor contributions from additional configurations. This fact is in sharp contrast to the coherent superposition of many *ph* configurations that characterizes the excitation in the region of classical collective modes, i.e. the giant resonances. Although the inclusion of pairing correlations increases the collectivity of the low lying states, its main effect is that of shifting the response to higher energies and fragmenting the isovector dipole response into several peaks with dominant single $2qph$ configurations. The situation slightly differs from that found in other relativistic investigations [163] in oxygen isotopes, where an increase in the response strength was also observed.

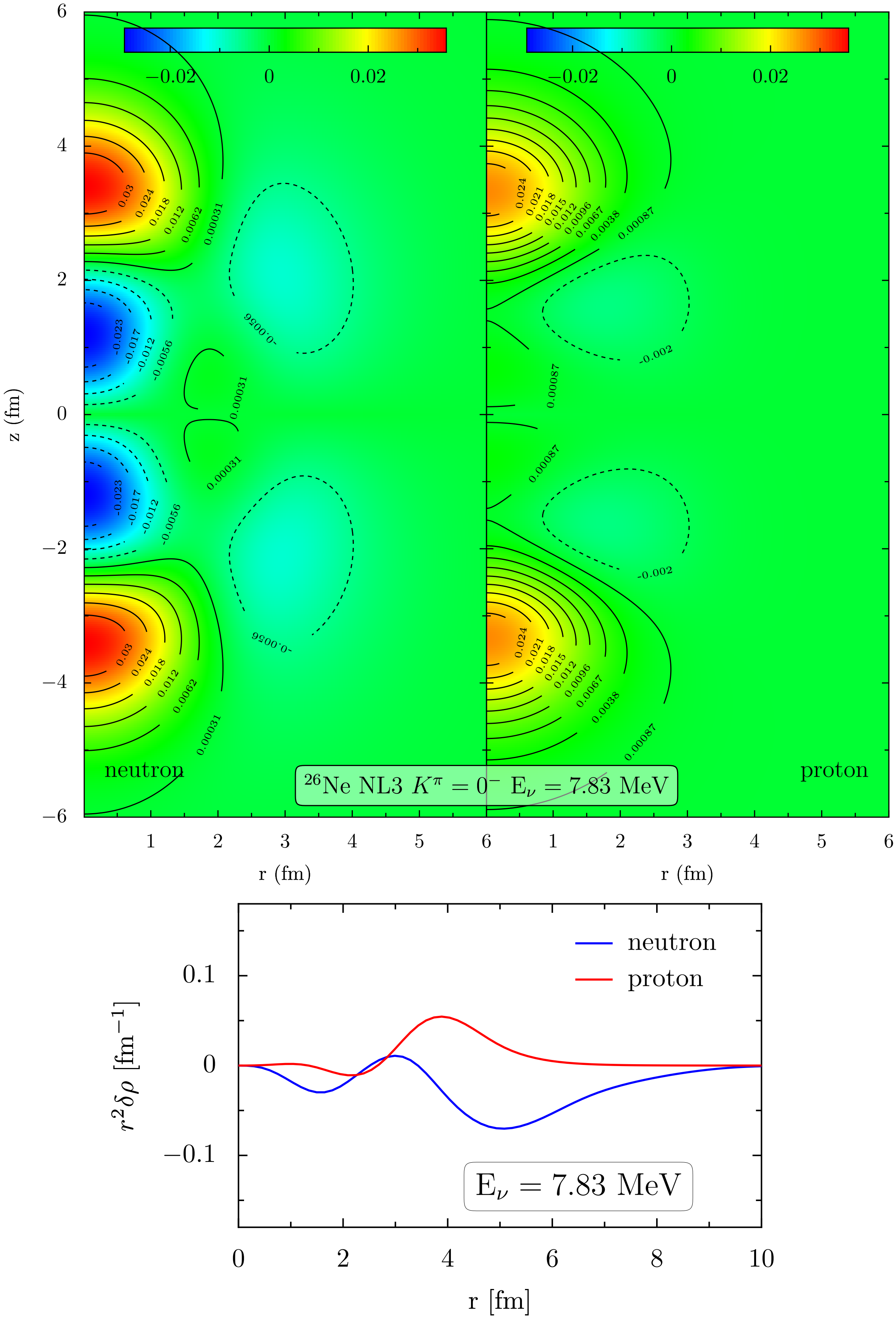

Figure 7.7: Transition densities for the low lying peaks in the E1 response of ^{26}Ne, calculated with the NL3 parameter set.

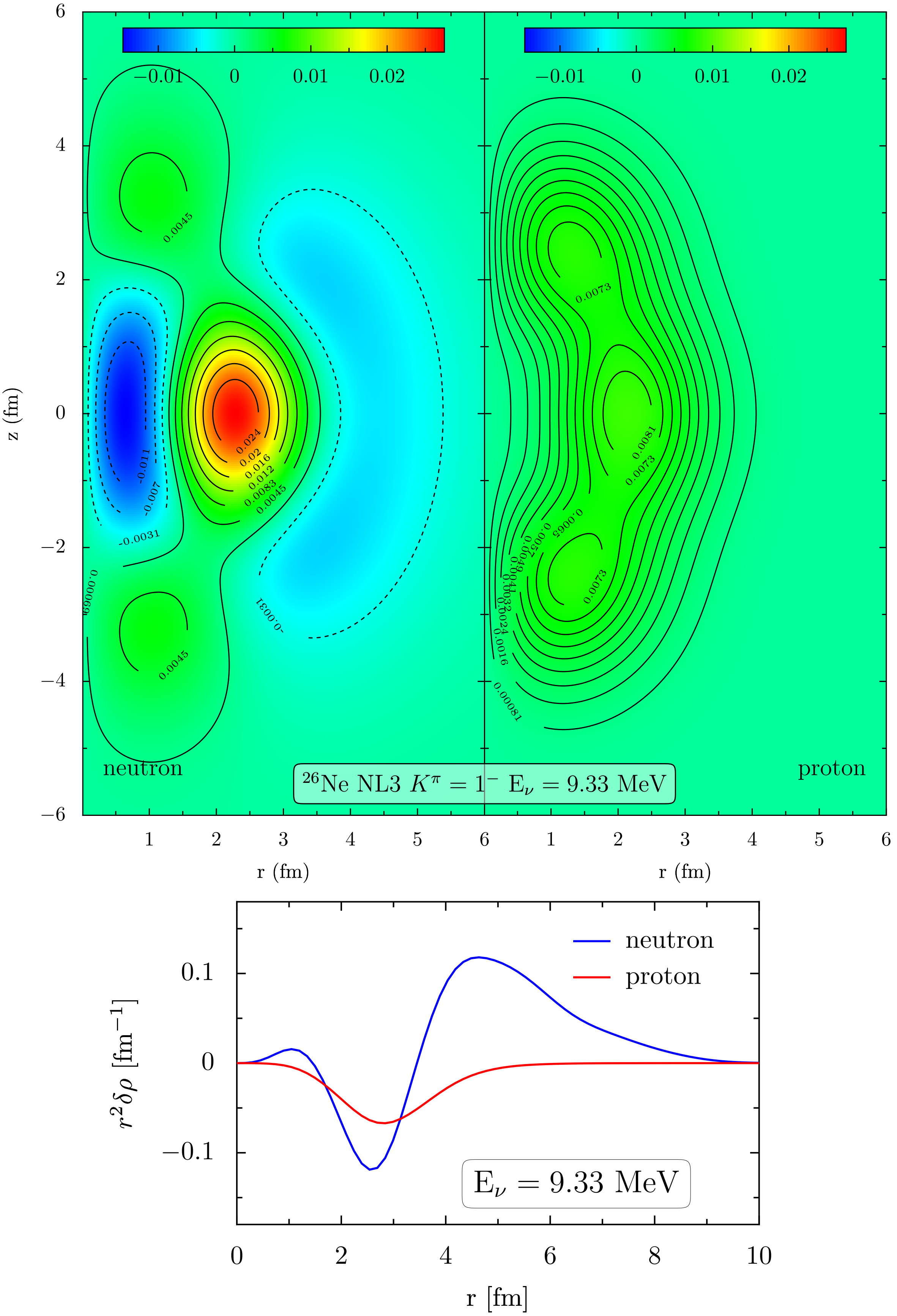

Figure 7.8: Transition densities for the low lying peaks in the E1 response of ^{26}Ne, calculated with the NL3 parameter set.

^{26}Ne $K^\pi = 0^-$ peak at 7.8 MeV, NL3 parameter set			ΔE
neutron	70%	$-\frac{1}{2}^+([211]\,61\%) \to +\frac{1}{2}^-([310]58\%)$	8.5
neutron	9%	$-\frac{1}{2}^+([220]\,88\%) \to +\frac{1}{2}^-([330]82\%)$	12.9
proton	7%	$-\frac{1}{2}^+([220]\,85\%) \to +\frac{1}{2}^-([330]81\%)$	14.4
neutron	2%	$-\frac{1}{2}^+([211]\,61\%) \to +\frac{1}{2}^-([330]82\%)$	5.5
neutron	2%	$-\frac{1}{2}^+([211]\,61\%) \to +\frac{1}{2}^-([301]54\%)$	9.3

^{26}Ne $K^\pi = 1^-$ peak at 9.33 MeV, NL3 parameter set			ΔE
neutron	44%	$-\frac{1}{2}^+([211]\,61\%) \to +\frac{3}{2}^-([301]65\%)$	9.3
neutron	38%	$+\frac{5}{2}^+([202]\,97\%) \to -\frac{3}{2}^-([321]83\%)$	9.5
neutron	8%	$+\frac{1}{2}^+([211]\,61\%) \to +\frac{1}{2}^-([301]54\%)$	9.3
neutron	1%	$-\frac{3}{2}^+([211]\,94\%) \to +\frac{5}{2}^-([312]86\%)$	14.4

Table 7.1: *ph* structure for the 7.8 MeV and 9.3 MeV peaks in ^{26}Ne for the NL3 parameter sets, respectively.

Figures 7.7 and 7.8 show the intrinsic and projected transition densities, for ^{26}Ne, of the main peaks found for the $K^\pi = 0^-$ and $K^\pi = 1^-$ excitation modes in the low energy region, at 7.83 MeV and 9.33 MeV respectively. The transition density for the 7.8 MeV peak is a mixture between the classical isovector dipole and the pygmy dipole resonances. The same can be said of the transition density for the peak at 9.3 MeV, even though it shows a much more developed pygmy character, with protons and neutrons in-phase in the nuclear core, and a skin predominantly composed of neutrons.

The decomposition into single particle transitions of these two peaks can be seen in Table 7.1. The contribution C_{qph} from a particular proton or neutron *qph* configuration to a RPA state is determined by

$$C_{qph} = (|\mathcal{X}^\nu_{ph}|^2 - |\mathcal{Y}^\nu_{ph}|^2)\eta^-_{ph} \tag{7.2}$$

where the occupation factor η^- is defined in Equation (4.19). $\mathcal{X}^\nu$ and $\mathcal{Y}^\nu$ are the RQRPA amplitudes associated to a particular RQRPA excitation energy. With a major contribution of 70% of the total coming from one configuration, it is evident that the lower lying peak at 7.8 MeV is mostly a single particle transition. The excitation at 9.3 MeV has important contributions coming from two different single particle transitions. Consequently, it cannot be said that these excitations have a very collective nature. However, it has to be taken into account that we are treating with very light nuclei, and that the number of possible configurations that can reasonably contribute to such low lying excitations is not very high.

Already mentioned, a recent experiment [55] has studied at RIKEN the elastic and inelastic scattering of ^{26}Ne on ^{nat}Pb and ^{27}Al target. It was found that the excitation energy spectrum between the one neutron and the two neutron emission thresholds exhibits a strong E1 strength. The measured reduced transition probability in the energy interval 8-10 MeV is $B(E1, \uparrow) = 0.544 \pm 0.183\mathrm{e}^2\mathrm{fm}^2$. The fraction of the classical Thomas-Reiche-Kuhn energy weighted sum rule exhausted by the mode is of 5.2%±2.1%. The theoretical value obtained in our calculations is 3.5%, which is inside the experimental error margin. However, other theoretical studies [76] carried out in spherical symmetry show better agreement, in that respect, with the experimental results. Concerning the position of the main enhancement in the E1 response, in this experiment it was found at 9 MeV. This value is in very good agreement with the result obtained in the present investigation, which is only 0.3 MeV off the experimental value, and much closer than the already cited theoretical study in spherical symmetry. Regrettably, no data could be extracted from measurements around 7 MeV, as it is too close to the neutron threshold to draw reliable conclusions. Thus, the peak that our calculations predict at 7.8 MeV cannot be confirmed by these experimental results.

7.2 Low lying E1 response in ^{100}Mo

The dipole strength close to separation energies in several Mo isotopes was measured in a recent experiment [134]. We shall concentrate in ^{100}Mo, as it was the only deformed nucleus which was studied. In that experiment it was found that there is a modest enhancement of the response in the low lying energy region. It has been tentatively linked to the Pygmy Dipole Resonance. The extracted dipole functions combine smoothly with those previously reported in studies of the Giant Dipole Resonance [14], obtained from photoneutron absorption reactions. In this section we apply the RHB+RQRPA framework for deformed nuclei to the study of the response of the E1 operator in ^{100}Mo, in particular the low lying dipole strength and its structure.

The ground state properties of ^{100}Mo, as calculated with the NL3 and DD-ME2 parameter sets, predict a binding energy of 8.5 MeV per particle. The pairing constants were adjusted to reproduce the experimental gaps of $\Delta_n = 0.9$ MeV and $\Delta_p = 1$ MeV. The deformation obtained with this parameters is of $\beta = 0.3$, with prolate shape.

In Figure 7.9 we display the RHB+RQRPA dipole strength distribution in ^{100}Mo. The black data points with error bars correspond to the experimental results of references [14, 134]. The experimental centroid energy is situated at 18 MeV. The calculated positions of the theoretical centroid energies, taken over the same energy interval as the available experimental data, is 17.4 MeV for the NL3 parameter set, while for DD-

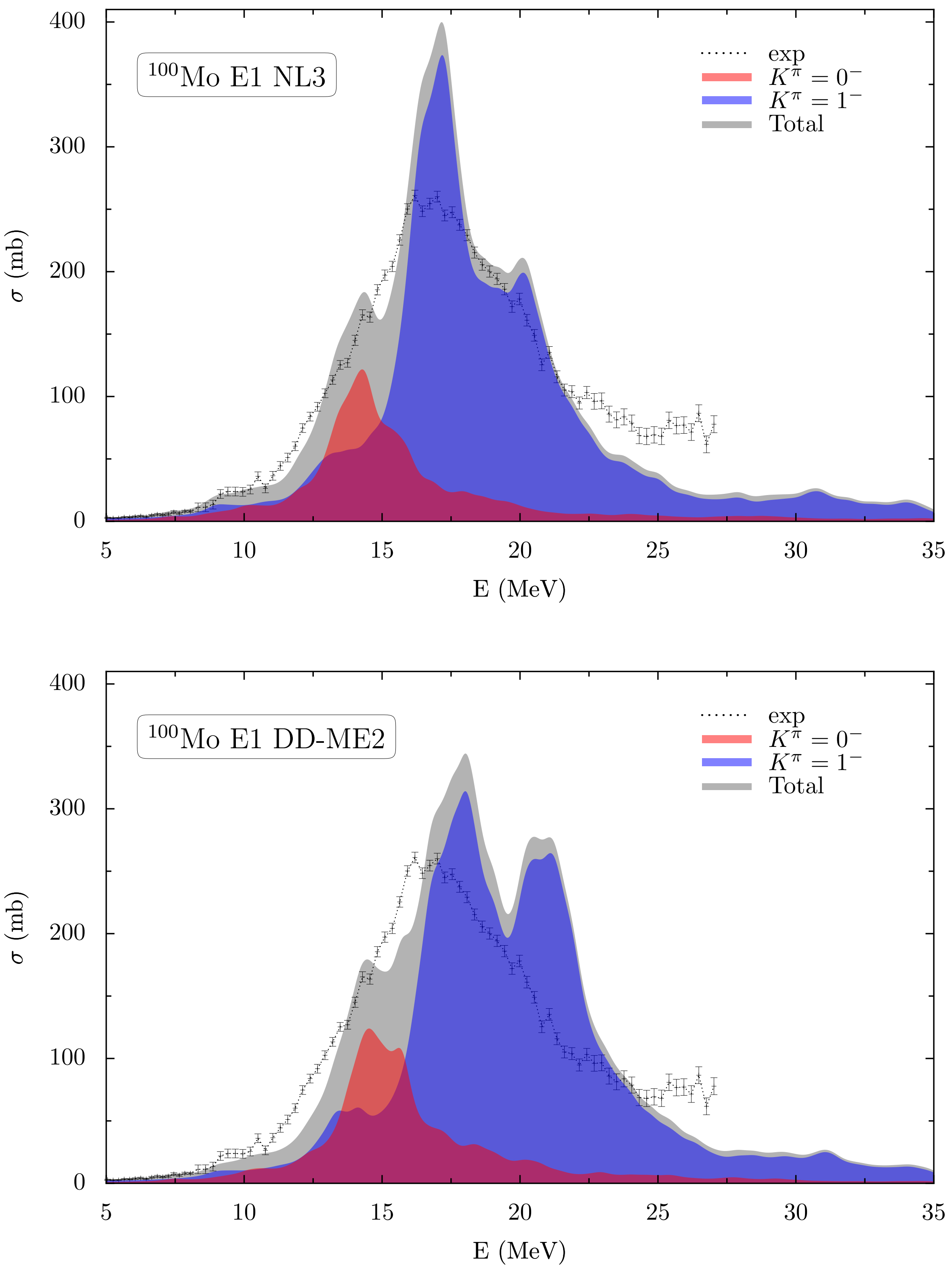

Figure 7.9: Dipole strength in ^{100}Mo for the NL3 and DD-ME2 parameter sets. The red and blue curves correspond to the $K^\pi = 0^-$ and $K^\pi = 1^-$ excitation modes, respectively. The experimental data was taken from references [14, 134].

	m_1/m_0 (MeV)	$\sqrt{m_3/m_1} - m_1/m_0$ (MeV)	$\bar{E}_{E1}$ (MeV)	Γ_{E1} (MeV)
NL3	17.4	1.4	17.2	2.4
DD-ME2	18.3	1.2	18.5	3.3
Exp	18.0	1.4	17.4	3.6

Table 7.2: Energy moments (second and third columns) and Lorentz fits (fourth and fifth columns) results for the GDR in ^{100}Mo.

ME2 it is 18.3 MeV. The more recent DD-ME2 parameter set performs very well. The older NL3 is more than half an MeV off the experimental value. Adjusting both the experimental and theoretical data to a Lorentzian over the same energy interval one finds a different picture, as can be seen in Table 7.2. The experimental best Lorentzian fit gives 17.4 MeV as the experimental centroid position for the GDR, while the NL3 and DD-ME2 predict 17.2 MeV and 18.5 MeV, respectively.

Interestingly enough, at a first glance to Figure 7.9 the NL3 parameter set seems to perform better, in agreement with the Lorentzian fits parameters. In particular, this visual effect is produced because the maximum for the experimental and theoretical curves are closer. However, the quantitative adjustment using energy moments show that, in reality, DD-ME2 performs better. This should not come out as a surprise, as DD-ME2 is adjusted specifically to ground state isovector properties. Attending to the fragmentation of the response, as measured by both the moments and the Lorentzian fits, it is also better reproduced with the more modern DDME functional. The discrepancies between the Lorentzian fits and the energy moments predictions are a well known problem caused by the relatively important influence of the GDR tails in the fitting process. In an effort to minimize this effect it is not uncommon, in well deformed nuclei, to fit to two or even three Lorentzians. However, in the present study, such a fit does not change the results significantly.

As expected, the collectivity of the GDR peaks obtained is very high. The largest single particle contribution in the dominant RPA peak has a share of only 15% of the sum. The total strength of the GDR, for both functionals, is provided by two different clusters of $K^\pi = 1^-$ RPA excitation modes. One cluster is situated in the energy interval 17.5-18 MeV, while the other is around the 16.5-17 MeV energy interval. All the dominant peaks inside these two clusters show the typical isovector pattern in the transition densities. This fine structure of the E1 response at GDR energies was also found in the preceding section for Neon isotopes. However, in this case this feature can also be observed in the experimental data as two separated peaks at the maximum (16-17 MeV). In our calculations the higher lying cluster provides one third more strength to the total response, in contrast with the experimental data where both peaks are of approximately the same height. We have performed some tests to understand this

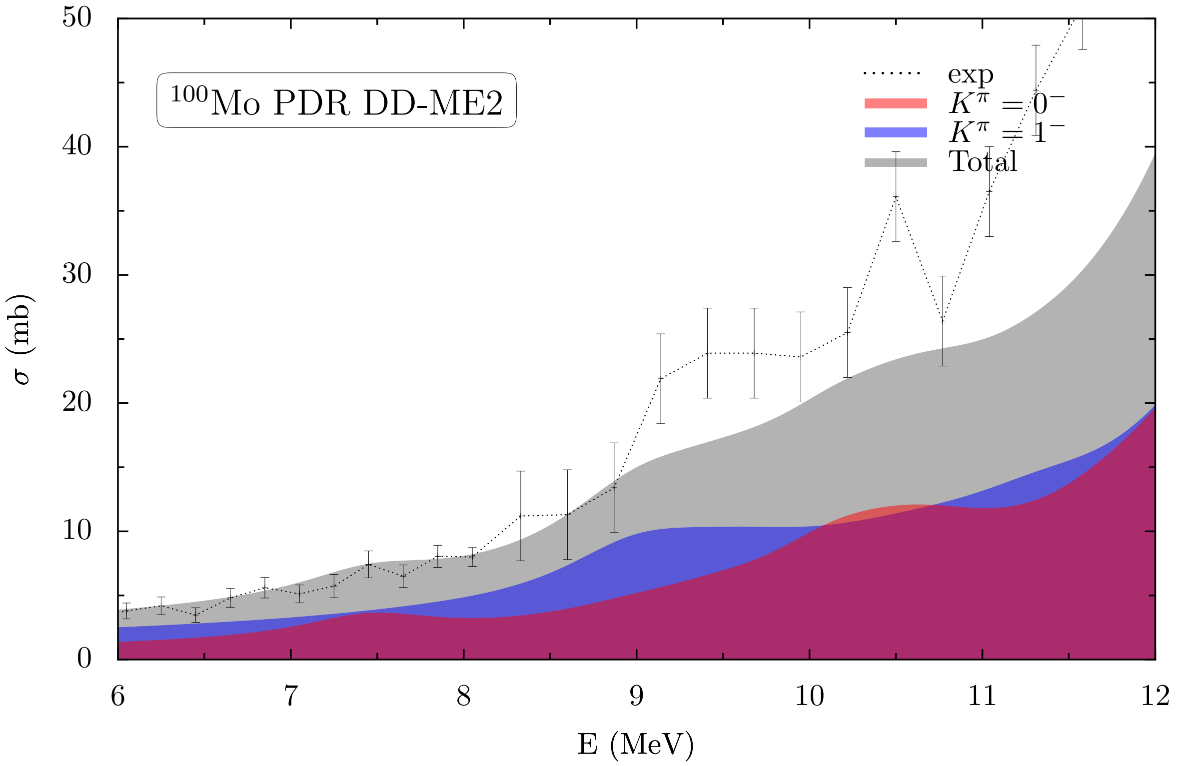

Figure 7.10: Low lying E1 response in ^{100}Mo for the DD-ME2 parameter set.

discrepancy and preliminary results show that the size of the *qp* configuration space plays a very important role in the share of strength that each cluster provides to the total GDR response, even though the Energy Weighted Sum Rule and the centroid energy over the relevant energy range stays practically unchanged. Some reports [35] have attempted to interpret the GDR splitting using a extended collective mode, and their findings link it to deformation effects.

However, a detailed study of our results in that energy region (16-18 MeV) reveals that the splitting is of isovector nature, with mostly neutron excitations in the lower cluster around 16.5 MeV and mostly proton excitations in the region around 17.5 MeV. Thus, this splitting comes from the influence of the electromagnetic interaction or the isovector part of the nuclear force, or a combination of both. Calculations without including the electromagnetic interaction also predict a comparable clustering, so one has to conclude that the splitting is mostly due to the isovector part of the nuclear interaction. Concerning whether the origin is deformation related or not, our results obtained for the spherical nucleus ^{142}Nd show also this fine structure in the GDR, i.e., in our case the effect is not driven by deformation.

Regarding the low lying dipole response, a recent experimental study [134] performed

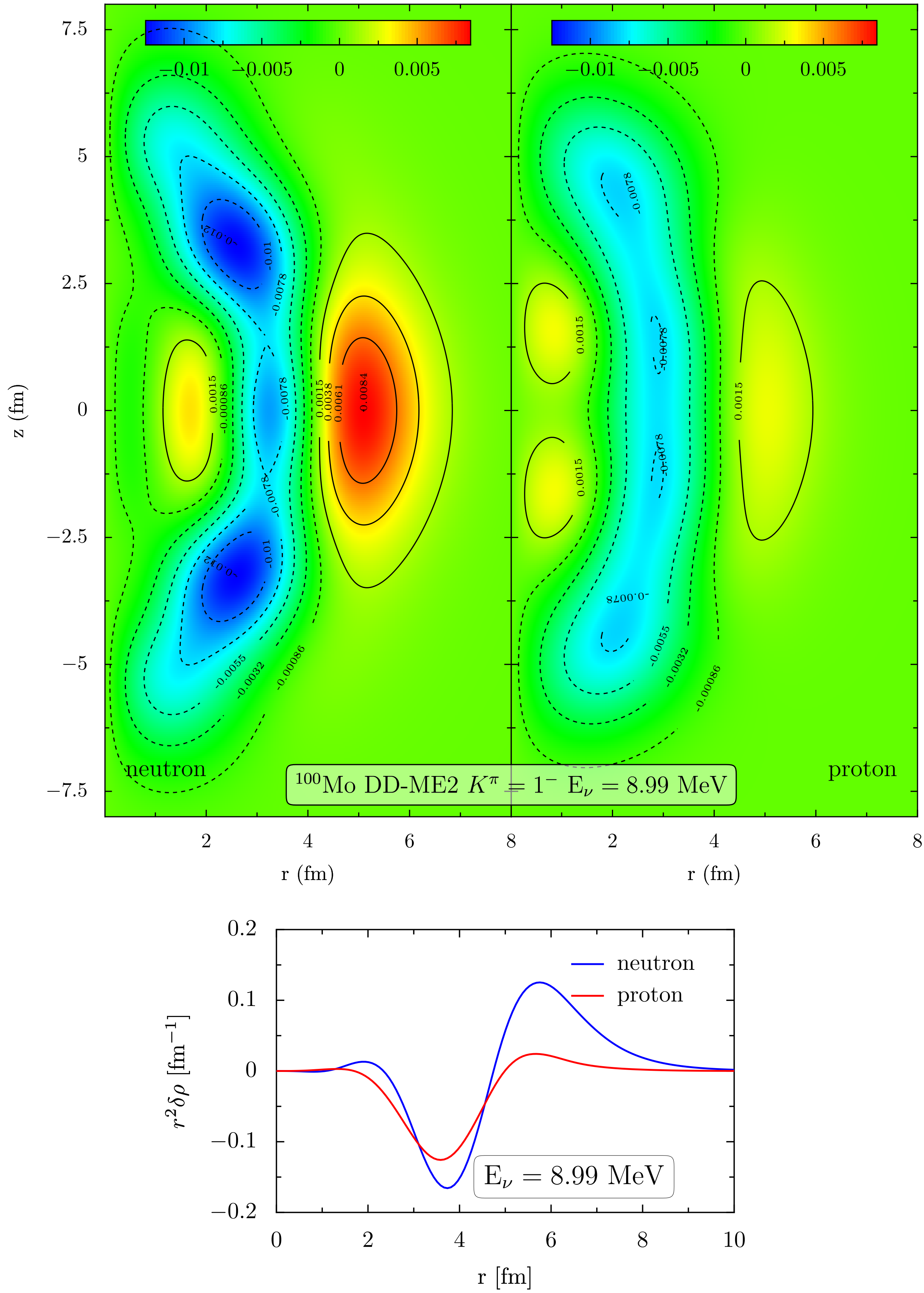

Figure 7.11: Upper panel: transition density for the $K^\pi = 1^-$ peak at 9 MeV, DD-ME2. Lower panel: projected transition density for the same peak.

in Molybdenum isotopes has found non negligible strength enhancements in ^{100} Mo at energies of 6.5 MeV, 7 MeV and 9 MeV. Figure 7.10 is a detailed plot of the E1 strength as calculated with DD-ME2 parameter set in the energy interval 6-12 MeV. The plotted experimental data up to 8 MeV is from reference [134], while for higher energies, above the neutron separation threshold, it was taken from reference [14]. The experimental data points show two enhancements at around 9 MeV and 10.5 MeV, in good agreement with our results, which predict a $K^{\pi} = 1^{-}$ mode peak at 8.9 MeV and a double $K^{\pi} = 0^{-}$ mode peak at 10.5 MeV. In addition to these, Figure 7.10 shows another theoretical $K^{\pi} = 0^{-}$ peak at 7.4 MeV, which can be linked to the 7 MeV enhancement found in the results from reference [134]. In that same study, another peak was found at 6.5 MeV with strong dipole strength. However, even though it appears in our calculated response with both parameter sets, NL3 and DD-ME2, it does not contribute appreciably to the total pygmy strength.

A detailed analysis of the peak at 7.4 MeV reveals that 90% of its total strength comes from a unique single particle transition. In particular, the radial dependence of its projected transition density does not exhibit the typical characteristics of a pygmy resonance. This contradicts the conclusions of reference [134], where it was postulated that this peak belongs to a sequence of pygmy resonances, extending from 6 MeV up to 11 MeV. However, the strong peak at 9 MeV, which is well reproduced in our results and was identified in the same study as a pygmy resonance, displays all the characteristics linked with a soft dipole mode. The upper plot in Figure 7.11 is the intrinsic transition density for the peak as calculated with the DD-ME2 parameter set. Neutrons are clearly in-phase with protons in the nuclear interior, composing the typical pygmy inner core, while on the surface region only neutrons contribute, out of phase with the core, with a very extended transition probability. In the lower panel of the same figure is depicted the projected transition density for that same excitation mode. It confirms the interpretation of the intrinsic transition density. Neutrons and protons are in phase within the nuclear interior and form a core against which a skin composed predominantly of neutrons, with a very long tail, vibrates.

The single particle structure of both modes (at 7.4 MeV and 9 MeV) can be found in Table 7.3. The high collectivity found in both cases is remarkable, with many contributions coming from different single particle configurations. This fact is in contradiction with other theoretical studies where the collectivity of the PDR was found not to be so high. Two effects might be adding up to build such a high collectivity. First, the explicit increase in the configuration space, over spherical calculations, in the deformed case. And second, the influence of pairing correlations, allowing many more possible single particle transition in the same energy range.

The decomposition of the PDR at 9 MeV attending to its single particle configuration presented in Table 7.3, indicates clearly that it is an excitation dominated by neutrons,

Peak at 8.7 MeV, NL3 parameter set			ΔE
neutron	19%	$+\frac{1}{2}^{+}([420]\,81\%) \rightarrow +\frac{1}{2}^{-}([541]70\%)$	9.23
neutron	16%	$+\frac{3}{2}^{+}([422]\,86\%) \rightarrow -\frac{3}{2}^{-}([541]70\%)$	9.41
neutron	9%	$-\frac{3}{2}^{-}([301]\,95\%) \rightarrow +\frac{5}{2}^{+}([413]92\%)$	8.91
neutron	6%	$+\frac{5}{2}^{+}([422]\,92\%) \rightarrow -\frac{3}{2}^{-}([541]76\%)$	9.14
neutron	4%	$+\frac{1}{2}^{+}([431]\,73\%) \rightarrow +\frac{1}{2}^{-}([550]77\%)$	10.23
neutron	4%	$+\frac{1}{2}^{-}([301]\,94\%) \rightarrow +\frac{1}{2}^{+}([400]90\%)$	10.64
proton	2%	$+\frac{7}{2}^{-}([303]\,98\%) \rightarrow -\frac{5}{2}^{+}([422]92\%)$	8.6

Peak at 8.9 MeV, DD-ME2 parameter set			ΔE
neutron	15%	$+\frac{3}{2}^{+}([422]\,86\%) \rightarrow -\frac{1}{2}^{-}([541]94\%)$	9.59
neutron	10%	$+\frac{5}{2}^{+}([413]\,92\%) \rightarrow -\frac{3}{2}^{-}([521]59\%)$	9.02
neutron	10%	$+\frac{1}{2}^{+}([301]\,95\%) \rightarrow +\frac{1}{2}^{-}([411]88\%)$	8.98
neutron	3%	$+\frac{1}{2}^{+}([431]\,73\%) \rightarrow +\frac{1}{2}^{-}([550]74\%)$	10.62
proton	3%	$+\frac{3}{2}^{-}([312]\,93\%) \rightarrow -\frac{1}{2}^{-}([440]66\%)$	9.12
neutron	3%	$+\frac{1}{2}^{-}([301]\,95\%) \rightarrow +\frac{1}{2}^{+}([400]89\%)$	11.05
neutron	2.5%	$-\frac{1}{2}^{+}([420]\,82\%) \rightarrow +\frac{3}{2}^{-}([521]59\%)$	9.98
neutron	2.5%	$-\frac{3}{2}^{-}([301]\,95\%) \rightarrow +\frac{5}{2}^{+}([402]92\%)$	11.59

Table 7.3: *ph* structure for the 9 MeV E1 transition operator in ^{100}Mo for NL3 and DD-ME2 parameter sets, respectively. In parenthesis are the oscillator quantum numbers of the oscillator levels with major contribution to the state, with its corresponding percentage. The left column refers to the normalization of RPA amplitudes.

	4-12 MeV (% TRK)	8.5-9.5 MeV(% TRK)	4-27 MeV (% TRK)
Exp	6.9%	0.9%	121%
NL3	6.7%	1.0%	126%
DD-ME2	5.3%	0.8%	140%

Table 7.4: Percentage of the classical Thomas-Reiche-Kuhn sum rule exhausted by the experimental data [14, 134] and the parameter sets NL3 and DD-ME2 in ^{100}Mo.

as was easily gathered from Figure 7.11. Its structure and contribution to the total strength are partially influenced by pairing correlations. Most of the intervening single particle transitions are quenched by the occupation factors, and some would even be forbidden in the absence of pairing correlations. The systematic change in the oscillator quantum numbers of the major components indicates that this pygmy peak is a $\Delta N = 1$ excitation.

In Table 7.4 we show the percentage of the classical Thomas-Reiche-Kuhn sum rule exhausted by the experimental data [14, 134] and the two parameter sets used in the RHB+RQRPA calculations. Three different energy intervals are presented. The NL3 parameter set, with a percentage of 5.7% in the low lying energy region 4-12 MeV, reproduces the experimental value of 6.9% very well, while the DD-ME2 parameter set underestimates the strength by more than one percent. For the total energy interval measured in the experiments, again NL3 comes very close and DD-ME2 overestimates in more than 15% the overall strength of the dipole response. The discrepancy in the Thomas-Reiche-Kuhn sum rule over the whole experimental energy range as calculated with the DD-ME2 is produced by an enhancement in the response at energies slightly higher than the GDR, around 22 MeV, that can be observed in Figure 7.9. The strength exhausted by the peak identified as the Pygmy Dipole Resonance is around 1% of the total TRK sum rule. Compared to other heavy nuclei where these soft collective dipole modes exhaust up to 5% of the classical TRK sum rule, the PDR in ^{100}Mo is not very pronounced.

To summarise, the results obtained within the RHB+RQRPA framework for deformed nuclei for the GDR agree reasonably well with the experimental data from reference [14] and [134]. Surprisingly, we have found that the performance of the NLME functional with the NL3 parameter set in the prediction of the giant dipole resonance features is on a par with the DDME functional using the DD-ME2 parameter set. We have confirmed the presence of soft collective mode of pygmy character at 9 MeV in ^{100}Mo, that exhaust around 1% of the classical Thomas-Reiche-Kuhn sum rule. Its collectivity has been found to be high and the detailed structure compatible with the features found in studies carried out in spherical symmetry. However, the analysis of two other experimentally found peaks in the same energy region disagrees with the conclusion presented in reference [134], i.e., that they are of pygmy character; our results indicate those peaks have very a markedly single particle nature.

Chapter 8

Summary and Conclusions

"Physics is becoming so unbelievably complex that it is taking longer and longer to train a physicist. It is taking so long, in fact, to train a physicist to the place where he understands the nature of physical problems that he is already too old to solve them."

— Eugene P. Wigner, 1902-1995

In the present investigation we have formulated the relativistic quasiparticle random phase approximation (RQRPA) on the basis of a relativistic Hartree-Bogoliubov (RHB) model having axial symmetry. The RHB model provides a unified description of mean field and pairing correlations, making it a ideal tool for the study of nuclei over the entire nuclear chart. The RHB+RQRPA model employed in this work is fully self-consistent. For the interaction in the particle-hole channel three different density functionals were used, i.e. the standard RMF functional with non-linear meson self interactions, the RMF functional with density dependent meson-nucleon coupling constants, and the RMF functional with density dependent point couplings. Pairing correlations are described, as a first step, using a very simple monopole pairing force. The same interaction is used in both the RHB equations and in the matrix equations of the RQRPA. As it has been shown, this self-consistency feature is of vital importance for the fulfillment of current conservation and the decoupling of spurious modes.

The two-quasiparticle QRPA configuration space includes states with both nucleons in the discrete bound levels, states with one nucleon in the continuum, and also states with both nucleons in the continuum. The Dirac sea is consistently taken into account when constructing the configuration space. This is of paramount importance for the decoupling of spurious states, as well as for the proper description of the position of collective giant resonances.

A great deal of effort and time was spent in the construction and validation of a parallel computer code written in FORTRAN 90 for solving the axial symmetry RQRPA equations in the canonical basis. Through extensive testing, the correctness of the implemented numerical solution has been proved. In particular, we have presented a systematic study of the relevant numerical parameters, which shows that realistic calculation in heavy nuclei are possible without sacrificing accuracy in the results. The decoupling of the spurious Goldstone modes associated with the broken rotational, translational and particle number symmetries is accomplished without further adjustments in the interaction. Their influence on the physical results has been demonstrated to be minimal.

We have applied the implemented framework to the study of the M1 excitations in sample nuclei, in particular the scissors and spin excitation modes. Results for ^{156}Gd show a relatively good agreement with experimental data, and essential physical features are well reproduced. It has been shown that the response is divided in two well separated regions, a low lying one between 2-5 MeV were there exists strong orbital response, and another between 5-10 MeV where the dominant excitation mechanism is due to spin-flip transitions. However, the results indicate that the supposed dominant orbital nature of the scissors mode cannot be fully established as the response of the spin part of M1 is as strong, if not stronger, than its orbital part. In addition to the scissors mode, a soft M1 mode with strong orbital character is found in ^{156}Gd at relatively low energies. From the analysis of the proton and neutron transition densities in the intrinsic frame, and from the structure of the RQRPA amplitudes, it is concluded that this mode corresponds to a collective rotation of the deformed neutron skin against the deformed proton-neutron core.

The existence of heavy fragmentation in the energy region corresponding to the scissors mode has been traced back to the single particle ground state structure. The peak identified as the scissors mode shows a moderately collective behaviour, being three *ph* configuration responsible for approximately 90% of the observed response and the rest distributed between different *ph* configurations with lesser contributions. The two characteristic and experimentally well known “bumps“ in the M1 spin excitations are well reproduced within the RQRPA model with the studied interactions. Their different isospin structure shows that the low lying mode exhibits a dominant isoscalar nature, while the peak at higher energy has a dominant isovector character. Both have a radically different single particle structure compared to the low-lying peaks with strong orbital character.

The RHB+RQRPA in axial symmetry has also been applied to the study of E1 excitations, in particular the GDR and the recently observed low lying modes. Results for nuclei in the isotope chain ^{20}Ne–^{28}Ne are presented and analysed in comparison with recent experimental results on the low lying E1 spectrum in ^{26}Ne. Remarkable agreement with experiment is found for the position of the GDR in the two nuclei (^{20}Ne and ^{22}Ne) for which data is available, even though small differences between the different functionals and parameter sets used are evident.

The appearance of a soft collective mode in the region between 8-12 MeV for ^{26}Ne exhausting around 5% of the classical Thomas-Reiche-Kuhn sum rule agrees with the conclusions of experimental studies. Its structure resembles that of a mixture of dipole and pygmy excitation modes, and hints to the possibility that the simple interpretation of these modes as a vibration of a core composed of protons and neutrons against an outer shell of excess neutrons is no longer fully valid in light deformed nuclei. It has been found that the collectivity of these soft modes is increased compared to similar studies in spherical nuclei, in part due to the artificial increase in the available configuration space and in part due to pairing correlations. On the other hand, pairing correlations have been found to be responsible for the quenching of the total strength exhausted by these low lying soft collective modes. Since the single particle structure greatly influences the excitation response in this kind of nuclei, however, further study is necessary to draw final conclusions.

In order to compare with some very recent experimental results, we have also undertaken the study of E1 excitations in ^{100}Mo. General features of the Giant Dipole Resonance are well reproduced by the different calculations performed with various density functionals and parameter sets. The absence of significant low lying strength compared with that of other heavy nuclei fully agrees with the published data. The analysis of the structure of the low lying dominant peaks at 7 MeV and 9 MeV reveal that their properties differ greatly. The former is composed of a single particle transition up to 80%, while the later displays a mild collectivity and pygmy-like features. We have thus confirmed the presence of soft collective mode of pygmy character at 9 MeV in ^{100}Mo, that exhaust around 1% of the classical Thomas-Reiche-Kuhn sum rule.

Future applications, already achievable with the presented RHB+RQRPA for deformed nuclei, include the systematic study of the influence of deformation in nuclear excitations, other multipolarities, the onset of collective modes. We would also like to give a brief outlook of future extensions and improvements, planned or already under development, which show the direction, scope and possibilities that such a framework offers. These include:

i) Improving parameter sets. Systematic differences in the performance of the three models implemented have been identified and studied under the relatively small scope of the sample applications presented in this document. As it is known from the success of the Nilsson mode, deformed nuclei have been found to be better mean field nuclei than spherical systems. Due to the additional correlations connected with the violation of the rotational symmetry, mean field theories provide a much better description of these deformed systems than they do in spherical nuclei, where the exact ground state contains large admixtures of low-lying surface phonons. Thus, the development of future energy functionals that carry further the quantitative understanding of nuclear systems can greatly benefit from the input that can be gathered from the study of excitations in deformed nuclei. Identifying shortcomings and distinguishing trends between different functionals will surely lead to an overall better description and understanding of nuclear phenomena.

ii) Better treatment of pairing. A better treatment of pairing correlations opens the door to the study of exotic nuclei close to the drip lines, where new nuclear structure is being reported in recent experimental and theoretical results. The understanding of questions like the influence of the change in shell structure in nuclear excitations, or the evolution and development of collective soft modes, can be properly undertaken with a better implementation of pairing correlations in the developed RMF+RQRPA framework for deformed nuclei. In particular, it will be essential for applications in exotic nuclei, where experiments are missing, to count on a pairing interaction that does not depend on the experimental knowledge of the gaps.

iii) Applications to astrophysics. A direct and natural extension to this work is the inclusion of proton-neutron RPA. Gamow-Teller and isobaric analog resonances play a very important role in astrophysics. Electroweak interactions such as scattering and absorption of electrons and neutrinos are strongly influenced by these resonances. They play an essential role during many stages in the evolution of stellar objects. The knowledge of such reaction rates provides a crucial input for the modeling of supernova explosions as well as accretion processes in binary systems. Nuclear netowork calculations for the description of nucleosynthesis are of particular importance in the understanding of heavy element abundancies in the universe, and require a precise knowledge of such reaction rates.

iv) Beyond-RPA. The use of response formalism, instead of the direct diagonalization of the RPA matrix equation, will enable the inclusion of beyond-RPA models and techniques, which have been proven to provide very good agreement with available experimental data in spherical nuclei. The ground work has already been laid down with a reference implementation that reproduces the results of spherical calculations and the data presented in this document. It is now being tested for its extensibility. Even though the feasibility of such an ambitious project depends crucially on efficient numerical techniques and the availability of good computer facilities, we are confident that in the near future we will be able to include beyond-RPA effects in our framework.

In conclusion, the relativistic RQRPA formulated in axially deformed systems represents a significant new theoretical tool for a realistic description of excitation phenomena in large regions of the nuclear chart, which has been accessible so far only by relatively crude phenomenological models. Its development, and the few sample applications presented in this document, show that its future use in nuclear structure and astrophysics will provide an valuable insight into very important, and still open, questions about the nature of the nuclear interaction, collective response, deformation effects, heavy element abundances and cross sections relevant in astrophysical processes.

Appendix A

Residual interaction two-body matrix elements

A.1 Density functionals with non-linear σ-meson field

The residual interaction is

$$\hat{v}^{ph} = \hat{v}_\sigma + \hat{v}_\omega + \hat{v}_\rho + \hat{v}_\gamma \tag{A.1}$$

where each one of the terms is

- σ meson field
$$\hat{v}^{ph}_\sigma(\mathbf{r},\mathbf{r}') = -g_\sigma^2 G_\sigma(\mathbf{r},\mathbf{r}') \tag{A.2}$$
- ω meson field
$$\hat{v}^{ph}_\omega(\mathbf{r},\mathbf{r}') = g_\omega^2 \gamma^\mu G_\omega(\mathbf{r},\mathbf{r}')\gamma'_\mu \tag{A.3}$$
- ρ meson field
$$\hat{v}^{ph}_\rho(\mathbf{r},\mathbf{r}') = g_\rho^2 \gamma^\mu \vec{\tau} G_\rho(\mathbf{r},\mathbf{r}')\gamma'_\mu \vec{\tau}' \tag{A.4}$$
- photon field
$$\hat{v}^{ph}_\gamma(\mathbf{r},\mathbf{r}') = \frac{e^2}{4}\gamma^\mu(1-\tau_3)G_\gamma(\mathbf{r},\mathbf{r}')\gamma'_\mu(1-\tau'_3) \tag{A.5}$$

with the propagators for the ω, ρ and γ fields

$$G_\phi(\mathbf{r},\mathbf{r}') = \frac{e^{-m_\phi|\mathbf{r}-\mathbf{r}'|}}{4\pi|\mathbf{r}-\mathbf{r}'|} \tag{A.6}$$

The propagator for the σ field does not have an analytic expression and has to be calculated numerically using the corresponding Klein-Gordon equation. In momentum space the two-body matrix elements $V^{ph}_{minj} = \langle mi|\hat{v}^{ph}|jn\rangle$ are

$$V^{ph}_{minj} = \frac{1}{(2\pi)^3} \sum_{m=\sigma,\omega,\rho,\gamma} \int d^3k \int d^3k Q^{\mu}_{mi}(\mathbf{k}) \Delta_m(\mathbf{k},\mathbf{k}') Q_{nj,\mu}(-\mathbf{k}) \tag{A.7}$$

with the propagators for the linear meson fields (i.e. ω, ρ and γ)

$$\Delta_m(\mathbf{k},\mathbf{k}') = \frac{\delta(\mathbf{k}-\mathbf{k}')}{\mathbf{k}^2+m^2} \tag{A.8}$$

Details for the calculation of the propagator for the σ meson field are given in Appendix D. The single particle matrix elements Q are defined as

$$Q^{\mu}_{mi}(\mathbf{k}) = \int d^3r \bar{\varphi}_m(\mathbf{r}) \Gamma^{\mu} \varphi_i(\mathbf{r}) e^{-i\mathbf{kr}} \tag{A.9}$$

with the vertices Γ^{μ} given by

$$\Gamma_{\sigma} = g_{\sigma}, \qquad \Gamma^{\mu}_{\omega} = g_{\omega}\gamma^{\mu}, \qquad \Gamma^{\mu}_{\rho} = g_{\rho}\vec{\tau}\gamma^{\mu}, \qquad \Gamma^{\mu}_{e} = e\frac{1-\tau_3}{2}\gamma^{\mu} \tag{A.10}$$

and the single-particle Dirac spinors

$$\varphi_i(\mathbf{r}) = \frac{1}{\sqrt{2\pi}} \begin{pmatrix} f_i^+(r_\perp,z)e^{i(\Omega_i-1/2)\phi} \\ f_i^-(r_\perp,z)e^{i(\Omega_i+1/2)\phi} \\ ig_i^+(r_\perp,z)e^{i(\Omega_i-1/2)\phi} \\ ig_i^-(r_\perp,z)e^{i(\Omega_i+1/2)\phi} \end{pmatrix} \chi_{t_i(t)} \tag{A.11}$$

In cylindrical coordinates $((r_\perp,\phi,z)$ and $(k_\perp,\chi,k_z))$ we find for the dot product $\mathbf{k}\cdot\mathbf{r}$

$$\mathbf{k}\cdot\mathbf{r} = k_\perp r_\perp \cos(\chi-\phi) + k_z z \tag{A.12}$$

Using the Dirac basis

$$\{\gamma^0, \gamma^+ = \frac{-1}{\sqrt{2}}(\gamma^1+i\gamma^2), \gamma^- = \frac{1}{\sqrt{2}}(\gamma^1-i\gamma^2), \gamma^3\} \tag{A.13}$$

it can be easily shown that for each μ, the factor $\overline{\varphi}_m(r_\perp,z,\phi)\,\Gamma^{\mu}\,\varphi_i(r_\perp,z,\phi)$ can be expressed as

$$\overline{\varphi}_m(r_\perp,z,\phi)\,\Gamma^{\mu}\,\varphi_i(r_\perp,z,\phi) = \frac{\alpha}{2\pi}\,F^{\mu}_{mi}(r_\perp,z)\,e^{in\phi} \tag{A.14}$$

where n is an integer of the form $n = -\Omega_m + \Omega_i \pm \{0,1\}$, $\alpha = \pm\{1,i\}$ is a phase and F is a real function that does not depend on the azimuthal angle ϕ. The single particle matrix elements can thus be written as

$$Q^{\mu}_{mi}(\mathbf{k}) = \alpha \iiint r_{\perp} dr_{\perp}\, dz\, \frac{d\phi}{2\pi}\, F^{\mu}_{mi}(r_{\perp}, z)\, e^{in\phi}\, e^{ik_z z}\, e^{ik_{\perp} r_{\perp}\, \cos(\phi - \chi)} \tag{A.15}$$

By means of the following variable change

$$\phi - \chi = \theta \qquad d\phi = d\theta \qquad \phi = \theta + \chi \tag{A.16}$$

it becomes

$$Q^{\mu}_{mi}(\mathbf{k}) = \alpha\, e^{in\chi} \iint r dr\, dz\, F^{\mu}_{mi}(r_{\perp}, z)\, e^{ik_z z} \int \frac{d\theta}{2\pi}\, e^{in\theta}\, e^{ik_{\perp} r_{\perp}\, \cos\theta} \tag{A.17}$$

and using the integral expression for the Bessel functions of the first kind

$$i^n J_n(x) = \int_0^{2\pi} \frac{d\phi}{2\pi}\, e^{in\phi} e^{ix\cos\phi} \tag{A.18}$$

it can be written as

$$Q^{\mu}_{mi}(\mathbf{k}) = i^n \alpha\, e^{in\chi} \iint r_{\perp} dr_{\perp}\, dz\, F^{\mu}_{mi}(r_{\perp}, z)\, J_n(k_{\perp} r_{\perp})\, e^{ik_z z} \tag{A.19}$$

Since the functions F will always have a well defined parity, the exponential in the z-direction reduces to a cosine or sine, giving an extra i factor in the later case.

$$Q^{\mu}_{mi}(\mathbf{k}) = (+i)^n \alpha e^{in\chi} \iint r_{\perp} dr_{\perp} dz\, F^{\mu}_{mi}(r_{\perp}, z) J_n(k_{\perp} r_{\perp}) \{\cos, i\sin\}(k_z z) \tag{A.20}$$

$$Q^{\mu}_{mi}(-\mathbf{k}) = (-i)^n \alpha e^{in\chi} \iint r_{\perp} dr_{\perp} dz\, F^{\mu}_{mi}(r_{\perp}, z) J_n(k_{\perp} r_{\perp}) \{\cos, i\sin\}(k_z z) \tag{A.21}$$

Defining $\mathcal{F}^{\mu}_{mi}(k_{\perp}, k_z)$ as

$$\mathcal{F}^{\mu}_{mi}(k_{\perp}, k_z) = \iint r_{\perp} dr_{\perp} dz\, F^{\mu}_{mi}(r_{\perp}, z) J_n(k_{\perp} r_{\perp}) \{\cos, \sin\}(k_z z) \tag{A.22}$$

we have that the single particle matrix elements read

$$Q^{\mu}_{mi}(\mathbf{k}) = (+i)^n \alpha e^{in\chi} \mathcal{F}^{\mu}_{mi}(k_{\perp}, k_z) \tag{A.23}$$

$$Q^{\mu}_{mi}(-\mathbf{k}) = (-i)^n \alpha e^{in\chi} \mathcal{F}^{\mu}_{mi}(k_{\perp}, k_z) \tag{A.24}$$

and the full two-body matrix elements for a given meson field are

$$V^{ph}_{minj} = \alpha^{\mu}_{mi} \alpha^{\mu}_{nj} \int \frac{d\chi d\chi'}{(2\pi)^3} e^{in^{\mu}_{mi}\chi} e^{in^{\mu}_{nj}\chi'} \cdot \tag{A.25}$$

$$\cdot \iint k_{\perp} dk_{\perp} dk_z k'_{\perp} dk'_{\perp} dk'_z \mathcal{F}^{\mu}_{mi}(k_{\perp}, k_z) \Delta(\mathbf{k}, \mathbf{k}') \mathcal{F}^{\mu}_{nj}(k'_{\perp}, k'_z) \tag{A.26}$$

where summation over μ is implied. For axial symmetry the propagator $\Delta(\mathbf{k}, \mathbf{k}')$ is always factored into a part depending on $k_\perp$ and k_z, and a $\delta(\chi - \chi')$. So in order for this matrix element not to be zero, the argument for the exponential functions in the first integral must vanish, thus getting so the angular momentum projection conservation rule

$$n^\mu_{mi} + n^\mu_{nj} = 0 \tag{A.27}$$

For the σ meson field the vertex is Γ is proportional to the four by four identity matrix, and so the functions F_{mi} read

$$F^{(\sigma)}_{mi} = f^+_m f^+_i + f^-_m f^-_i - g^+_m g^+_i - g^-_m g^-_i \tag{A.28}$$

with $n_{mi} = \Omega_m - \Omega_i$ and $\alpha = 1$.

For the other meson fields the vertexes Γ are proportional to the γ matrices. Remembering that we are using a spherical Dirac basis, the functions F^μ_{mi} are

- For $\mu = 0$
  $$F^0_{mi} = f^+_m f^+_i + f^-_m f^-_i + g^+_m g^+_i + g^-_m g^-_i \tag{A.29}$$
  with $n_{mi} = \Omega_m - \Omega_i$ and $\alpha = 1$.
- For $\mu = +$
  $$F^+_{mi} = g^+_m f^-_i - f^+_m g^-_i \tag{A.30}$$
  with $n_{mi} = \Omega_m - \Omega_i - 1$ and $\alpha = i$.
- For $\mu = -$
  $$F^-_{mi} = f^-_m g^+_i - g^-_m f^+_i \tag{A.31}$$
  with $n_{mi} = \Omega_m - \Omega_i + 1$ and $\alpha = i$.
- For $\mu = 3$
  $$F^3_{mi} = g^+_m f^+_i - f^+_m g^+_i + g^-_m f^-_i - f^-_m g^-_i \tag{A.32}$$
  with $n_{mi} = \Omega_m - \Omega_i$ and $\alpha = -i$.

A.2 Density dependent meson exchange density functionals

The residual interaction is

$$\hat{v}^{ph} = \hat{v}_\sigma + \hat{v}_\omega + \hat{v}_\rho + \hat{v}_\gamma \tag{A.33}$$

where each one of the terms is

- σ meson field

$$\begin{aligned}
\hat{v}^{ph}_{\sigma}(\mathbf{r},\mathbf{r}') = & - g_{\sigma}(\rho_v(\mathbf{r}))G_{\sigma}(\mathbf{r},\mathbf{r}')g_{\sigma}(\rho_v(\mathbf{r}')) \\
& - \left\{ \frac{\partial g_{\sigma}}{\partial \rho_v(\mathbf{r})}\gamma_0' + \frac{\partial^2 g_{\sigma}}{\partial \rho_v^2(\mathbf{r})} + \gamma^0 \frac{\partial g_{\sigma}}{\partial \rho_v(\mathbf{r})} \right\} \sigma(\mathbf{r})\delta(\mathbf{r}-\mathbf{r}') \\
& - \left\{ g_{\sigma}(\rho_v(\mathbf{r}))\frac{\partial g_{\sigma}}{\partial \rho_v(\mathbf{r}')}\gamma_0'\rho_s(\mathbf{r}') + \gamma^0\rho_s(\mathbf{r})\frac{\partial g_{\sigma}}{\partial \rho_v(\mathbf{r})} g_{\sigma}(\rho_v(\mathbf{r}')) \right. \\
& \left. + \gamma^0\rho_s(\mathbf{r})\frac{\partial g_{\sigma}}{\partial \rho_v(\mathbf{r})}\frac{\partial g_{\sigma}}{\partial \rho_v(\mathbf{r}')}\rho_s(\mathbf{r}')\gamma_0' \right\} G_{\sigma}(\mathbf{r},\mathbf{r}') \qquad (A.34)
\end{aligned}$$

- ω meson field

$$\begin{aligned}
\hat{v}^{ph}_{\omega}(\mathbf{r},\mathbf{r}') = & \quad \gamma^{\mu} g_{\omega}(\rho_v(\mathbf{r}))G_{\omega}(\mathbf{r},\mathbf{r}')g_{\omega}(\rho_v(\mathbf{r}))\gamma_{\mu}' \\
& + \left\{ 2\frac{\partial g_{\omega}}{\partial \rho_v(\mathbf{r})} + \frac{\partial^2 g_{\omega}}{\partial \rho_v^2(\mathbf{r})}\rho_v(\mathbf{r}) \right\} \omega(\mathbf{r})\delta(\mathbf{r}-\mathbf{r}') \\
& + \left\{ g_{\omega}(\rho_v(\mathbf{r}))\frac{\partial g_{\omega}}{\partial \rho_v(\mathbf{r}')}\rho_v(\mathbf{r}') + \rho_v(\mathbf{r})\frac{\partial g_{\omega}}{\partial \rho_v(\mathbf{r})} g_{\omega}(\rho_v(\mathbf{r}')) \right. \\
& \left. + \rho_v(\mathbf{r}')\frac{\partial g_{\omega}}{\partial \rho_v(\mathbf{r})}\frac{\partial g_{\omega}}{\partial \rho_v(\mathbf{r}')}\rho_v(\mathbf{r}') \right\} G_{\omega}(\mathbf{r},\mathbf{r}') \qquad (A.35)
\end{aligned}$$

- ρ meson field

$$\begin{aligned}
\hat{v}^{ph}_{\rho}(\mathbf{r},\mathbf{r}') = & \quad \gamma^{\mu}\vec{\tau} g_{\rho}(\rho_{tv}(\mathbf{r}))G_{\rho}(\mathbf{r},\mathbf{r}')g_{\rho}(\rho_{tv}(\mathbf{r}))\vec{\tau}'\gamma_{\mu}' \\
& + \left\{ \frac{\partial g_{\rho}}{\partial \rho_{tv}(\mathbf{r})}\vec{\tau} + \frac{\partial g_{\rho}}{\partial \rho_{tv}(\mathbf{r})}\vec{\tau}' + \frac{\partial^2 g_{\rho}}{\partial \rho_{tv}^2(\mathbf{r})}\rho_{tv}(\mathbf{r}) \right\} \rho(\mathbf{r})\delta(\mathbf{r}-\mathbf{r}') \\
& + \left\{ g_{\rho}(\rho_{tv}(\mathbf{r}))\vec{\tau}\frac{\partial g_{\rho}}{\partial \rho_{tv}(\mathbf{r}')}\rho_{tv}(\mathbf{r}') + \rho_{tv}(\mathbf{r})\frac{\partial g_{\rho}}{\partial \rho_{tv}(\mathbf{r})}\vec{\tau}' g_{\rho}(\rho_{tv}(\mathbf{r}')) \right. \\
& \left. + \rho_{tv}(\mathbf{r}')\frac{\partial g_{\rho}}{\partial \rho_{tv}(\mathbf{r})}\frac{\partial g_{\rho}}{\partial \rho_{tv}(\mathbf{r}')}\rho_{tv}(\mathbf{r}') \right\} G_{\rho}(\mathbf{r},\mathbf{r}') \qquad (A.36)
\end{aligned}$$

- photon field

$$\hat{v}^{ph}_{\gamma}(\mathbf{r},\mathbf{r}') = \frac{e^2}{4}\gamma^{\mu}(1-\tau_3)G_{\gamma}(\mathbf{r},\mathbf{r}')\gamma_{\mu}'(1-\tau_3') \qquad (A.37)$$

The symbols without prime refer to particle 1 and the ones with it to particle 2. ρ_s, ρ_v and ρ_{tv} denote the scalar, vector and isovector-vector density respectively, and the derivatives of the meson-nucleon couplings with respect to the vector density ρ_v are evaluated at the ground state density ρ_v^0. $\sigma(\mathbf{r})$, $\omega(\mathbf{r})$ and $\rho(\mathbf{r})$ refer to the sigma, omega and rho meson fields respectively.

The first terms in all cases can be calculated using the procedure outlined in the previous section. The only difference is that one has to be careful because this time the functions $\mathcal{F}$ contain the coordinate dependent coupling constant g. For example, for the ω channel they would be

$$\mathcal{F}^{\mu}_{mi}(k_\perp, k_z) = \iint r_\perp dr_\perp dz\, g_\omega(\rho(r_\perp, z)) F^{\mu}_{mi}(r_\perp, z) J_n(k_\perp r_\perp)\{\cos, \sin\}(k_z z) \tag{A.38}$$

and similarly for the other meson fields. In addition to the normal terms also found in the linear functionals, the two-body residual interaction of functionals with density dependent nucleon-meson couplings have a number of rearrangement terms. These include two types: one that is formally identical to the others and that contains the usual propagators $G(\mathbf{r}, \mathbf{r}')$, and another where the propagator is substituted by a delta function. In axial symmetry these last ones read

- σ field, contact (delta) terms

$$\begin{aligned} V^{ph}_{minj} &= -\frac{1}{2\pi} \iint r_\perp dr_\perp dz\; \sigma(r_\perp, z) \qquad\qquad (A.39) \\ &\left\{ \frac{\partial^2 g_\sigma}{\partial \rho_v^2(\mathbf{r})} (f_m^+ f_i^+ - f_m^- f_i^- - g_m^+ g_i^+ + g_m^- g_i^-)(f_n^+ f_j^+ - f_n^- f_j^- - g_n^+ g_j^+ + g_n^- g_j^-) \right. \\ &+ \frac{\partial g_\sigma}{\partial \rho_v(\mathbf{r})} (f_m^+ f_i^+ - f_m^- f_i^- + g_m^+ g_i^+ - g_m^- g_i^-)(f_n^+ f_j^+ - f_n^- f_j^- - g_n^+ g_j^+ + g_n^- g_j^-) \\ &+ \left. \frac{\partial g_\sigma}{\partial \rho_v(\mathbf{r})} (f_m^+ f_i^+ - f_m^- f_i^- - g_m^+ g_i^+ + g_m^- g_i^-)(f_n^+ f_j^+ - f_n^- f_j^- + g_n^+ g_j^+ - g_n^- g_j^-) \right\} \end{aligned}$$

- ω field, contact (delta) terms

$$\begin{aligned} V^{ph}_{minj} &= \frac{1}{2\pi} \iint r_\perp dr_\perp dz\; \omega(r_\perp, z) \left\{ 2\frac{\partial g_\omega}{\partial \rho_v(\mathbf{r})} + \frac{\partial^2 g_\omega}{\partial \rho_v^2(\mathbf{r})} \rho_v(\mathbf{r}) \right\} \qquad (A.40) \\ &(f_m^+ f_i^- - f_m^- f_i^+ - g_m^+ g_i^- + g_m^- g_i^+)(f_n^+ f_j^- - f_n^- f_j^+ - g_n^+ g_j^- + g_n^- g_j^+) \end{aligned}$$

- ρ field, contact (delta) terms

$$\begin{aligned} V^{ph}_{minj} &= \frac{1}{2\pi} \iint r_\perp dr_\perp dz\; \rho(r_\perp, z) \left\{ \frac{\partial g_\rho}{\partial \rho_{tv}(\mathbf{r})} \vec{\tau} + \frac{\partial g_\rho}{\partial \rho_{tv}(\mathbf{r})} \vec{\tau}' + \frac{\partial^2 g_\rho}{\partial \rho_{tv}^2(\mathbf{r})} \rho_{tv}(\mathbf{r}) \right\} \\ &(f_m^+ f_i^- - f_m^- f_i^+ - g_m^+ g_i^- + g_m^- g_i^+)(f_n^+ f_j^- - f_n^- f_j^+ - g_n^+ g_j^- + g_n^- g_j^+) \end{aligned} \tag{A.41}$$

A.3 Density dependent point coupling density functionals

The residual interaction is

$$\hat{v}^{ph} = \hat{v}_s + \hat{v}_v + \hat{v}_{ts} + \hat{v}_{tv} + \hat{v}_\gamma \tag{A.42}$$

where each one of the terms is

- scalar isoscalar term

$$\hat{v}_s^{ph}(\mathbf{r}, \mathbf{r}') = (\alpha_s + 2\beta\rho_s + 3\gamma_s\rho_s^2 + \delta_s\Delta)\delta(\mathbf{r} - \mathbf{r}') \tag{A.43}$$

- vector isoscalar term

$$\hat{v}_v^{ph}(\mathbf{r}, \mathbf{r}') = \gamma^\mu(\alpha_v + 2\beta\rho_v + 3\gamma_s\rho_v^2 + \delta_v\Delta)\gamma'_\mu\delta(\mathbf{r} - \mathbf{r}') \tag{A.44}$$

- scalar isovector term

$$\hat{v}_{ts}^{ph}(\mathbf{r}, \mathbf{r}') = \vec{\tau}(\alpha_{ts} + 2\beta\rho_{ts} + 3\gamma_s\rho_{ts}^2 + \delta_{ts}\Delta)\vec{\tau}'\delta(\mathbf{r} - \mathbf{r}') \tag{A.45}$$

- vector isovector term

$$\hat{v}_{tv}^{ph}(\mathbf{r}, \mathbf{r}') = \gamma^\mu\vec{\tau}(\alpha_{tv} + 2\beta\rho_{tv} + 3\gamma_s\rho_{tv}^2 + \delta_{tv}\Delta)\vec{\tau}'\gamma'_\mu\delta(\mathbf{r} - \mathbf{r}') \tag{A.46}$$

- photon field

$$\hat{v}_\gamma^{ph}(\mathbf{r}, \mathbf{r}') = \frac{e^2}{4}\gamma^\mu(1 - \tau_3)G_\gamma(\mathbf{r}, \mathbf{r}')\gamma'_\mu(1 - \tau'_3) \tag{A.47}$$

Appendix B

M1 transition operator

The M1 operator is defined as:

$$\hat{M}_{1\mu} = \mu_N \left(g_s \mathbf{s} + g_l \mathbf{l}\right) \cdot \left(\nabla r Y_{1\mu}(\theta, \phi)\right) \tag{B.1}$$

with

$$\left.\begin{array}{rcl} g_s & = & g_p \\ g_l & = & 1 \end{array}\right\} \text{ protons} \qquad \left.\begin{array}{rcl} g_s & = & g_n \\ g_l & = & 0 \end{array}\right\} \text{ neutrons} \tag{B.2}$$

and where the angular momentum operator $\mathbf{l}$ acts only on the coordinates of the wave-function. If x_μ are the spherical coordinates of $\mathbf{r}$ defined as:

$$\begin{array}{rcl} x_{+1} & = & \frac{-1}{\sqrt{2}}\left(x + iy\right) \\ x_{-1} & = & \frac{1}{\sqrt{2}}\left(x - iy\right) \\ x_0 & = & z \end{array} \tag{B.3}$$

then $rY_{1\mu} = \sqrt{\frac{3}{4\pi}} x_\mu$ and

$$\nabla r Y_{1\mu} = \sqrt{\frac{3}{4\pi}} \partial_i x_k = \sqrt{\frac{3}{4\pi}} \delta_{ik} \tag{B.4}$$

so if $\mathbf{a}$ is a vector in spherical coordinates it follows

$$\mathbf{a} \cdot \left(\nabla r Y_{1\mu}\right) = \sqrt{\frac{3}{4\pi}} a_\mu \tag{B.5}$$

The scissors mode excitation mode is $K = 1^{+}$, and the corresponding operator is the $\hat{M}_{11}$. Using (B.5)

$$\hat{M}_{11} = \sqrt{\frac{3}{4\pi}}\mu_N \left(g_s s_{+1} + g_l l_{+1}\right) \tag{B.6}$$

where l_{+1} and s_{+1} are calculated using (B.3) and read

$$\begin{aligned} s_{+1} &= \frac{1}{2}\Sigma_{+} = \frac{-1}{2\sqrt{2}}\left(\Sigma_x + i\Sigma_y\right) && \text{(B.7)} \\ l_{+1} &= \frac{\mathbb{1}}{2\sqrt{2}}e^{i\phi}\left[r\partial_z - z\left(\partial_r + i\frac{1}{r}\partial_\phi\right)\right] && \text{(B.8)} \end{aligned}$$

So finally the $\hat{M}_{11}$ single particle matrix elements, carrying out the integration over the azimuthal angle ϕ, can be expanded to

$$\begin{aligned} \langle m|\hat{M}_{11}|i\rangle = \quad & \mu_N \delta_{\Omega_m-\Omega_i,1}\frac{1}{\sqrt{2}}\sqrt{\frac{3}{4\pi}}\int \mathrm{r}\mathrm{d}r\mathrm{d}z \\ \Big[\quad - \quad & g_l z\left(f_m^{+}\partial_r f_i^{+} + f_m^{-}\partial_r f_i^{-} + g_m^{+}\partial_r g_i^{+} + g_m^{+}\partial_r g_i^{-}\right) \\ + \quad & g_l r\left(f_m^{+}\partial_z f_i^{+} + f_m^{-}\partial_z f_i^{-} + g_m^{+}\partial_z g_i^{+} + g_m^{-}\partial_z g_i^{-}\right) \\ + \quad & g_l\frac{(\Omega_i - 1/2)z}{r}(f_m^{+}f_i^{+} + g_m^{+}g_i^{+}) \\ + \quad & g_l\frac{(\Omega_i + 1/2)z}{r}(f_m^{-}f_i^{-} + g_m^{-}g_i^{-}) \\ - \quad & g_s\left(f_m^{+}f_i^{-} + g_m^{+}g_i^{-}\right)\Big] \end{aligned} \tag{B.9}$$

Appendix C

E1 transition operator

The effective isovector dipole operator, with the center of mass correction already subtracted, reads

$$\hat{Q}_{1\mu}^{T=1} = e\frac{N}{N+Z}\sum_{p=1}^{Z} r_p Y_{1\mu}(\hat{r}_p) - e\frac{Z}{N+Z}\sum_{n=1}^{N} r_n Y_{1\mu}(\hat{r}_n) \tag{C.1}$$

With the definition of spherical coordinates (B.3) and using the relation $rY_{1\mu} = \sqrt{\frac{3}{4\pi}}x_\mu$ it can be expressed as

$$\hat{Q}_{1\mu}^{T=1} = e\frac{N}{N+Z}\sum_{p=1}^{Z} x_{p\mu} - e\frac{Z}{N+Z}\sum_{n=1}^{N} x_{n\mu} \tag{C.2}$$

And in cylindrical coordinates the three components are

$$\begin{aligned}
\hat{Q}_{10}^{T=1} &= e\frac{N}{N+Z}\sum_{p=1}^{Z} z_p - e\frac{Z}{N+Z}\sum_{n=1}^{N} z_n \\
\hat{Q}_{1\pm1}^{T=1} &= e\frac{N}{N+Z}\sum_{p=1}^{Z} r_{p\perp}e^{\pm i\phi} - e\frac{Z}{N+Z}\sum_{n=1}^{N} r_{n\perp}e^{\pm i\phi}
\end{aligned} \tag{C.3}$$

And the single particle matrix elements are

$$\begin{aligned}
\langle m|\hat{Q}_{10}^{T=1}|i\rangle &= -\delta_{\Omega_m-\Omega_i,0}\frac{eN}{A}\int rzdrdz\left(f_m^+f_i^- - f_m^-f_i^+ - g_m^+g_i^- + g_m^-g_i^+\right) \\
\langle m|\hat{Q}_{11}^{T=1}|i\rangle &= -\delta_{\Omega_m-\Omega_i,1}\frac{eN}{A}\int r^2drdz\left(f_m^+f_i^- - f_m^-f_i^+ - g_m^+g_i^- + g_m^-g_i^+\right)
\end{aligned} \tag{C.4}$$

for proton pairs, and

$$\begin{aligned}
\langle m|\hat{Q}^{T=1}_{10}|i\rangle &= +\delta_{\Omega_m-\Omega_i,0}\frac{eZ}{A}\int rzdrdz\left(f^+_m f^-_i - f^-_m f^+_i - g^+_m g^-_i + g^-_m g^+_i\right) \\
\langle m|\hat{Q}^{T=1}_{11}|i\rangle &= +\delta_{\Omega_m-\Omega_i,1}\frac{eZ}{A}\int r^2drdz\left(f^+_m f^-_i - f^-_m f^+_i - g^+_m g^-_i + g^-_m g^+_i\right)
\end{aligned} \tag{C.5}$$

for neutron pairs.

Appendix D

Non-linear Sigma Field

D.1 Plane wave expansion in cylindrical coordinates

The plane wave $e^{\mathrm{i}\boldsymbol{kr}}$ in cylindrical coordinates with $\boldsymbol{r} = (z, r, \varphi)$ and $\boldsymbol{k} = (k_z, k_\perp, \chi)$ can be written as

$$e^{\mathrm{i}\boldsymbol{kr}} = e^{\mathrm{i}k_z z} e^{\mathrm{i}k_\perp r cos(\varphi - \chi)}. \tag{D.1}$$

The first exponential of the decomposition is trivial to handle in the calculations, so let us concentrate in the last term. We would like to expand it as a series:

$$e^{\mathrm{i}x cos(\alpha)} = \sum_{n=-\infty}^{\infty} C_n e^{\mathrm{i}n\alpha} \tag{D.2}$$

where we have to determine the coefficients C_n. Using the integral representation for the Bessel function we find

$$J_n(x) = \frac{1}{2\pi \mathrm{i}^n} \int_0^{2\pi} e^{\mathrm{i}x cos(\alpha)} e^{\mathrm{i}n\alpha} \mathrm{d}\alpha = \frac{1}{2\pi \mathrm{i}^n} \sum_{n'=-\infty}^{\infty} C_{n'} \int_0^{2\pi} e^{\mathrm{i}(n+n')\alpha} \mathrm{d}\alpha = \mathrm{i}^{-n} C_{-n} \tag{D.3}$$

With the properties of the Bessel functions

$$J_{-n}(x) = J_n(-x) = (-)^n J_n(x) \tag{D.4}$$

we get

$$e^{\mathrm{i}x cos(\alpha)} = \sum_{n=-\infty}^{\infty} \mathrm{i}^n J_n(x) e^{\mathrm{i}n\alpha} \tag{D.5}$$

or

$$e^{\mathrm{i}\boldsymbol{k}\boldsymbol{r}} = e^{\mathrm{i}k_z z} e^{\mathrm{i}k_\perp r cos(\varphi-\chi)} = e^{\mathrm{i}k_z z} \sum_{n=-\infty}^{\infty} \mathrm{i}^n J_n(k_\perp r) e^{\mathrm{i}n(\varphi-\chi)}. \tag{D.6}$$

D.2 The Klein-Gordon equation

The meson equation for the non-linear sigma channel is

$$[-\Delta + m_\sigma^2]\sigma = -g_\sigma \rho_s - g_2\sigma^2 - g_3\sigma^3 \tag{D.7}$$

In the small amplitude limit $\sigma(t) = \sigma_0 + \delta\sigma$ it becomes

$$[-\Delta + m_\sigma^2 + U(\boldsymbol{r})]\delta\sigma(\boldsymbol{r}) = -g_\sigma \delta\rho_s(\boldsymbol{r}) \tag{D.8}$$

with

$$U(\boldsymbol{r}) = 2g_2\sigma + 3g_3\sigma^2 \tag{D.9}$$

Because of axial symmetry

$$U(\boldsymbol{r}) \equiv U(r, z) \tag{D.10}$$

Performing a Fourier transformation of equation (D.8) we obtain from the folding rule

$$(f * g)(\boldsymbol{k}) = \int d^3r\ f(\boldsymbol{r})g(\boldsymbol{r})e^{-i\boldsymbol{k}\boldsymbol{r}} = \int \frac{d^3k'}{(2\pi)^3} f(\boldsymbol{k}-\boldsymbol{k}')g(\boldsymbol{k}') \tag{D.11}$$

the Klein-Gordon equation in Fourier space

$$(\boldsymbol{k}^2 + m_\sigma^2)\delta\sigma(\boldsymbol{k}) + U(\boldsymbol{k}) * \delta\sigma(\boldsymbol{k}) = -g_\sigma \delta\rho_s(\boldsymbol{k}). \tag{D.12}$$

The $*$ is the convolution operator, so that

$$(\boldsymbol{k}^2 + m_\sigma^2)\delta\sigma(\boldsymbol{k}) + \int \frac{\mathrm{d}^3k'}{(2\pi)^3} U(\boldsymbol{k}-\boldsymbol{k}')\delta\sigma(\boldsymbol{k}') = -g_\sigma \delta\rho_s(\boldsymbol{k}) \tag{D.13}$$

Using axial symmetry we obtain

$$
\begin{aligned}
U(\boldsymbol{k}-\boldsymbol{k}') &= \int \mathrm{d}^3r\; U(r,z)\, e^{-\mathrm{i}\boldsymbol{k}\boldsymbol{r}} e^{\mathrm{i}\boldsymbol{k}'\boldsymbol{r}} \\
&= \int \mathrm{d}^3r\; U(r,z) e^{-\mathrm{i}(k_z-k_z')z} \sum_{n=-\infty}^{\infty} \mathrm{i}^{-n} J_n(k_\perp r) e^{-\mathrm{i}n(\varphi-\chi)} \sum_{n'=-\infty}^{\infty} \mathrm{i}^{n'} J_{n'}(k_\perp' r) e^{\mathrm{i}n'(\varphi-\chi')} \\
&= 2\pi \sum_n e^{\mathrm{i}n(\chi-\chi')} \int r\mathrm{d}r\mathrm{d}z\; U(r,z) J_n(k_\perp r) J_n(k_\perp' r) e^{-\mathrm{i}(k_z-k_z')z} \\
&= (2\pi)^2 \sum_n e^{\mathrm{i}n(\chi-\chi')} U_n(k_\perp, k_z, k_\perp', k_z') \qquad \text{(D.14)}
\end{aligned}
$$

with $\mathrm{d}^2r = r\mathrm{d}r\mathrm{d}z$

$$
U_n(k_\perp, k_z, k_\perp', k_z') = \frac{1}{2\pi} \int \mathrm{d}^2r\, U(r,z)\, e^{-\mathrm{i}(k_z-k_z')z} J_n(k_\perp r)\, J_n(k_\perp' r) \qquad \text{(D.15)}
$$

The source term in the Klein-Gordon equation (D.8) is periodic in the angle φ

$$
-g_\sigma \delta\rho_s(\boldsymbol{r}) = g_\sigma \mathrm{Q}_{mi}(\boldsymbol{r}) = \overline{\varphi}_m(\boldsymbol{r})\; \varphi_i(\boldsymbol{r}) = \mathrm{F}_{mi}(r,z) e^{-\mathrm{i}K\varphi} \qquad \text{(D.16)}
$$

where K is an integer. We therefore find in Fourier space with Equation (D.6)

$$
\begin{aligned}
-\, g_\sigma \delta\rho_s(\boldsymbol{k}) &= \int \mathrm{d}^3r\; \mathrm{F}_{mi}(r,z) e^{-\mathrm{i}K\varphi} e^{-\mathrm{i}\boldsymbol{k}\boldsymbol{r}} \\
&= \int \mathrm{d}^3r\; \mathrm{F}_{mi}(r,z) e^{-\mathrm{i}K\varphi} e^{-\mathrm{i}k_z z} \sum_{n=-\infty}^{\infty} (-\mathrm{i})^n J_n(k_\perp r) e^{-\mathrm{i}n(\varphi-\chi)} \\
&= \mathrm{i}^K e^{-\mathrm{i}K\chi} \int \mathrm{d}^2r\; \mathrm{F}_{mi}(r,z)\; J_K(k_\perp r) e^{-\mathrm{i}k_z z} \qquad \text{(D.17)}
\end{aligned}
$$

So we can write

$$
\delta\rho_s(\boldsymbol{k}) = \delta\rho_s(k_\perp, k_z) e^{-\mathrm{i}K\chi} \qquad \text{(D.18)}
$$

with

$$
-g_s \delta\rho_s(k_\perp, k_z) = \mathrm{i}^K \int \mathrm{d}^2r\; \mathrm{F}_{mi}(r,z) J_K(k_\perp r) e^{-\mathrm{i}k_z z} \qquad \text{(D.19)}
$$

Thus the Klein Gordon equation in Fourier space has the form

$$
(\boldsymbol{k}^2 + m_\sigma^2)\delta\sigma(\boldsymbol{k}) + \int \frac{\mathrm{d}^3k'}{(2\pi)^3} U(\boldsymbol{k}-\boldsymbol{k}')\delta\sigma(\boldsymbol{k}') = -g_\sigma \delta\rho_s(k_\perp, k_z) e^{-\mathrm{i}K\chi} \qquad \text{(D.20)}
$$

Therefore we make the ansatz

$$
\delta\sigma(\boldsymbol{k}) = \delta\sigma(k_\perp, k_z) e^{-\mathrm{i}K\chi} \qquad \text{(D.21)}
$$

and find

$$(\boldsymbol{k}^2+m_\sigma^2)\delta\sigma(k_\perp,k_z)+\int\frac{\mathrm{d}^3k'}{(2\pi)^3}U(\boldsymbol{k}-\boldsymbol{k}')\delta\sigma(k'_\perp,k'_z)e^{\mathrm{i}K(\chi-\chi')}=-g_\sigma\delta\rho_s(k_\perp,k_z) \quad \text{(D.22)}$$

Now, using Equation (D.14) the integration over the azimuthal momentum can be carried carried analytically

$$\int\frac{\mathrm{d}^3k'}{(2\pi)^3}U(\boldsymbol{k}-\boldsymbol{k}')\delta\sigma(k'_\perp,k'_z)e^{\mathrm{i}K(\chi-\chi')}=\int\mathrm{d}^2k\;U_{-K}(k_\perp,k_z,k'_\perp,k'_z)\delta\sigma(k'_\perp,k'_z) \quad \text{(D.23)}$$

Finally we find

$$(\boldsymbol{k}^2+m_\sigma^2)\delta\sigma(k_\perp,k_z)+\int\mathrm{d}^2kU_{-K}(k_\perp,k_z,k'_\perp,k'_z)\delta\sigma(k'_\perp,k'_z)=-g_\sigma\delta\rho_s(k_\perp,k_z) \quad \text{(D.24)}$$

We now define the Integral kernel

$$H_K(k_\perp,k_z,k'_\perp,k'_z)=(k_\perp^2+k_z^2+m^2)\frac{\delta(k_\perp-k'_\perp)}{k_\perp}\delta(k_z-k'_z)+U_{-K}(k_\perp,k_z,k'_\perp,k'_z) \quad \text{(D.25)}$$

so our equation can be written as

$$\int\mathrm{d}^2k'H_K(k_\perp,k_z,k'_\perp,k'_z)\,\delta\sigma(k'_\perp,k'_z)=-g_\sigma\delta\rho_s(k_\perp,k_z) \quad \text{(D.26)}$$

The Propagator is defined by

$$\int\mathrm{d}^2k''H_K(k_\perp,k_z,k''_\perp,k''_z)\Delta(k''_\perp,k''_z,k'_\perp,k'_z)=\frac{\delta(k_\perp-k'_\perp)}{k_\perp}\delta(k_z-k'_z) \quad \text{(D.27)}$$

and we can solve this integral equation by

$$\delta\sigma(k_\perp,k_z)=-g_\sigma\int\mathrm{d}^2k'\Delta_K(k_\perp,k_z,k'_\perp,k'_z)\delta\rho_s(k'_\perp,k'_z) \quad \text{(D.28)}$$

If we discretize the integration

$$\int k_\perp\mathrm{d}k_\perp\mathrm{d}k_zf(k_\perp,k_z)=\sum_i w_if(k_{\perp i},k_{zi}) \quad \text{(D.29)}$$

(w_i contains the factor $k_{\perp i}$), the δ-function has to be replaced by

$$\delta^2(k-k'):=\frac{1}{k_\perp}\delta(k_\perp-k'_\perp)\delta(k_z-k'_z)\rightarrow\frac{1}{w_i}\delta_{ii'} \quad \text{(D.30)}$$

In this case we obtain

$$\begin{aligned} f(k_{\perp_i},k_{z_i}) &= \int \mathrm{d}^2k\delta^2(k-k')f(k_\perp,k_z) \\ &= \sum_i w_j \frac{1}{w_j}\delta_{jj'}f(k_{\perp j},k_{zj}) \end{aligned} \tag{D.31}$$

and we find

$$\begin{aligned} w_i\delta\sigma(i) &= w_i\delta\sigma(k_{\perp i},k_{zi}) \\ &= -g_\sigma w_i \int \mathrm{d}^2k'\Delta_K(k_\perp,k_z,k'_\perp,k'_z)\delta\rho_s(k'_\perp,k'_z) \\ &= -g_\sigma \sum_j w_i\Delta_K(i,j)w_j\delta\rho_s(j) \end{aligned} \tag{D.32}$$

We therefore need the matrix

$$\Delta_{ij} = w_i\Delta_K(i,j)w_j \tag{D.33}$$

It is obtained from the definition

$$\sum_i H_K(i,j)w_j\Delta_K(j,i') = \frac{1}{w_{i'}}\delta_{ii'} \tag{D.34}$$

or

$$\sum_j H_K(i,j)w_j\Delta_K(j,i')w_{i'} = \delta_{ii'} \tag{D.35}$$

or

$$\Delta_{ij} = w_i\Delta_K(i,j)w_j = H_K^{-1}(i,j) \tag{D.36}$$

Therefore we have to invert the matrix

$$H_K^{-1}(i,j) = (k^2_{\perp_i} + k^2_{z_i} + m^2)\frac{1}{w_i}\delta_{ij} + U_{-K}(i,j) \tag{D.37}$$

Bibliography

[1] Dieperink A.E.L. *Prog. Part. Nucl. Phys.*, 9:121, 1983.

[2] A.V. Afanasjev, T.L. Khoo, S. Frauendorf, G.A. Lalazissis, and I. Ahmad. *Phys. Rev. C*, 67:024309, 2003.

[3] A.V. Afanasjev, J. Knig, and P. Ring. *Nucl. Phys. A*, 608:107, 1996.

[4] A.V. Afanasjev, G.A. Lalazissis, and P. Ring. *Acta Phys. Hung. New Ser. Heavy Ion Phys.*, 6:299, 1997.

[5] A.V. Afanasjev, G.A. Lalazissis, and P. Ring. *Nucl. Phys. A*, 634:395, 1998.

[6] A.V. Afanasjev, I. Ragnarsson, and P. Ring. *Phys. Rev. C*, 59:3166, 1999.

[7] A.V. Afanasjev and P. Ring. *Nucl. Phys. A*, 654:647c, 1999.

[8] A.V. Afanasjev and P. Ring. *Phys. Rev. C*, 62:031302, 2000.

[9] C. O. Almbladh and U. v. Barth. *Phys. Rev. B*, 31:3231, 1985.

[10] G. Audi and A.H. Wapstra. *Nucl. Phys. A*, 595:409, 1995.

[11] T. Aumann et al. *Nucl. Phys. A*, 649:297c, 1999.

[12] Nikolaus B. A., Hoch T., and Madland D. G. *Phys. Rev.*, C46:1757, 1992.

[13] A. D. Becke. *J. Chem. Phys*, 104:1040, 1996.

[14] H. Beil, R. Bergere, P. Carlos, A. Lepretre, A. de Miniac, and A. Veyssiere. *Nucl. Phys. A*, 227:427–449, 1974.

[15] M. Bender, T. Cornelius, G.A. Lalazissis, J.A. Maruhn, W. Nazarewicz, and P.-G. Reinhard. *Eur. Phys. J. A*, 14:23, 2002.

[16] M. Bender, K. Rutz, P.-G. Reinhard, and J. A. Maruhn. *Eur. Phys. J.*, A8:59, 2000.

[17] U.E.P. Berg, C. Blsing, J. Drexler, and et al. *Phys. Lett. B*, 149:59, 1984.

[18] C. Bloch and A. Messiah. *Nucl. Phys.*, 39:95, 1962.

[19] S.K. Bogner, T.T.S. Kuo, and A. Schwenk. *Phys. Rep.*, 386:1, 2003.

[20] N. N. Bogoliubov. *Sov. Phys. Usp.*, 2:236, 1959.

[21] N. N. Bogoliubov. *Usp. Fiz. Nauk.*, 67:549, 1959.

[22] J. Boguta and A.R. Bodmer. *Nuclear Physics A*, 292:43, 1977.

[23] D. Bohle, G. Kilgus, A. Richter, et al. *Phys. Lett. B*, 195:326, 1987.

[24] D. Bohle, A. Richter, U.E.P. Berg, and et al. *Nucl. Phys A*, 458:205, 1986.

[25] D. Bohle, A. Richter, W. Steffen, et al. *Phys. Lett.*, B137:27, 1984.

[26] A. Bohr. *Phys. Rev.*, 81:134, 1951.

[27] A. Bohr. *Mat. Fys. Medd. Dan. Vid. Selsk.*, 26:No. 14, 1952.

[28] N. Bohr. *Nature*, 137:344, 1936.

[29] M. Born and R.J. Oppenheimer. *Ann. Physik*, 87:457, 1927.

[30] G.E. Brown. *Unified Theory of Nuclear Models.* North Holland, Amsterdam, 1964.

[31] G.E. Brown, J.A. Evans, and D.J. Thouless. *Nucl. Phys. A*, (24):1483, 1961.

[32] Kieron Burke, Jan Werschnik, and E. K. U. Gross. *The Journal of Chemical Physics*, 123(6):062206, 2005.

[33] T. Bürvenich, D.G Madland, J.A. Maruhn, and Reinhard P.-G. *Phys. Rev. C*, 65:044308, 2002.

[34] K. Capelle and G. Vignale. *Phys. Rev B*, 65:113106, 2002.

[35] P. Carlos, H. Beil, R. Bergere, A. Lepretre, and A. Veyssiere. *Nucl. Phys. A*, 172:437–448, 1971.

[36] L. Chaves and A. Poves. *Phys. Rev. C*, 34(3):1137–1139, Sep 1986.

[37] J. T. Chayes, L. Chayes, and M. B. Ruskai. *J. Stat. Phys*, 38:497, 1985.

[38] S. A. Chin and J. D. Walecka. *Phys. Lett.*, B52:24, 1974.

[39] Varshalovich D. A., Moskalev A. N., and Khersonskii V. K. *Quantum Theory of Angular Momentum.* World Scientific, Singapore, 1988.

[40] N.D. Dang, A.S Au, T. Suzuki, and A. Arima. *Phys. Rev. C*, 63:044302, 2001.

[41] C. de Coster and K. Heyde. *Phys. Rev. Lett.*, 66:2456, 1991.

[42] C. de Coster, K. Heyde, and A. Richter. *Nucl. Phys. A*, 542:375, 1992.

[43] F. de Jong and H. Lenske. *Phys. Rev.*, C57:3099, 1998.

[44] J. Dobaczewski and J. Dudek. *Phys. Rev. C*, 52:1827, 1995.

[45] R. M. Dreizler and E. K. U. Gross. *Density functional theory.* Springer, Berlin, 1990.

[46] H. P. Dürr and E. Teller. *Phys. Rev.*, 101:494, 1956.

[47] A. R. Edmonds. *Angular Momentum in Quantum Mechanics.* University Press, Princeton, 1957.

[48] R. Englman. *The Jahn-Teller effect in molecules and crystals.* Wiley, London, 1972.

[49] A. Faessler, D.T. Khoa, M. Grigorescu, and R. Nojarov. *Phys. Rev. Lett.*, 65:2978, 1990.

[50] D. Frekers, H.J. Wortche, A. Richter, et al. *Phys. Lett.*, B244:178, 1990.

[51] D. Frekers, H.J. Wrtche, A. Richter, and et al. *Phys. Lett. B*, 244:178, 1990.

[52] B. Friedman and V. R. Pandharipande. *Nucl. Phys.*, A361:502, 1981.

[53] S. Fritsch, N. Kaiser, and W. Weise. *Nucl. Phys. A*, 750:259, 2005.

[54] C. Fuchs, H. Lenske, and H. H. Wolter. *Phys. Rev.*, C52:3043, 1995.

[55] J. Gibelin. *Search for the low lying dipole strength in the neutron rich nucleus* ^{26}Ne. PhD thesis, Institut de physique nucléaire, Orsay, 2006.

[56] T. L. Gilbert. *Phys. Rev. B*, 12:2111, 1975.

[57] M Glodhaber and E. Teller. *Phys. Rev.*, 73:1156, 1948.

[58] D. Gogny. *Phys. Rev. Lett.*, 35:565, 1975.

[59] I. Hamamoto and C. Magnusson. *Phys. Lett. B*, 260:6, 1991.

[60] J. E. Harriman. *Phys. Rev. A*, 24:680, 1981.

[61] T. Hartmann, J. Enders, P. Mohr, K. Vogt, S. Volz, and A. Zilges. *Phys. Rev. Lett.*, 85:274, 2000.

[62] K. Heyde and C. de Coster. *Phys. Rev. C*, 44:R2262, 1991.

[63] R.R. Hilton. *Z. Phys.*, A316:121, 1984.

[64] R.R. Hilton. *Ann. Phys.*, 214:258, 1992.

[65] R.R Hilton, W. Höhenberger, and P. Ring. *Eur. Phys. J. A*, 1:257, 1998.

[66] F. Hofmann, C. M. Keil, and H. Lenske. *Phys. Rev.*, C64:025804, 2001.

[67] P. Hohenberg and W. Kohn. *Phys. Rev.*, 136(B864), 1964.

[68] C. J. Horowitz and B. D. Serot. *Phys. Lett.*, B140:181, 1984.

[69] F. Iachello. *Nucl. Phys.*, A358:89, 1981.

[70] Dobaczewski J., Nazarewicz W., Werner T. R., Berger J. F., Chinn C. R., and Dechargé J. *Phys. Rev*, C53:2809, 1996.

[71] Rusnak J. J. and R. J. Furnstahl. *Nucl. Phys*, A627:495, 1997.

[72] H.A. Jahn and E. Teller. *Proc. Roy. Soc.*, A161:220, 1937.

[73] M. H. Johnson and E. Teller. *Phys. Rev.*, 93:93, 1954.

[74] M. H. Johnson and E. Teller. *Phys. Rev.*, 98:783, 1955.

[75] S. Kamerdzhiev, J Speth, and Tertychny G. *Phys. Rept.*, 393:1–86, 2004.

[76] E. Khan and N. Van Giai. *Phys. Lett. B*, 472:253–257, 2000.

[77] W. Kohn and L. J. Sham. *Phys. Rev.*, 140(4A):A1133–A1138, Nov 1965.

[78] S.J. Krieger, P. Bonche, H. Flocard, P. Quentin, and M.S. Weiss. *Nuc. Phys. A*, 517:275–284, 1990.

[79] H. Kucharek and P. Ring. *Z. Phys.*, A339:23, 1991.

[80] G. Lalazissis, D. Vretenar, and P. Ring. *Phys. Rev. C*, 69:017301, 2004.

[81] G. A. Lalazissis, T. Nikšić, D. Vretenar, and P. Ring. *Phys. Rev.*, C71:024312, 2005.

[82] G.A. Lalazissis, A.R. Farhan, and M.M. Sharma. *Nucl. Phys. A*, 628:221, 1998.

[83] G.A. Lalazissis, J. König, and P. Ring. *Phys. Rev. C*, 55:540, 1997.

[84] G.A. Lalazissis, D. Vretenar, W. Pschl, and P. Ring. *Nucl. Phys. A*, 632:363, 1998.

[85] G.A. Lalazissis, D. Vretenar, W. Pschl, and P. Ring. *Phys. Lett. B*, 418:7, 1998.

[86] G.A. Lalazissis, D. Vretenar, and P. Ring. *Phys. Rev. C*, 57:2294, 1998.

[87] G.A. Lalazissis, D. Vretenar, and P. Ring. *Nucl. Phys. A*, 650:133, 1999.

[88] G.A. Lalazissis, D. Vretenar, and P. Ring. *Phys. Rev. C*, 63:034305, 2001.

[89] G.A. Lalazissis, D. Vretenar, and P. Ring. *Nucl. Phys. A*, 679:481, 2001.

[90] G.A. Lalazissis, D. Vretenar, P. Ring, Stoitsov M., and L. Robledo. *Phys. Rev. C*, 60:014310, 1999.

[91] G.A. Lalazissis, D. Vretenar, P. Ring, M. Stoitsov, and L. Robledo. *Phys. Rev. C*, 60:014310, 1999.

[92] P. E. Lammert. *J. Chem. Phys.*, 125:074114, 2006.

[93] M. Levy. *Phys. Rev. A*, 26:1200, 1986.

[94] M. Levy, J. P. Perdew, and V. Sahni. *Phys. Rev. A*, 30:2745, 1984.

[95] E. H. Lieb. *Density functional methods in physics.* Plenum, New York, 1985.

[96] E. Litvinova and P. Ring. *Phys. Rev. C*, 73:044328, 2006.

[97] Huan Liu and Larry Zamick. *Phys. Rev. C*, 36(5):2057–2063, Nov 1987.

[98] N. Lo Iudice and F. Palumbo. *Phys. Rev. Lett.*, 41:1532, 1978.

[99] Z. Ma et al. *Nucl. Phys. A*, 703:222, 2002.

[100] H. Madokoro and M. Matsuzaki. *Prog. Theor. Phys.*, 101:1027, 1999.

[101] C. Magnusson. *Physica Scripta*, 43:460, 1991.

[102] J.A. McNeil, R.J. Furnstahl, E. Rost, and J.R. Shepard. *Phys. Rev. C*, 40:399, 1989.

[103] T. Nikšić, D. Vretenar, P. Finelli, and P. Ring. *Phys. Rev.*, C66:024306, 2002.

[104] T. Niksic, D. Vretenar, P. Ring, and G.A. Lalazissis. *Phys. Rev. C*, 65:054320, 2002.

[105] R. Nojarov and A. Faessler. *Nucl. Phys. C*, 41:1243, 1990.

[106] R. Nojarov, A. Faessler, and P.O. Lipas. *Nucl. Phys. A*, 553:381, 1991.

[107] R. Nojarov, A. Faessler, and P. Sarriguren. *Nucl. Phys. A*, 563:349, 1993.

[108] N. Paar, T. Nikšić, D. Vretenar, and P. Ring. *Phys. Lett. B*, 606:288, 2005.

[109] N. Paar, P. Ring, T. Nikšić, and D. Vretenar. *Phys. Rev. C*, 67:034312, 2003.

[110] N. Paar, D. Vretenar, and P. Ring. *Phys. Rev. Lett.*, 94:182501, 2005.

[111] S. Patra, S. Yoshida, N. Takigawa, and C.R. Praharaj. *Phys. Rev. C*, 50:1924, 1994.

[112] W. Pauli. *Naturwiss.*, 12:741, 1924.

[113] J. P. Perdew, S. Kurth, A. Zupan, and P. Blaha. *Phys. Rev. Lett*, 82:2544, 1999.

[114] J. P. Perdew, R. G. Parr, M. Levy, and J. L. Balduz. *Phys. Rev. Lett.*, 49:1691, 1982.

[115] J. P. Perdew and Y. Wang. *Phys. Rev. B*, 33:8800, 1986.

[116] C.E. Price and G.E. Walker. *Phys. Lett. B*, 155:17, 1985.

[117] W. Pschl, D. Vretenar, G.A. Lalazissis, and P. Ring. *Phys. Rev. Lett.*, 79:3841, 1997.

[118] A.A. Raduta, N. Lo Ioudice, and I.I. Ursu. *Nucl. Phys. A*, 584:84, 1995.

[119] J. Rainwater. *Phys. Rev.*, 79:432, 1950.

[120] C. Rangacharyulu, A. Richter, H.J. Wrtche, and et al. *Phys. Rev. C*, 43:R949, 1991.

[121] P.-G. Reinhard. *Rep. Prog. Phys.*, 52:439, 1989.

[122] P.-G. Reinhard, M. Rufa, J. Maruhn, W. Greiner, and J. Friedrich. *Z. Phys. A*, 323:13, 1986.

[123] P.G. Reinhard. *Nucl. Phys. A*, 649:105c, 1999.

[124] A. Richter. *Contemporary Topics in Nuclear Structure Physics*, page 127. World Scientific, Singapore, 1988.

[125] A. Richter. *Nucl. Phys. A*, 507(99), 1990.

[126] A. Richter. *Nucl. Phys. A*, 522:139, 1991.

[127] A. Richter. *Nucl. Phys. A*, 553:417, 1992.

[128] A. Richter. *Nucl. Phys. A*, 553:417c, 1993.

[129] A. Richter. *Prog. Part. Nucl. Phys.*, 34:261, 1995.

[130] P. Ring. *Prog. Part. Nucl. Phys.*, 37:193, 1996.

[131] P. Ring and A.V. Afanasjev. *Prog. Part. Nucl. Phys.*, 38:137, 1997.

[132] P. Ring, Zhong-Yu Ma, Nguyen Van Giai, D. Vretenar, A. Wandelt, and Li-Gang Cao. *Nucl. Phys.*, A694:249, 2001.

[133] P. Ring and P. Schuck. *The nuclear many-body problem.* Springer, Heidelberg, 1980.

[134] G. Rusev, E. Grosse, M. Erhard, K. Junghans, K. Kosev, et al. *Eur. Phys. J. A*, 27:171–176, 2006.

[135] K. Rutz, M. Bender, P. Reinhard, and J.A. Maruhn. *Phys. Lett. B*, 468:1, 1999.

[136] K. Rutz, M. Bender, P.-G. Reinhard, J.A. Maruhn, and W. Greiner. *Nucl. Phys. A*, 634:67, 1998.

[137] H. Sagawa, N. Van Giai, N. Takigawa, M. Ishihara, and K. Yazaki. *Z. Phys. A*, 351:385, 1995.

[138] H. Schüler and Th. Schmidt. *Z. Phys.*, 94:457, 1935.

[139] B. D. Serot. *Rep. Prog. Phys.*, 55:1855, 1992.

[140] B. D. Serot and J. D. Walecka. *Adv. Nucl. Phys.*, 16:1, 1986.

[141] M. Serra. *Field theoretical description of exchange terms and pairing correlation in nuclear systems.* Phd thesis, Technical University of Munich (unpublished), 2001.

[142] M. Serra and P. Ring. *Phys. Rev.*, C65:064324, 2002.

[143] M.M. Sharma, M.A. Nagarajan, and P. Ring. *Phys. Lett. B*, 312:377, 1993.

[144] J.R. Shepard, E. Rost, and J.A. McNeil. *Phys. Rev C*, 40:2320, 1989.

[145] H. Steinwedel and J.H.D Jensen. *Z. Naturforschung*, 5a:413, 1950.

[146] Y. Sugahara and H. Toki. *Nuclear Physics A*, 579:557, 1994.

[147] T. Suzuki and D.J. Rowe. *Nucl. Phys. A*, 289:461, 1977.

[148] C.E. Svensson and et al. *Phys. Rev. Lett.*, 82:3400, 1999.

[149] N. Takigawa, S. Yoshida, K. Hagino, S.K. Patra, and C. Praharaj. *Phys. Rev. C*, 53:1038, 1996.

[150] J. Tao, J. P. Perdew, V. N. Staroverov, and G. E. Scuseria. *Phys. Rev. B*, 69:075102, 2004.

[151] M. Tohyama and A.S Umar. *Phys. Lett. B*, 516:415, 2001.

[152] E. Tryggestad et al. *Nucl. Phys. A*, 687:231c, 2001.

[153] V. Tselyaev et al. *Phys. Rev.*, C75:014315, 2007.

[154] S. Typel and H. H. Wolter. *Nucl. Phys.*, A656:331, 1999.

[155] C. A. Ullrich and W. Kohn. *Phys. Rev. Lett.*, 89:156401, 2002.

[156] J. Uusitalo and et al. *Phys. Rev. C*, 59:R2975, 1999.

[157] J. G. Valatin. *Phys. Rev.*, 122:1012, 1961.

[158] D. Vautherin and D. M. Brink. *Phys. Rev.*, C5:626, 1972.

[159] F. Villars. *Varenna Lectures*, 36:1; 14, 1966.

[160] P. von Brentano, A. Zilges, R. D. Heil, et al. *Nucl. Phys. A*, 557:593, 1993.

[161] D. Vretenar, A. V. Afanasjev, G. A. Lalazissis, and P. Ring. *Physics Reports*, 409:101, 2005.

[162] D. Vretenar, G.A. Lalazissis, and P. Ring. *Phys. Rev. C*, 57:3071, 1998.

[163] D. Vretenar, T. Nikšić, N. Paar, and P. Ring. *Nucl. Phys. A*, 731:281, 2004.

[164] D. Vretenar, W. Pschl, G.A. Lalazissis, and P. Ring. *Phys. Rev. C*, 57:R1060, 1998.

[165] J. D. Walecka. *Annals Phys.*, 83:491–529, 1974.

[166] D. A. Wasson. *Phys. Lett. B*, 210:41, 1988.

[167] T.R. Werner, J.A. Sheikh, M. Misu, W. Nazarewicz, J. Rikovska, K. Heeger, A.S. Umar, and M.R. Strayer. *Nucl. Phys. A*, 597:327, 1996.

[168] S. Yoshida, S. Patra, N. Takigawa, and C.R. Praharaj. *Phys. Rev. C*, 50:1398, 1994.

[169] D. Zawischa, M. Macfarlane, and J. Speth. *Phys. Rev. C*, 42:1461, 1990.

[170] D. Zawischa and J. Speth. *Phys. Rev. Lett. B*, 252:4, 1990.

[171] H. D. Zeh. *Z. Phys.*, 202:28, 1967.

[172] Z. Y. Zhu, H. J. Mang, and P. Ring. *Phys. Lett*, B254:325, 1991.

[173] W. Ziegler, C. Rangacharyulu, A. Richter, and C. Spieler. *Phys. Rev. Lett.*, 65:2515, 1990.